

# Improved analysis of air shower radio emission with the LOPES experiment

Zur Erlangung des akademischen Grades eines  
DOKTORS DER NATURWISSENSCHAFTEN  
von der Fakultät für Physik  
des Karlsruher Instituts für Technologie (KIT)

genehmigte  
DISSERTATION

von Diplom-Physikerin Katrin Link  
aus Tübingen

Tag der mündlichen Prüfung: 18.11.2016  
Referent: Prof. Dr. Dr. h.c. Blümer  
Korreferent: Prof. Dr. Quast  
Betreuer: Dr. Huege



# Abstract

Galactic and Extragalactic objects produce highly energetic particles. Entering the Earth's atmosphere, these cosmic ray particles generate extensive air showers. During the evolution of the shower high numbers of electrons and positrons are created which emit radio signals. The LOPES experiment was measuring this radio emission for around ten years. Already during that time our knowledge of the emission properties and our understanding of the physics behind the emission processes increased tremendously.

The LOPES experiment played a pioneering role in bringing forward the radio measurement technique, also profiting from its host experiment KASCADE-Grande.

The proof-of-principle for air shower measurements using interferometric beamforming was provided by LOPES. Many publications followed and finally it was shown that the important air shower characteristics can be reconstructed using LOPES measurements. At the same time the Monte Carlo Codes which were used for simulating the expected radio signals evolved.

But one of the still open questions was why the amplitude measured by LOPES was lower than predicted by the current state-of-the-art simulation code CoREAS.

This was closely connected with the question how precise the electric field component can be reconstructed from LOPES measurements. Particularly, since a simplified reconstruction needs to be applied, whose influence has never been investigated in detail.

Within this work the complete reconstruction pipeline for LOPES data was overhauled and improved.

In particular, the missing detector simulation was developed, which allowed to use the same analysis software for measured and simulated data. This directly provides the application of the interferometric analysis to simulations.

Furthermore, it was now possible to investigate the influence of the simplified reconstruction and the influence of measured noise on the reconstruction parameters.

It could be shown that neither the simplified reconstruction nor other detector effects nor the measured radio noise led to a deformation of the radio signal that could explain the observed difference between LOPES and CoREAS simulations.

It became apparent that the external reference source, used for the amplitude calibration, was calibrated in a way that did not fit the needs for air shower measurements. Using updated reference values, a recalibration of the LOPES amplitude was performed. This resulted in a lower measured amplitude which now matches the expectations from CoREAS simulations. A detailed comparison between data and simulations based not only on the lateral distribution but also on the interferometric quantities was performed.

With the improved analysis former results, reconstructed from amplitude parameters, were corrected and other published results were confirmed. Arrival direction and energy of the primary particle as well as the depth of the shower maximum were reconstructed using both, data and simulations and for the first time LOPES-only accuracies were provided.



# Verbesserte Analyse der Radioemission von Luftschauern mit dem LOPES Experiment

Galaktische sowie extragalaktische Objekte produzieren sehr hochenergetische Teilchen. Dringen diese in die Erdatmosphäre ein induzieren sie Schauer aus Sekundärteilchen, größtenteils Elektronen und Positronen, welche Radiostrahlung emittieren. Etwa zehn Jahre lang wurde diese Radiostrahlung durch das LOPES Experiment vermessen. Insbesondere durch die Zusammenarbeit mit dem Experiment KASCADE-Grande kam LOPES damit eine Schlüsselrolle bei der Verbesserung des Verständnisses der Radioemissionsmechanismen und der ihnen zugrunde liegenden physikalischen Prozesse zu.

Nach dem ersten Beweis der Messbarkeit kosmischer Strahlung mittels interferometrischer Verfahren gab es eine ganze Reihe weiterer Veröffentlichungen der LOPES-Kollaboration und es konnte schließlich gezeigt werden, dass alle wichtigen Luftschauparameter aus den Messungen rekonstruiert werden können. Gleichzeitig wurden auch die Monte-Carlo-Verfahren zur Simulation der Radiostrahlung weiterentwickelt, hin zum auch in dieser Arbeit verwendeten Programm CoREAS.

Die von CoREAS vorhergesagte Radiostrahlung wies allerdings eine größere Amplitude auf als von LOPES gemessen. Diese Diskrepanz zwischen Daten und Simulationen ist eng verknüpft mit der Frage, wie präzise das elektrische Feld aus den LOPES-Daten rekonstruiert werden kann, vor allem, da die Rekonstruktion zwingend auf einer vereinfachenden Annahme basiert, deren Einfluss bisher nicht geklärt worden war.

Im Rahmen dieser Arbeit wurde die gesamte Rekonstruktionskette grundlegend überprüft und verbessert. Insbesondere wurde eine bisher fehlende Detektorsimulation zur Anwendung auf CoREAS-Simulationen entwickelt. Mit deren Hilfe war es nun möglich sowohl gemessene, als auch simulierte Daten mit derselben Software zu analysieren. So konnten erstmalig interferometrische Verfahren auch auf simulierte Daten angewendet werden.

Darüber hinaus ließen sich so die Einflüsse der vereinfachten Rekonstruktion und des gemessenen Rauschens auf die rekonstruierten Messgrößen untersuchen.

Es konnte gezeigt werden, dass weder die vereinfachte Rekonstruktion noch der Detektor selbst das Signal in der Form verändern, dass damit der beobachtete Unterschied zwischen LOPES-Daten und CoREAS-Simulationen erklärt werden könnte.

Es stellte sich heraus, dass diese Diskrepanz durch eine für die Bedürfnisse von Luftschauparameter-Messungen ungeeignete Kalibration der Referenzquelle, welche für die Amplitudenkalibration verwendet wird, hervorgerufen wurde. Nach einer neuen Kalibration zeigen die LOPES-Daten und CoREAS-Simulationen eine gute Übereinstimmung. Sowohl auf der gemessenen Lateralverteilung als auch auf interferometrischen Größen beruhend wurde ein detaillierter Vergleich zwischen Daten und Simulationen durchgeführt.

Mittels der verbesserten Analyse konnten Resultate, welche auf der gemessenen Amplitude basieren, korrigiert werden und weitere bisherige Ergebnisse bestätigt werden. Ankunftsrichtung und Energie des Primärteilchens sowie die Tiefe des Schauermaximums wurden dabei sowohl für Daten als auch für Simulationen rekonstruiert und es konnten erstmals auch LOPES-eigene Genauigkeiten bestimmt werden.



# Contents

<b>1</b>	<b>Introduction</b>	<b>1</b>
<b>2</b>	<b>Cosmic Rays</b>	<b>5</b>
2.1	Energy Spectrum of cosmic rays . . . . .	5
2.2	Extensive air showers . . . . .	7
2.3	Detection of high-energy cosmic rays . . . . .	9
2.3.1	Particle detectors . . . . .	9
2.3.2	Fluorescence detectors . . . . .	10
2.3.3	Cherenkov detectors . . . . .	10
2.3.4	Radio detectors . . . . .	10
2.4	Radio emission of cosmic-ray air showers . . . . .	11
2.4.1	Basic properties of radio emission . . . . .	11
2.4.2	Radio emission physics . . . . .	12
2.4.3	Experiments . . . . .	14
<b>3</b>	<b>The LOPES experiment</b>	<b>17</b>
3.1	Setups and previous results . . . . .	18
3.2	Standard analysis pipeline . . . . .	23
3.2.1	Summary of reconstructed radio emission parameters . . . . .	28
3.3	Reconstruction of electric field components . . . . .	29
3.4	Status before improved analysis . . . . .	30
3.5	Event selection . . . . .	33
3.5.1	Simulations of measured events . . . . .	34
<b>4</b>	<b>Detector simulation</b>	<b>37</b>
4.1	Structure of <i>reas2event</i> . . . . .	39
4.1.1	Requirements . . . . .	39
4.1.2	Upsampling of the raw simulations . . . . .	39
4.1.3	Reading simulations . . . . .	40
4.1.4	Calculate signal at antenna footpoint . . . . .	41
4.1.5	Calculate signal at ADC . . . . .	43
4.1.6	Noise treatment . . . . .	43
4.1.7	Write LOPES .event file . . . . .	45
4.2	Influence of noise on reconstruction parameters . . . . .	45
4.3	Influence of the simplified reconstruction on the electric field components	52

4.4	Comparison of pure simulations and simulations including noise . . . . .	58
4.5	Influence of reconstruction method on lateral time distribution . . . . .	59
4.6	Conclusion . . . . .	61
<b>5</b>	<b>Absolute Amplitude Calibration</b>	<b>63</b>
5.1	Revision of the simulated antenna gain pattern . . . . .	64
5.2	Implementation of the absolute amplitude calibration . . . . .	67
5.3	Verification of the original calibration analysis . . . . .	68
5.4	Exchange of the calibration software . . . . .	70
5.5	Revised characterisation of the reference source . . . . .	71
5.6	Impact of revised amplitude calibration on reconstructed quantities . . .	72
5.7	Conclusion . . . . .	75
5.8	Cross-Calibration with LOFAR and Tunka-Rex . . . . .	76
<b>6</b>	<b>Revision of former results using the improved analysis</b>	<b>79</b>
6.1	Discussion of uncertainties . . . . .	80
6.2	Comparison of data and simulations . . . . .	83
6.2.1	Lateral distribution . . . . .	84
6.2.2	CC-beam amplitude and cone angle $\rho_{CC}$ . . . . .	89
6.2.3	Conclusion . . . . .	91
6.3	Reconstruction of arrival direction . . . . .	92
6.4	Reconstruction of the cosmic-ray energy . . . . .	94
6.4.1	Based on CC-beam . . . . .	94
6.4.2	Based on the amplitude at a certain lateral distance . . . . .	100
6.4.3	Comparing energy scales of KASCADE-Grande and Tunka-133 . .	104
6.5	Reconstruction of the shower maximum . . . . .	107
6.6	Conclusion . . . . .	111
<b>7</b>	<b>Conclusion</b>	<b>113</b>
<b>A</b>	<b>Histograms of the radio emission properties</b>	<b>117</b>
A.1	Properties from lateral distribution . . . . .	118
A.2	Properties from beamforming . . . . .	119
A.3	Cone angle from lateral time fit . . . . .	120
<b>B</b>	<b>Calibration certificate of reference source</b>	<b>123</b>
	<b>Bibliography</b>	<b>137</b>

# 1

## Introduction

Measurements of cosmic ray particles have been performed for more than a hundred years, but are still of high interest as the origin of the cosmic particles is not yet fully understood. Since they cover such a wide range of energy, different observation techniques are necessary. For energies below  $10^{14}$  eV the flux of cosmic rays is high enough for a direct measurement of the particles in space or at high altitudes. At these energies the mass composition of the cosmic ray particles is well understood and their acceleration is explained by Galactic sources, mainly supernova remnants.

For higher energies the measurement is more complex since the flux becomes too low for a measurement in space and therefore big detector arrays on ground are necessary. While travelling through the Earth's atmosphere the primary particles interact with nuclei and a cosmic ray air shower evolves. Using various techniques the primary particle's mass, energy and arrival direction need to be reconstructed from the air shower properties. The best-established method for the detection of air showers is the measurement of the secondary particles with arrays of particle detectors. But for a reconstruction of the primary particle properties they have to rely on models describing the hadronic interactions. Fluorescence or Cherenkov telescopes measure the light emitted during the air shower evolution. These techniques are less model-dependent but both suffer from a low duty cycle. In the last years the radio technique caught up with these well-established techniques combining a good duty cycle with minor model dependencies. It turns out that combining different techniques in so-called hybrid measurements are the key for successful air shower measurements that are able to solve the open questions of cosmic ray properties at the highest energies.

The first radio measurements already started in the 1960s still using analogue techniques. Their success was limited and the interest in this field decreased after an initial period of intense research. In the early 2000s a revival of the now digital radio measurements started, accompanied by theoretical investigations. One of the first modern radio experiments was the LOPES array co-located with the KASCADE-Grande particle detector array. KASCADE-Grande not only provided a trigger on high energy air showers but also high level reconstruction parameters such as energy and arrival direction.

Originally built for a proof-of-principle, LOPES was able to show that radio measurements yield information on the primary properties mass, energy and arrival direction. But although remarkable results were achieved with LOPES a number of open questions concerning the standard reconstruction pipeline remained along with the question if and how these affect the results. In the standard analysis pipeline of LOPES a simplified reconstruction is applied and it was never tested whether this simplification is valid and if the reconstructed electric field components are compatible with the true components.

While a comparison of LOPES measurements and REAS 3.11 simulations showed a good agreement, the amplitudes calculated using the superior CoREAS simulations were more than a factor of two too low and even within uncertainties they did not match. It was unclear whether this was due to the simplified reconstruction or any other unknown inconsistency in the standard analysis pipeline of LOPES or whether it was a true divergence between data and simulations. Since LOPES was the only radio experiment with an absolute amplitude calibration at that time, this could not be checked by any other experiment.

A good agreement of data and simulations is of special interest for the reconstruction of the primary particle energy. Radio measurements can provide an independent determination of the energy scale using a parameter-free Monte-Carlo simulation code like CoREAS. To get reliable results the amplitude of the measurement needs to be precisely calibrated and the simulations need to predict these amplitudes accurately.

Another important aspect is that in the standard reconstruction pipeline of LOPES an interferometric beamforming is applied to LOPES data which was never applied to simulations. But LOPES results are partly based on quantities determined by the beamforming method: The depth of shower maximum is correlated with the cone angle and the energy is reconstructed from the amplitude of the cross-correlation beam. These analyses were either not done with simulations, or for the depth of shower maximum, are based on a different determination of the cone angle. This raises the question how to apply the beamforming method on simulations and whether the different treatment of data and simulations influences the obtained results.

Furthermore the influence of noise on the reconstructed radio signal properties was formerly investigated using test pulses. Based on these investigations a noise correction is applied within the standard reconstruction. But so far it was never tested if this noise correction is also valid for true pulses, with a pulse shape as expected from air showers. To address these questions the complete standard analysis pipeline of LOPES was scrutinized in this work to eliminate potential problems and check the validity of the simplified reconstruction. Especially, a full detector simulation was developed to investigate the various open points.

The detector simulation is used to fold in the detector effects on simulated events. These events can then be reconstructed with the standard analysis pipeline, including the interferometric beamforming, and the reconstructed properties can be compared with the true ones. Three aspects were investigated using this detector simulation. First, it directly provides an interferometric beamforming applied to simulations. This allowed for the first time the evaluation of the beamforming parameters reconstructed from simulations. Second, it was investigated how noise influences the reconstructed parameters. The measured noise can be added optionally to the simulated signal within the

detector simulation. Since LOPES is located in a radio-noisy environment the optional inclusion of noise allows to study also the principle potential of the used techniques which is of special interest for other experiments in radio quiet areas. And third, the influence of the simplified reconstruction was tested by comparing the true and reconstructed electric field components.

A description of the detector simulation and how the simplified reconstruction and noise influences the radio properties is presented in chapter 4. Although the measured quantities are partly influenced by both, noise and the simplified reconstruction, no significant problem was found. Therefore it could be ruled out that these effects lead to the disagreement of LOPES-measured amplitudes and those simulated by CoREAS.

The influence of the absolute amplitude calibration, applied in the standard pipeline, cannot be studied with the developed detector simulation, and was therefore separately analysed. This included a revision of the simulated gain pattern of the LOPES antennas, a new and independent implementation of the analysis software used to interpret LOPES calibration measurements and an update of the calibration values of the reference antenna, see chapter 5. It turned out that the calibration values of the reference source did not fit our actual needs and a recalibration was requested from the manufacturer. Using these new reference values updated calibration values were calculated, resulting in lower measured amplitudes.

Based on the findings of this thesis a final analysis was done. This includes detailed comparison between LOPES data and CoREAS simulations, based on several radio emission quantities. Using the detector simulation and the updated amplitude calibration a conclusive result was obtained. Furthermore, the reconstruction of the air shower parameters – arrival direction, energy of the primary particle and depth of shower maximum – was performed, now in the same way for data and simulations with and without noise. This allows to also quantify the LOPES-only resolution and gives the intrinsic accuracy. The achieved results are presented in chapter 6.



# 2

## Cosmic Rays

More than 100 years ago Victor Hess measured the ionization in the air and discovered that at higher altitude this ionization increases (Hess, 1912). This was the first evidence for the so-called cosmic rays. The next years several further balloon flights and more detailed measurements followed (for a review see Fick and Hoffmann (2014)), showing that the cosmic rays are charged particles coming from space with a wide range of energies. Cosmic rays mainly exist of atomic nuclei and only around 2% are electrons or gamma rays. Today the energy spectrum of cosmic rays is measured by several experiments using different techniques for the different energy ranges. But up to now there are still many open questions to be clarified.

### 2.1 Energy Spectrum of cosmic rays

Cosmic rays cover a wide energy range beginning at around  $10^{10}$  eV up to more than  $10^{20}$  eV, see figure 2.1. Below  $10^{10}$  eV the energy spectrum is dominated by the geomagnetic cut-off and solar modulation. These effects shield cosmic rays with lower energies from reaching the Earth. Above  $10^{10}$  eV the flux follows a power law with different spectral indices. Up to the so-called *knee* at around  $4 \times 10^{15}$  eV the spectral index is  $\gamma \approx 2.7$ . Below  $10^{14}$  eV the flux is high enough to be measured with small detector systems at high altitude or in space. These detector systems allow a detailed measurement of energy, mass and arrival direction. Therefore the mass spectrum in this energy range is known, see figure 2.2. The nuclear abundance in cosmic rays follows mainly the one of our solar system indicating a stellar origin of cosmic rays. The difference in both spectra can be explained by spallation and fragmentation of cosmic-ray nuclei while travelling through the interstellar medium.

For higher energies the flux drops and therefore larger detector areas and longer measurements are necessary. This is only possible on Earth and not in space. But while travelling through the atmosphere the primary particle interacts with particles in the air and an extensive air shower evolves, see section 2.2. Therefore mass and energy of

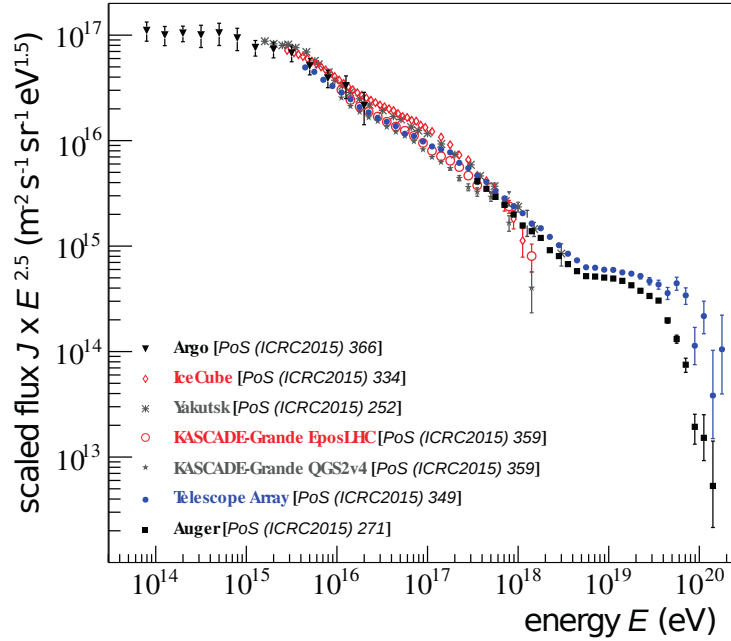


Figure 2.1: Scaled flux of cosmic rays as a function of energy for several experiments. The flux is scaled with  $E^{2.5}$  to visualize the different features. From Verzi (2016).

the primary particle in this energy range cannot be directly measured but have to be reconstructed from air shower parameters.

The change in the spectral slope around the *knee* to  $\gamma \approx 3$  is caused by a decreasing flux of light nuclei (Antoni et al., 2003; Aglietta et al., 2004). The favoured explanation is that these light nuclei cannot be accelerated to higher energies by Galactic objects. An alternative explanation is a reduced flux due to a charge-dependant leakage from the galaxy. Since both processes are charge-dependant they predict a second *knee* for heavy particles which was observed by KASCADE-Grande at an energy of  $10^{16.9}$  eV (Apel et al., 2011b).

At energies around  $4 \times 10^{18}$  eV the spectral index of the power law drops again to  $\gamma \approx 2.7$  forming the so-called *ankle*. This might be connected to a transition from Galactic to Extragalactic origin which is supported by the ankle-like feature in the light component of the cosmic rays at  $\sim 10^{17.08}$  eV discovered by KASCADE-Grande (Apel et al., 2013b). But still different models, as discussed in Unger (2008) can predict the observed all-particle spectrum and only a precise measurement of the composition at the very high energies allow a discrimination of the different models.

At energies above  $5 \times 10^{19}$  eV the spectrum cuts-off. Statistics in this energy range are low and a mass discrimination quite complex. Therefore it is not clear where this cut-off comes from. One possible explanation is that the accelerators cannot speed up the particles to higher energies. Alternatively the cut-off can be explained by the GZK effect (Zatsepin and Kuzmin, 1966; Greisen, 1966). The latter is only compatible with a pure proton composition since it is caused by the interaction of protons with photons from the cosmic microwave background. The leading experiments measuring composition at the highest energies are the Pierre Auger Observatory (Abraham J. et al., 2004; Aab et al., 2015) and the Telescope Array (Kawai et al., 2008). Currently a joint analysis of

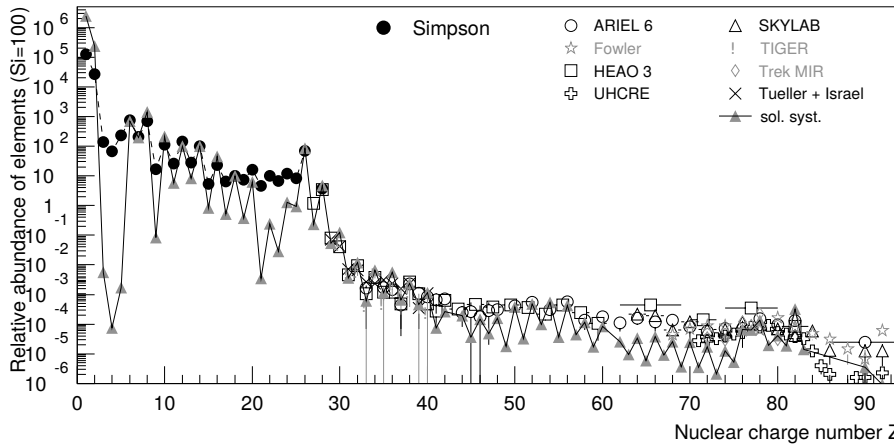


Figure 2.2: Relative nuclear abundance in cosmic rays, normalized to Si=100, at energies around 1 GeV/n and the relative abundance of nuclei in the solar system (Hörandel, 2008).

both experiments is going on providing the most promising approach for solving this question (Abbasi et al., 2016). But still the composition resolution at the highest energies is insufficient. The upgrade of the Pierre Auger Observatory, AugerPrime, will be able to provide high precision composition data at these highest energies (Aab et al., 2016b).

## 2.2 Extensive air showers

Extensive air showers occur once the primary particle of the cosmic ray interacts with a particle of the atmosphere (Auger et al., 1939). After this first hadronic interaction the secondary particles interact further and a cascade of particles evolves penetrating the whole atmosphere. The secondary particles can be split in three groups as shown in figure 2.3.

The hadronic component consists mainly of protons, neutrons, pions and kaons. Since these particles decay or interact further with air molecules this component has a short range and only few hadrons reach the ground. Charged pions and kaons decay into muons and muonic neutrinos and thus feed the muonic component. Neutral pions decay into gammas and feed the electromagnetic component. Protons and neutrons interact further with air molecules and hadrons with lower energy are produced.

Muons and muonic neutrinos build the muonic component. This component has the longest range. Since muons have a long lifetime most of them reach the ground before they decay and due to their small cross section the neutrinos can even penetrate through the Earth.

The electromagnetic component makes up around 90% of the particles and is formed by electrons, positrons and photons. The number of particles increases by pair production and bremsstrahlung until the critical energy is reached. This is called the shower maximum and its depth can be used as an indication for the primary mass. After the maximum low-energetic electromagnetic particles lose their energy via ionisation or Compton scattering and the number of particles decreases again. The electromagnetic component can reach a lateral distribution of several hundred metres at sea level and is

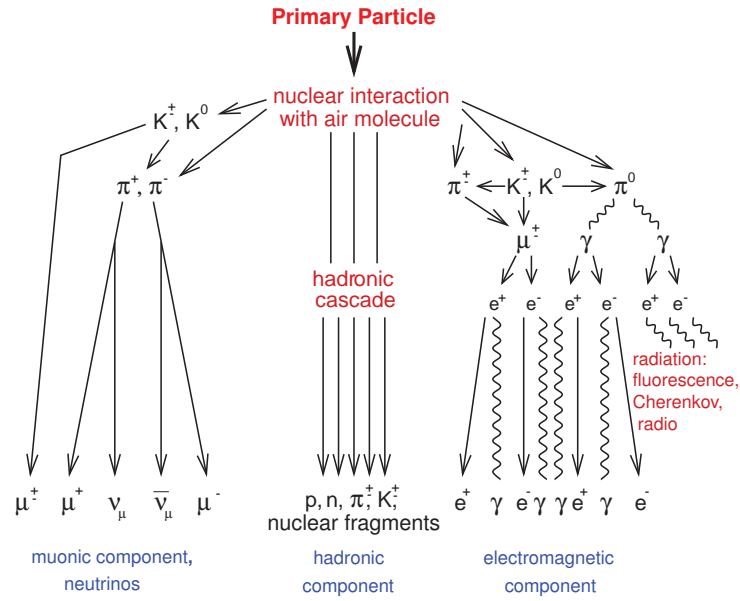


Figure 2.3: Scheme of an extensive air shower showing the three different components (Haungs et al., 2003).

responsible for the radio emission.

A simple model for the qualitative development of the electromagnetic cascade is the Heitler model (Heitler, 1954) which takes only into account pair-production and bremsstrahlung which leads to a doubling of the number of particles after each interaction length. The hadronic component can be described by the extended Heitler model, see Matthews (2005) where only pions are considered.

A comparison of the different components and its size allows to reconstruct the properties of the primary particle. E.g. the ratio of the muons to electrons can be used to determine the mass of the primary particle. For such reconstruction of primary particle properties it is often necessary to simulate the air shower using Monte Carlo simulations. A simulation of the air shower as it is done in CORSIKA (Heck et al., 1998) or AIRES (Sciutto, 1999) uses the information on cross sections and interaction models derived with accelerator experiments to model the complete air shower. Since the energy of air shower particles exceeds the energy range reached by accelerators the required properties are extrapolated. This can lead to deviation between these models and the real data and therefore an exact reconstruction of the primary particle is difficult. This is also a reason why the mass composition for high energy cosmic rays is not as precise as the one for lower energies.

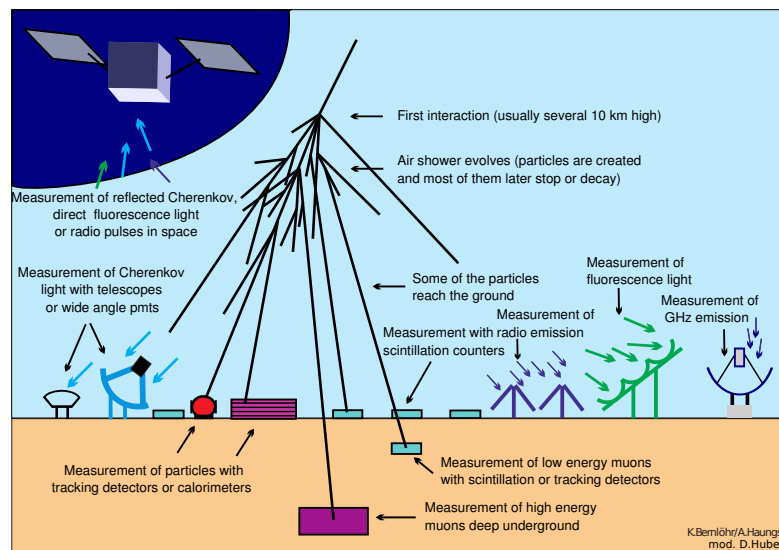


Figure 2.4: Overview of the different detection techniques for the measurement of air showers (Haungs et al., 2003).

## 2.3 Detection of high-energy cosmic rays

There are different methods to observe high-energy air shower as shown in figure 2.4. Nowadays often a combination of different techniques is used to get a complete picture of the air shower since each technique has its own strengths and weaknesses. In the following the most popular detection methods are described.

### 2.3.1 Particle detectors

The most established technique is to measure directly the secondary particles that reach the ground. Depending on the explored energy range an area of several hundred square metre to several thousand square kilometres is equipped with particle detectors. The various experiments use different detector techniques all measuring the footprint of the air shower at ground. At the Pierre Auger Observatory or the Haverah Park experiment (Lawrence et al., 1991) water Cherenkov tanks were used while the KASCADE-Grande experiment (Antoni et al., 2003; Apel et al., 2010) used different types of scintillators as well as calorimeters and tracking gas detectors. The direction of the primary particle can be reconstructed from the arrival times of the secondary particles in the detectors, the primary energy is connected with the total energy deposit and the mass can be determined when looking at the ratio of electron-to-muon number. Particle detectors have a high duty cycle, a very good angular resolution and they can reach energy resolutions of 20-30 % (Blümer et al., 2009). The mass resolution mainly depends whether a discrimination of muons and electrons is possible. This technique is suited for a wide energy range but highly depends on interaction models.

### 2.3.2 Fluorescence detectors

Fluorescence detectors do not measure the footprint of the air shower but the fluorescence light emitted during the whole evolution of the air shower. Relativistic air shower particles excite nitrogen molecules in the atmosphere. Excited molecules relax to the ground state by emitting ultra-violet light that can be detected by telescopes. Fluorescence detectors can measure the shower maximum and the shower energy more precise than particle detectors. The disadvantage is a worse direction reconstruction and the low duty cycle of only 10-15% because measurements are only possible in clear moonless nights. At the Pierre Auger Observatory four fluorescence telescopes (Abraham J. et al., 2010) are deployed with mirrors reflecting the light to photomultiplier cameras. From the characteristics of the signal a reconstruction of primary mass and energy is possible. While these measurements are little dependent on interaction models the signal strength strongly depends on atmospheric conditions that influence the transmission of the light.

### 2.3.3 Cherenkov detectors

Due to the non-unity refractive index of air Cherenkov light is emitted by the air shower. There are in principle two ways of detecting such light: Imaging telescopes like MAGIC (Aleksic et al., 2012) and H.E.S.S. (Hinton, 2004) and non-imaging ones like used in the Tunka-133 (Prosin et al., 2014) or the Yakutsk (Ivanov et al., 2009) experiment. The imaging telescopes detect the Cherenkov ring directly with mirror telescopes. The non-imaging experiments detect the flash of UV light with an array of photomultiplier tubes. Like for the fluorescence technique the advantages are a high sensitivity on shower maximum and energy with a low dependence on air shower models. But also only during clear, moonless nights the detection of the Cherenkov light is possible.

### 2.3.4 Radio detectors

While travelling through the Earth's atmosphere the electromagnetic component of the air shower emits radio signals during the whole shower evolution. Radio measurements are therefore sensitive to the longitudinal shower development and also to the shower maximum. Furthermore the amplitude of the signal is linearly correlated with the shower energy. Combining the advantage of a high duty cycle with the sensitivity on the primary particle properties the radio technique is very promising. But the efficiency of radio measurements highly depends on the angle between the incoming shower and the Earth's magnetic field due to the emission processes. Furthermore high radio noise in urban areas can lead to worse accuracy. This is the case for the LOPES (Apel et al., 2012a) experiment which is described in chapter 3. In the next section 2.4 the radio emission of air showers is explained in more detail.

## 2.4 Radio emission of cosmic-ray air showers

First activities in the field of radio emission already started in the 1960s, both theoretically (Askaryan, 1962; Kahn and Lerche, 1966) and experimentally (Jelley et al., 1965). Since other techniques like particle and fluorescence detection evolved faster and the correlation of radio properties with air shower characteristics showed problems these first activities stopped. With the development of digital signal processing the radio technique was revived in the early 2000s and got competitive with established detection methods (Huege, 2016). As a pioneering experiment LOPES provided the proof-of-principle for an interferometric measurement (Falcke et al., 2005) and developed many of the technologies and analysis approaches that made this success possible. In the last years the interest in radio detection increased and today several important air shower experiments also include radio antennas. The radio measurements provide additional information on air shower parameters like primary particle energy, mass and arrival direction, and this with a high duty cycle. Only during thunderstorms and very high atmospheric electric fields the radio emission is influenced that much that a reliable reconstruction of air shower properties is not possible (Apel et al., 2011a).

### 2.4.1 Basic properties of radio emission

The radio emission in an air shower is mainly caused by deflection of electrons and positrons in the Earth's magnetic field. For wavelengths smaller than the shower front this emission is coherent and adds up to a measurable pulse. The shower front has a thickness of a few metres, therefore the coherent emission is below 100 MHz. At these frequencies the amplitude of the pulse is proportional to the number of electrons in the shower and scales linearly with the primary energy (Huege, 2013). The pulse height also depends on the geometry of the air shower e.g. it decrease with an increased distance of the antenna to the shower axis or with smaller geomagnetic angle (the angle between the Earth's magnetic field and the air shower axis). To quantify these dependences the emission process needs to be understood in detail. The current state of research is discussed in section 2.4.2.

The radio wavefront provides information on the showers arrival direction and core. From the arrival times in the individual antennas these quantities can be determined. As a second-order effect the shape of the radio wavefront contains information on the shower maximum  $X_{\max}$  and therefore the primary mass. While the particle front is spherical recent studies show that the radio wavefront has a hyperbolic shape (Apel et al., 2014b). The opening angle of the asymptotic cone contains the information on the shower maximum: Heavy particles like iron have a bigger cross-section and therefore interact earlier in the atmosphere than light particles like proton. For radio emission this corresponds to a different distance to the source of the emission and is directly correlated with the opening angle of the wavefront which is smaller for light particles and bigger for heavy particles (Apel et al., 2014b).

The interaction height of the primary particle also affects the lateral distribution (LDF) which is the amplitude as a function of distance to shower axis. The slope of the lateral distribution is steeper for light particles than for heavy ones (Apel et al., 2014a). This dependence was also predicted by simulations, see Huege et al. (2008). The lateral distribution yields also information on the energy via the amplitude at a characteristic

distance at which the influence of the source distance, i.e., shower-to-shower fluctuations and the mass of the primary particle, is minimal. The higher the energy the higher the amplitude at this characteristic distance which has to be determined for each experiment individually. Due to its coherence the amplitude of the radio emission is expected to be proportional to the energy of the air shower. The amplitude and the slope can be derived by a fit to the lateral distribution. Due to the emission processes the lateral distribution is not symmetric, as explained in section 2.4.2. Different fitting functions are used by the various experiments. For many purposes, e.g. the comparison of LOPES data and CoREAS simulations, a simple one-dimensional exponential function is usable. Especially for an experiment like LOPES which suffers from high environmental noise and therefore has high measurement uncertainties. More precise measurements like done with LOFAR show that a non-rotationally symmetric two dimensional Gaussian function, taking into account east-west asymmetries, describes the true footprint up to a few percent (Nelles et al., 2015a).

### 2.4.2 Radio emission physics

The theory of radio emission evolved parallel to the experimental activities. Simulations of the expected radio pulses have been compared to measurements and so the assumptions and theories of radio emission could be verified. There are different approaches for radio simulations, from macroscopic to microscopic ones. The macroscopic approach is based on emission models using currents and net charge of the air shower, while microscopic models use full Monte Carlo simulation and calculate the radiation emitted by single electrons and positrons of the shower. An example for a macroscopic model is MGMR (de Vries et al., 2010), while e.g. CoREAS (Huege et al., 2013) and ZHAireS (Alvarez-Muñiz et al., 2012) use the microscopic approach. They all predict comparable results and give a consistent picture of the radio emission.

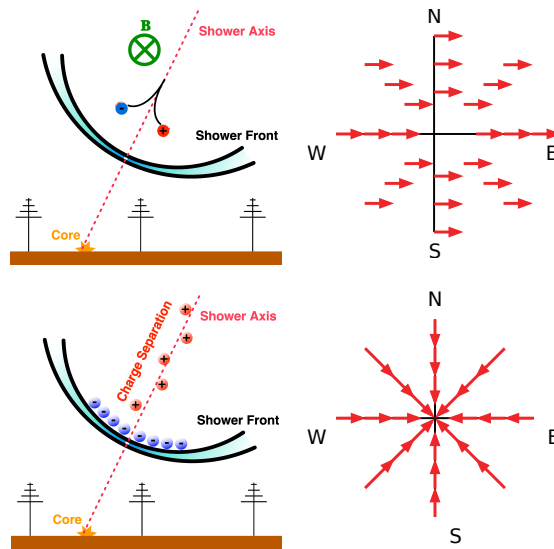


**Figure 2.5:** Schematic representation of the two main radio emission mechanisms of air showers. On the upper left the formation of time-varying transverse current is shown and on the upper right the corresponding pattern of the electric field vector. On the lower part the formation of the Askaryan effect and its corresponding electric field pattern is illustrated (Schoorlemmer, 2013; de Vries et al., 2012).

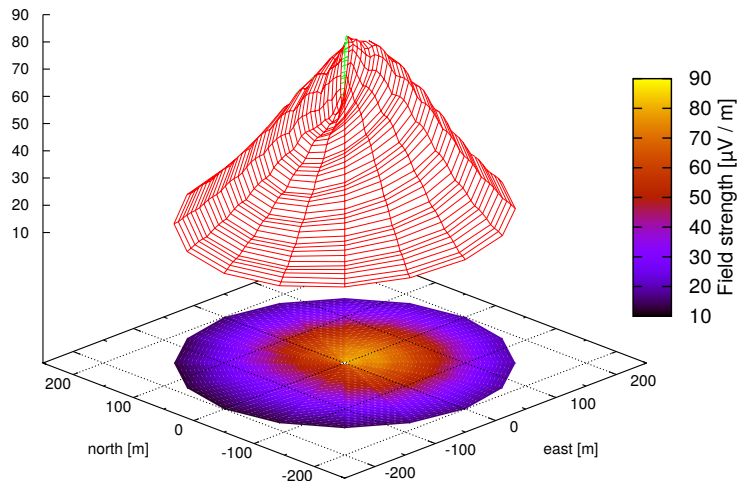


Figure 2.6: Footprint of the total field strength of a CoREAS simulated event for a vertical iron induced air shower with an energy of  $10^{17}$  eV in the frequency range from 40 to 80 MHz (Huege et al., 2013).

There are two main contributions to the radio emission:

- The **time-varying transverse currents** are caused by the acceleration of electrons and positrons in the geomagnetic field and the simultaneous deceleration by interactions with air molecules. This leads to a drift of electrons and positrons in different directions and thus induces transverse currents. These currents depend on the number of particles in the shower, therefore they grow up to the maximum of the shower and decline when the shower dies out. The radio emission originating from these time-varying transverse currents is linearly polarized and the electric field vector is oriented in the direction of the Lorentz force (Huege, 2014; Huege et al., 2012; Kahn and Lerche, 1966).
- The **time-varying net charge** is also called Askaryan effect. The number of electrons in the air shower is higher than the number of positive particles leading to a negative charge excess. This is mainly caused by the fact that the air molecules are ionized and while the ionizing electrons are carried away with the cascade the heavy positive ions stay behind. Furthermore the generated positrons of the shower annihilate with surrounding matter while the electrons are kept. Since the total number of particles changes during the evolution of the shower this leads to a time-varying net charge. The electric field vector is linear polarized, like the transverse currents, but radially oriented with respect to the shower axis (Huege, 2014; Scholten et al., 2008; Askaryan, 1962).

A schematic representation of these two main emission mechanisms is shown in figure 2.5. From there it is apparent that the superposition of these two effects leads to an asymmetric radio signal. Figure 2.6 shows the footprint simulated with the CoREAS Monte Carlo Code indicating this asymmetry.

For higher frequencies above 100 MHz a third effect becomes important:

- The **Cherenkov-like time compression** results from the refractive index of air and leads to different coherence conditions. Therefore the radio signals emitted

at different stages of the shower development can add up coherently at ground and an increased signal is seen at the Cherenkov angle (de Vries et al., 2011). This so-called Cherenkov ring yields additional information on the air shower characteristics.

Beside these main contributions several other effects could contribute to the radio signal. While they are negligible for air showers measured in the frequency range of several ten MHz they can be relevant for showers evolving in dense media and for other frequency ranges. For a complete picture these other effects are briefly discussed.

- Due to the Earth's magnetic field a separation of electrons and positrons is caused resulting in a **moving dipole**. Since it changes its strength the dipole emits a radio signal (Scholten et al., 2008).
- Particles are not only separated by the geomagnetic field but also deflected. Therefore they move on curved tracks and emit synchrotron-like radiation, called **geosynchrotron radiation** (Huege et al., 2012; Huege, T. and Falcke, H., 2003). The influence to the total signal at MHz frequencies is only very small but seems to get more important at GHz frequencies (Huege and James, 2013).
- Another emission mechanism is the **Cherenkov emission** for media with refractive index greater than one which should not be confused with the Cherenkov-like time compression. Particles moving faster than light in a medium emit Cherenkov radiation which becomes only significant for dense media.
- Another effect that influences the radio emission are strong atmospheric electric fields especially during thunderstorms. They can lead to signals much higher than from the geomagnetic effect (Buitink et al., 2007a; Ender, M. et al., 2009). The influence does not only depend on the strength of the electric field but also on the orientation relative to the shower axis (Gelb, 2012). For this reason data taken during strong atmospheric field conditions are not used for cosmic-ray analyses so far.

### 2.4.3 Experiments

First experiments to measure radio emission of air showers were built in the 1950s. Already then it was possible to show a dependence of the radio pulse on the Earth's magnetic field and an increase of the amplitude with increasing energy of the primary cosmic rays (Allan, 1971). For different reasons, e.g. huge differences in the amplitude between different experiments and insufficient theoretical understanding, further investigations were stopped. Around 2003, now with modern digital electronics, this detection method was revived and today many air shower experiments use the radio technique, often in addition to particle, Cherenkov- or fluorescence detectors. Below, some of these modern experiments are described briefly.

**LOPES** The LOFAR PrototypE Station experiment (Apel et al., 2012a) was located at the Karlsruhe Institute of Technology, Campus North, within the KASCADE-Grande experiment. It operated in the frequency range from 40 to 80 MHz and was externally triggered. A detailed description of the LOPES experiment can be found in chapter 3.

**LOFAR** **Low-Frequency Array** is mainly located in the Netherlands but also has some stations spread over different European countries e.g. Germany (van Haarlem, M. P. et al., 2013). Mainly build for radio astronomy, it can also be used as cosmic ray detector. Two different antenna types are used: Low-frequency antennas operating from 30 to 80 MHz and high-frequency antennas with a frequency range from 110 to 240 MHz. The antennas are grouped in stations consisting of almost 100 lowband and 50 highband antennas with several metres spacing. In the core of LOFAR several of these stations are located close together. There is also an array of scintillators located, the so called LORA extension (Thoudam et al., 2014). LORA provides a trigger for cosmic rays and basic air shower information, like the arrival time and geometry of the air shower and an estimation of the primary energy. The dense core of antennas allows a detailed measurement of the lateral distribution of radio signals.

**CODALEMA** Together with LOPES the **COsmic ray Detection Array with Logarithmic ElectroMagnetic Antennas** (Ravel et al., 2012) was the first modern experiment for radio air shower measurements. It is located at the radio observatory of Nançay in France and operates in the frequency range from 24 to 82 MHz. A simple array of scintillators provides a trigger for the radio antennas which were reconfigured several times. CODALEMA can benefit from a radio-quiet environment.

**AERA** As an extension to the Pierre Auger Observatory in Argentina the **Auger Engineering Radio Array** started operation in 2011 (Schröder et al., 2013a). Based on the experience gained with different prototype stations and provided by other experiments, like LOPES or CODALEMA, a layout with a dense spacing in the core and a wider spacing to the border had been chosen. The last antennas were installed in the beginning of 2015 and now AERA consists of around 150 antennas spread over an area of around 17 km<sup>2</sup>. Different antenna types are used measuring at a frequency range from 30 MHz to 80 MHz. Each antenna station consists of two orthogonal antennas measuring two polarizations of the air shower signal. The Pierre Auger Observatory with its sophisticated particle and fluorescence detectors is the perfect environment for hybrid air shower measurements.

**Tunka-Rex** The **Tunka-Radio** extension to the photomultiplier array Tunka-133 consists of more than 60 SALLAs (Small Aperiodic Loaded Loop Antennas) (Bezyazeev et al., 2015). With Tunka-Rex a cross-calibration of radio and Cherenkov signals of air showers is possible which gives the opportunity to determine the precision of radio measurements regarding energy and mass of the primary particles. Since the photomultiplier tubes measuring the Cherenkov signal are only operating in clear moonless nights an additional trigger from a scintillator array is now used during day.

**Yakutsk** At the Yakutsk air shower array the first radio measurements were done before 1989 and revived in 2008 (Knurenko and Petrov, 2015). Inside the particle array 12 antennas operating from 28 MHz to 40 MHz are installed.

**TREND** Like the name implies the main goal of the **Tianshan Radio Experiment for Neutrino Detection** is the measurement of neutrino-induced air showers

(Martineau-Huynh et al., 2012). Surrounded by mountains at an altitude of 2650 m the location is ideal for this technique: Tau-neutrinos interacting in the mountains induce horizontal air showers which can be detected by the 80 radio antennas. So far only a detection of high-energy cosmic rays was reported.

**ANITA** The balloon borne radio interferometer (**AN**tartic **Impulsive Transient Antenna**) has been built for the detection of high energy neutrinos (Hoover et al., 2010). High energy neutrinos induce cascades that generate radio emission in ice due to the Askaryan effect. With horn antennas attached to a balloon the radio signal from 300 MHz to 1200 MHz is measured above the Antarctic ice. ANITA III was launched at the end of 2014 and beside the search for neutrinos cosmic-ray measurements are possible (Nichol et al., 2011). These are the first broadband measurements of cosmic-ray radio emission.

**Experiments measuring microwave radio emission** Beside the MHz range also the GHz range is suitable for cosmic-ray radio measurements as it was shown by the **CROME** (**Cosmic-Ray Observation via Microwave Emission**) experiment (Šmída et al., 2014). CROME was located at the Karlsruhe Institute of Technology, Campus North, inside the KASCADE-Grande array. With dish antennas measuring the extended C band (~3.4 GHz to 4.2 GHz) over 30 events could be detected, triggered by KASCADE-Grande. Beside CROME also experiments in Argentina at the Pierre Auger Observatory are measuring in the GHz regime (Gaïor et al., 2013): MIDAS (Alvarez-Muñiz et al., 2013), AMBER (Gorham et al., 2008) and EASIER (Luis, P. Facal San et al., 2013).

# 3

## The LOPES experiment

LOPES (LOFAR PrototypE Station) was located in Karlsruhe, Germany, at the Campus North of the Karlsruhe Institute of Technology (KIT). This location was chosen to benefit from the particle detector KASCADE-Grande (Antoni et al., 2003; Apel et al., 2010). KASCADE consisted of 252 scintillator stations distributed regularly over an area of 200 m x 200 m. To be sensitive to the electron-muon ratio the outer stations had an additional muon detector. KASCADE was measuring cosmic rays with primary energies of  $10^{14}$  eV to  $10^{17}$  eV. To reach up to energies of around  $10^{18}$  eV KASCADE was extended to KASCADE-Grande with 37 additional stations distributed over an area of  $0.5 \text{ km}^2$ . Beside a trigger for the radio detectors on high energy cosmic rays KASCADE-Grande provided detailed information on the detected shower, like particle numbers, reconstructed energy, core and arrival direction. For the development of the new radio detection technique this information was essential. LOPES was built to provide the proof-of-principle for the detection of high energy cosmic rays with modern digital radio arrays using interferometric beamforming. After a successful measurement published in Falcke et al. (2005) detailed studies on the properties of such cosmic ray radio emission followed. For this purpose the LOPES experiment was redesigned several times to fulfil the changing requirements. Figure 3.1 shows a time-line of the different setups, explained in more detail in the next section.

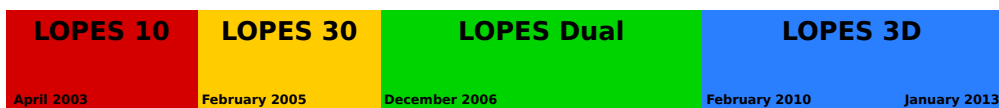
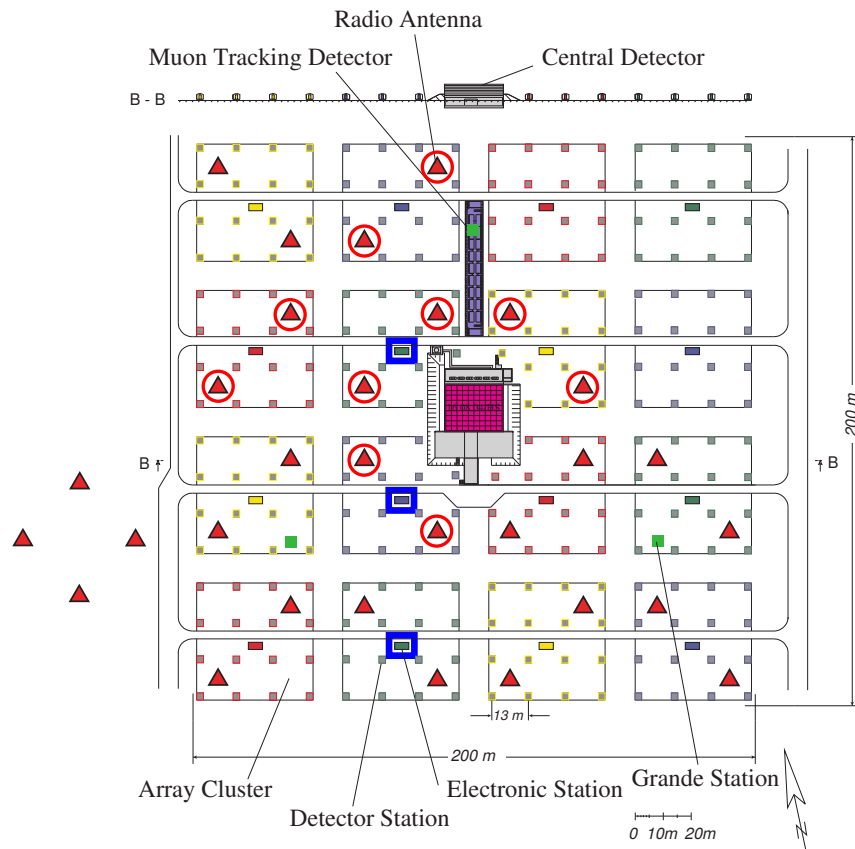


Figure 3.1: Overview of the different LOPES setups. Each setup is described in section 3.1.

### 3.1 Setups and previous results

LOPES started operation in April 2003 with ten antennas distributed over the KASCADE area, indicated with red circles in figure 3.2. The inverted-V-shaped dipole antennas, see figure 3.3, were all oriented in the east-west direction. This alignment was chosen as mainly east-west polarized emission was expected due to the geomagnetic effect. A frequency range from around 40 to 80 MHz was chosen since in this range coherent radio emission is expected and the radio background is relatively low. LOPES is externally triggered by KASCADE-Grande on high energy air showers with primary energies above  $\sim 10^{16.5}$  eV.



**Figure 3.2:** Layout of the LOPES 10 (red circle) and LOPES 30 (red triangle) antennas inside the KASCADE array (Horneffer, 2006).

Already with this very first setup several findings on fundamental properties of radio emission from air showers could be published. First of all the proof-of-principle for radio detection of air showers with digital interferometry was successful. Figure 3.4 shows an interferometric sky map with an air shower signal, visible as a bright point in the sky. The arrival direction is in good agreement with the one reconstructed by KASCADE. The sky map is obtained by calculating the cross-correlation beam (see section 3.2) for different points on a three-dimensional grid on the sky. Furthermore, the expected coherent emission in this frequency range, which results in a linear scaling of the radio emission with the energy, was confirmed (Falcke et al., 2005).



Figure 3.3: Inverted-V-shaped dipole antenna used for most LOPES setups.

With the extended LOPES 30, now with 30 east-west aligned antennas, a parametrization of the east-west signal, depending on energy, distance to shower axis and geomagnetic angle, was done which results in the following formula (Horneffer et al., 2007):

$$\epsilon_{EW} = 11 \cdot (1.16 + (1 - \cos \alpha)) \cos \theta \exp\left(\frac{-R_{SA}}{236 \text{ m}}\right) \left(\frac{E_p}{10^{17} \text{ eV}}\right)^{0.95} \left[\frac{\mu\text{V}}{\text{mMHz}}\right] \quad (3.1)$$

With:  $\alpha$  the geomagnetic angle,  $\theta$  the zenith angle,  $R_{SA}$  the mean distance of the antennas to the shower axis, and  $E_p$  the primary particle energy. The given fit parameters result from the fits which are shown in figure 3.5.

Using the data obtained with LOPES 30 further characteristics of the radio signals were investigated, like the angular resolution (Nigl et al., 2008a), the detection of inclined events (Petrovic et al., 2007) and the characteristics of the frequency spectrum (Nigl et al., 2008b). Detailed studies on the lateral distribution showed that an exponential behaviour fits for  $\sim 80\%$  of the events, while  $\sim 20\%$  show a flattening towards the shower core (Apel et al., 2010). Comparisons between data and simulations are based on these lateral distributions. The simulations obtained with the Monte-Carlo-Codes REAS2 and REAS3 use the geometry and energy as reconstructed by KASCADE-Grande. While the slope for REAS2 was too steep REAS3 simulations often fit nicely (Huege et al., 2012). Also a comparison on the absolute height of the signal was possible since an absolute amplitude calibration was performed. Details on this calibration are shown in chapter 5.

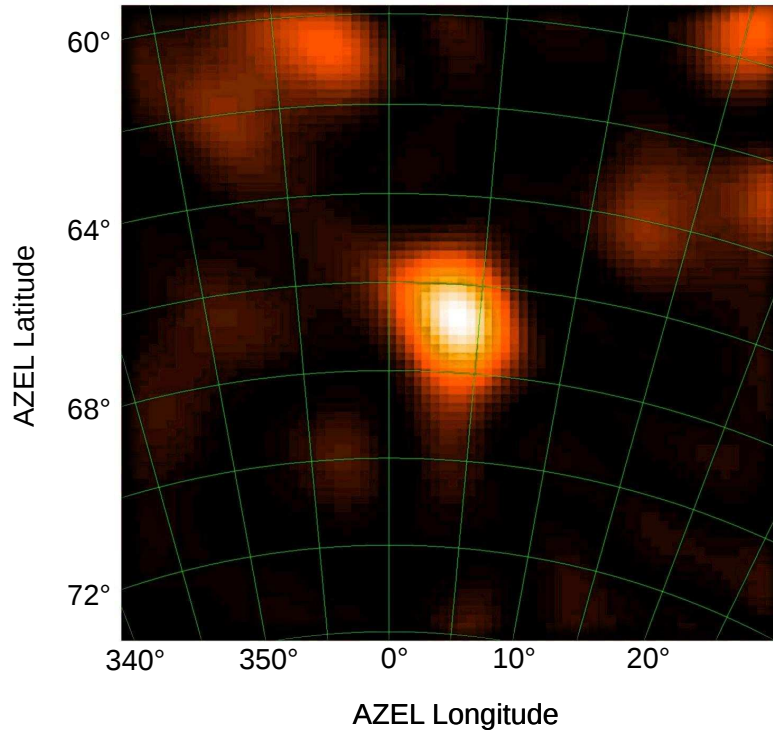


Figure 3.4: Sky map of the cross-correlation beam measured with LOPES. The signal originating from the air shower is clearly visible and the reconstructed arrival direction is in agreement with KASCADE (Falcke et al., 2005).

Further investigations were done on the influence of thunderstorms on the radio pulse height. With data obtained from lightning maps times of thunderstorm were identified and an increased pulse height was visible for most events (Buitink et al., 2005, 2007b). Subsequently an e-field mill was installed at the detection site to monitor the electric field and thunderstorm events could be excluded in the standard event selection.

For the next setup, called LOPES Dual, half of the antennas were rotated to be north-south aligned. In principle this allows the measurement of the complete electric field vector. Mainly for technical reasons it was decided to only have five stations with both, east-west and north-south aligned antennas while the remaining twenty antennas were singly distributed inside the KASCADE area, as shown in figure 3.6. This led to the problem that still a vectorial reconstruction of the electric field vector was not possible, as explained in detail in section 3.3. Anyhow an analysis based on the single components was possible, now also for the north-south component.

With this new data set also investigations on the reconstruction of the shower maximum  $X_{\max}$  were performed. Two independent methods were developed, one based on the slope of the lateral distribution (Apel et al., 2014a) and one based on the opening angle of the radio wavefront (Apel et al., 2014b). The results of both methods are in agreement with each other and also with other air shower experiments but suffer from large systematic uncertainties, see figure 3.7.

For the last setup, LOPES 3D (Apel et al., 2012a), the antennas were exchanged by Tripoles while the electronic system was kept the same. Now really the full three-

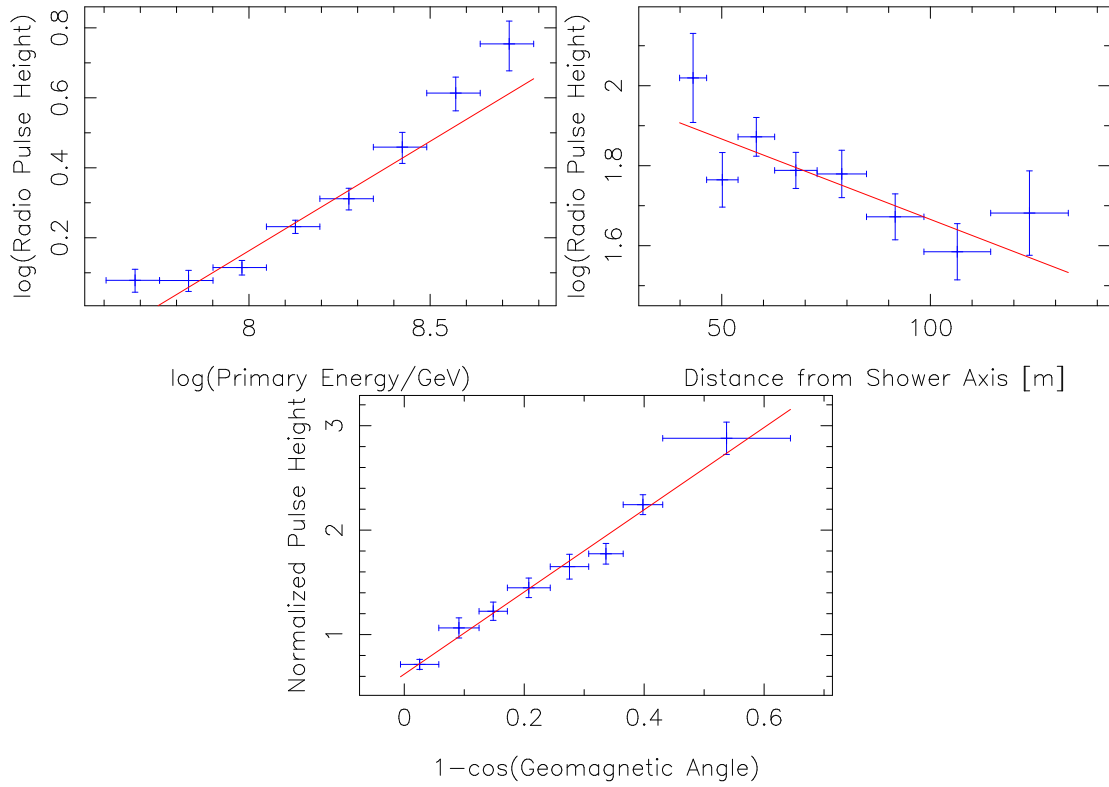


Figure 3.5: Parametrization of the east-west signal for the LOPES 30 data resulting in formula 3.1 (Hornefer et al., 2007).

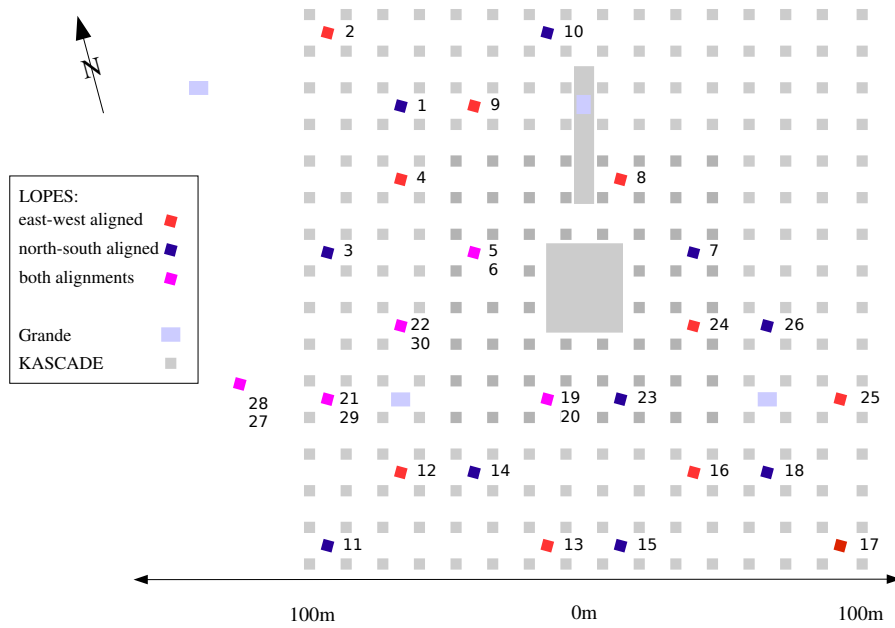
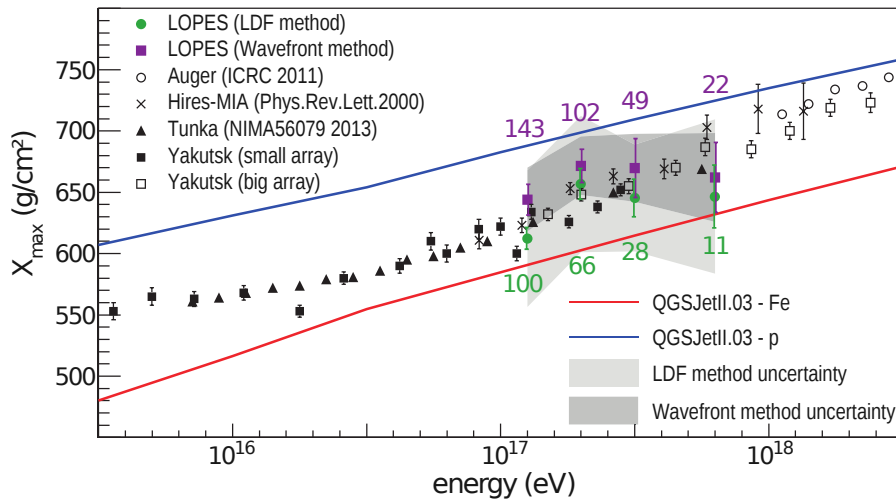


Figure 3.6: Layout of the LOPES Dual antennas at the KASCADE-Grande site (Nehls, 2008).



**Figure 3.7:** Mean  $X_{\max}$  values as a function of energy obtained with two different methods for LOPES, the LDF method based on the slope of the lateral distribution and the wavefront method based on the cone angle of the radio wavefront. The results of LOPES are consistent among themselves and are consistent with the results by other experiments and predictions by simulations (Schröder et al., 2015).

dimensional electric field vector could be measured. Although the measurement time was around three years only poor statistics were obtained due to a tremendous increase of noise related to a big construction site next to the array. In figure 3.8 the reconstructed electric field vector for one example event is shown.

With the shutdown of the hosting KASCADE-Grande array also LOPES was dismantled in 2013. Data analysis is still going on up to now and a closing analysis is done in this work. The data is supposed to be published in the public data center for KASCADE-Grande KCDC (Haungs et al., 2015).

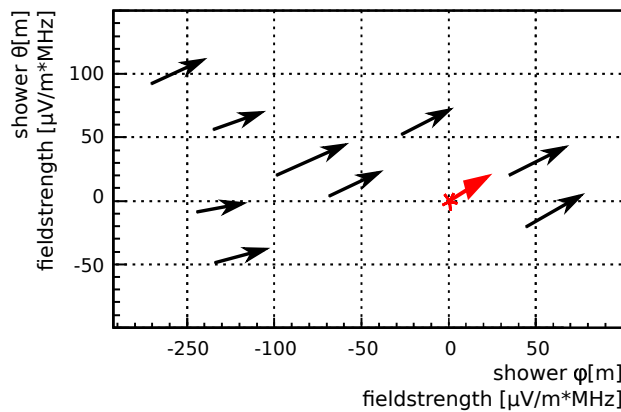


**Figure 3.8:** Reconstructed electric field vector for one example event. The direction of the black arrows indicate the direction of the vector in the shower plane with the antenna position as starting point and the length is correlated with the field strength. The red arrow indicates the shower core and the expected orientation of the electric field according to the  $\vec{v} \times \vec{B}$  model. The length of the red arrow is arbitrary (Huber, 2014).

## 3.2 Standard analysis pipeline

In this chapter the standard analysis pipeline is explained which is part of the open-source LOFAR software package. This pipeline includes the application of the detector influence and an interferometric reconstruction of the radio signal.

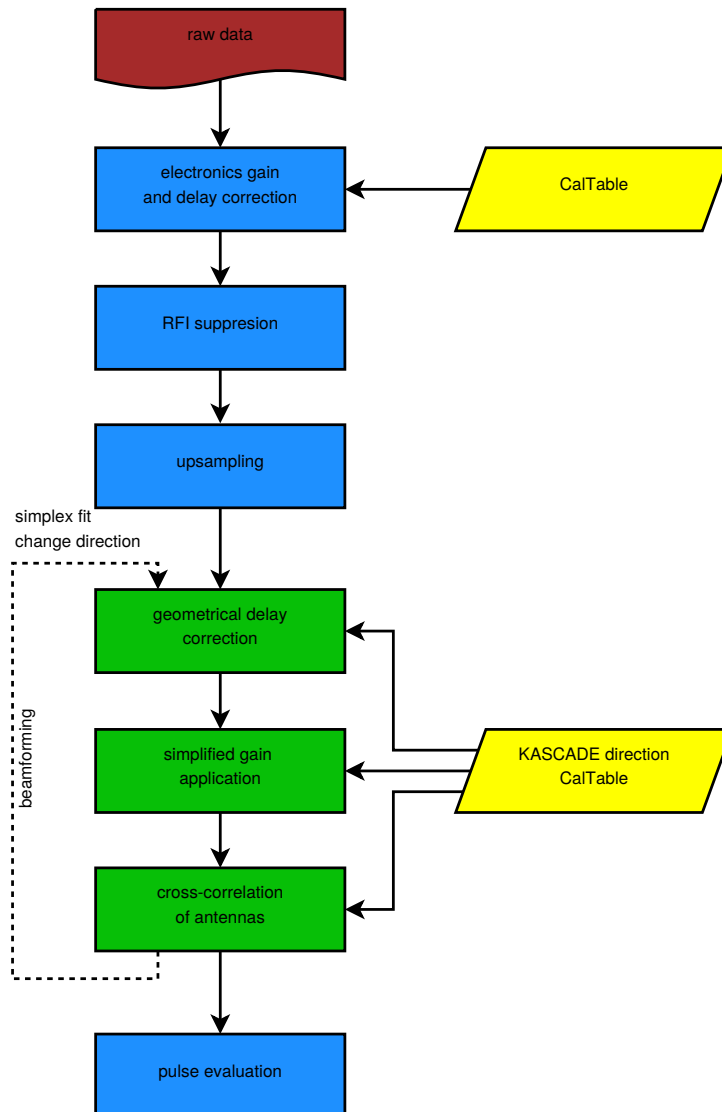


**Figure 3.9:** Flowchart of the standard LOPES analysis pipeline. The binary data file is shown in red, the data treatment in blue, input from external sources in yellow and the iterative beamforming and simplex-fit procedure in green. Adopted from Huber (2014)

### Pre-selection of events

Before running the standard analysis pipeline a pre-selection of events is reasonable. To have reliable reconstruction parameters a cut on the event quality specified by KASCADE-Grande is necessary. Additionally a cut on air shower parameters can reduce the number of processed events without measurable radio signal. The cuts and their impact on the event number is shown in section 3.5.

### Electronics gain and delay correction

Figure 3.9 shows a flowchart of the typical analysis procedure. The input for the analysis pipeline are the binary LOPES event files. In the first step the signal is corrected for the detector influences of the electronic chain and for induced delays. This is done in the frequency domain. The amplification factor of the amplitude is determined with the absolute amplitude calibration described in chapter 5. The delay induced by the electronics has been measured directly and an additional timing calibration on an event-by-event basis is performed using the beacon, see Schröder et al. (2010). Then the data is filtered to the designed bandwidth of 43 to 74 MHz to correct for different filter modules.

### RFI suppression and upsampling

Afterwards the quality of the signal is improved by narrowband RFI (radio frequency interference) suppression and optional upsampling. The narrowband RFI suppression is possible since air showers emit a broadband signal while narrowband signals are mainly man-made and can be cut out. LOPES measures in the second Nyquist domain and an upsampling allows to calculate additional data points to get higher resolution. This is done by the zero-padding methods as described in Bracewell (1986).

### Iterative beamforming with direction and wavefront reconstruction

The next step is an iterative procedure wherein the gain of the antenna is applied and the beamforming takes place. According to the arrival direction and the distance of the air shower a geometrical delay of the signal in each antenna is calculated. This delay depends on the shape of the radio wavefront. Investigations on measured and simulated radio signals show that a hyperbolic shape is the best approximation for the radio wavefront (Apel et al., 2014b). Such a hyperbolic shape is parametrized using the following formula:

$$c\tau(d, z_s) = \sqrt{(d \sin \rho)^2 + (cb)^2} + z_s \cos \rho + cb \quad (3.2)$$

With the lateral distance of the antenna to the shower axis  $d$ , the distance of the antenna to the shower plane  $z_s$  and the two parameters  $\rho$  for the opening angle of the cone and  $b$  describing the offset.

According to the expected arrival time of the signal, calculated with formula 3.2, the time traces are shifted in such a way that the radio signal arrives at the same time

in all antennas.

Then the directional sensitivity of the antenna is considered by the application of the antenna gain. Details on this application and the reconstruction of the electric field can be found in section 3.3.

In a final step the cross correlation beam, CC-beam, is calculated using the following equation:

$$CC(t) = \pm \sqrt{\frac{1}{N_{\text{pairs}}} \sum_{i=1}^{N-1} \sum_{i>j}^N s_i(t) \cdot s_j(t)} \quad (3.3)$$

With  $N$  being the number of traces,  $N_{\text{pairs}}$  the number of unique pairs, the time  $t$  and the time-shifted traces of the particular antennas  $s_{i/j}(t)$ .

To suppress fine structure coming from the bandpass filtering a block-averaging over three samples is applied to the CC-beam. Then the arrival direction and the distance are changed according to a defined grid on the sky and the CC-beam is maximized using a simplex fit. The arrival direction reconstructed by KASCADE-Grande is used as a starting value. The change of the arrival direction and the distance to the source is correlated with a change of  $\rho$ . In the end a Gaussian function is fitted to the CC-beam which provides the information on time and height of the CC-beam.

### Pulse evaluation

The calculation of the CC-beam enables the identification of the pulse induced by the air shower: RFI, e.g., induced by the KASCADE detectors, is usually incoherent as demonstrated in figure 3.10. Plot a) shows the time-shifted traces of all east-west aligned antennas measuring at that time. The coherent radio pulse from an air shower is clearly visible although the signal-to-noise ratio is low. In plot b) the calculated CC- and the power-beam are presented. This also shows that although the power of the noise is as high, even higher than the signal, the CC-beam allows to identify the time of the air shower signal. This information is used to get the radio pulse amplitude measured by individual antennas. The maximum of the Hilbert envelope closest to the arrival time of the air showers is taken. Plot c) shows that this would be hardly possible with the information from only one antenna.

With the timing information from the CC-beam the maximum pulse amplitudes of all antennas are determined by choosing the nearest local maxima in the trace. For the amplitude of the single antennas also the influence of noise is considered: Investigations show that noise can increase or decrease the signal depending on the signal-to-noise ratio and a noise correction is applied individually for each antenna depending on the signal-to-noise ratio. For details of the noise correction see Schröder et al. (2012).

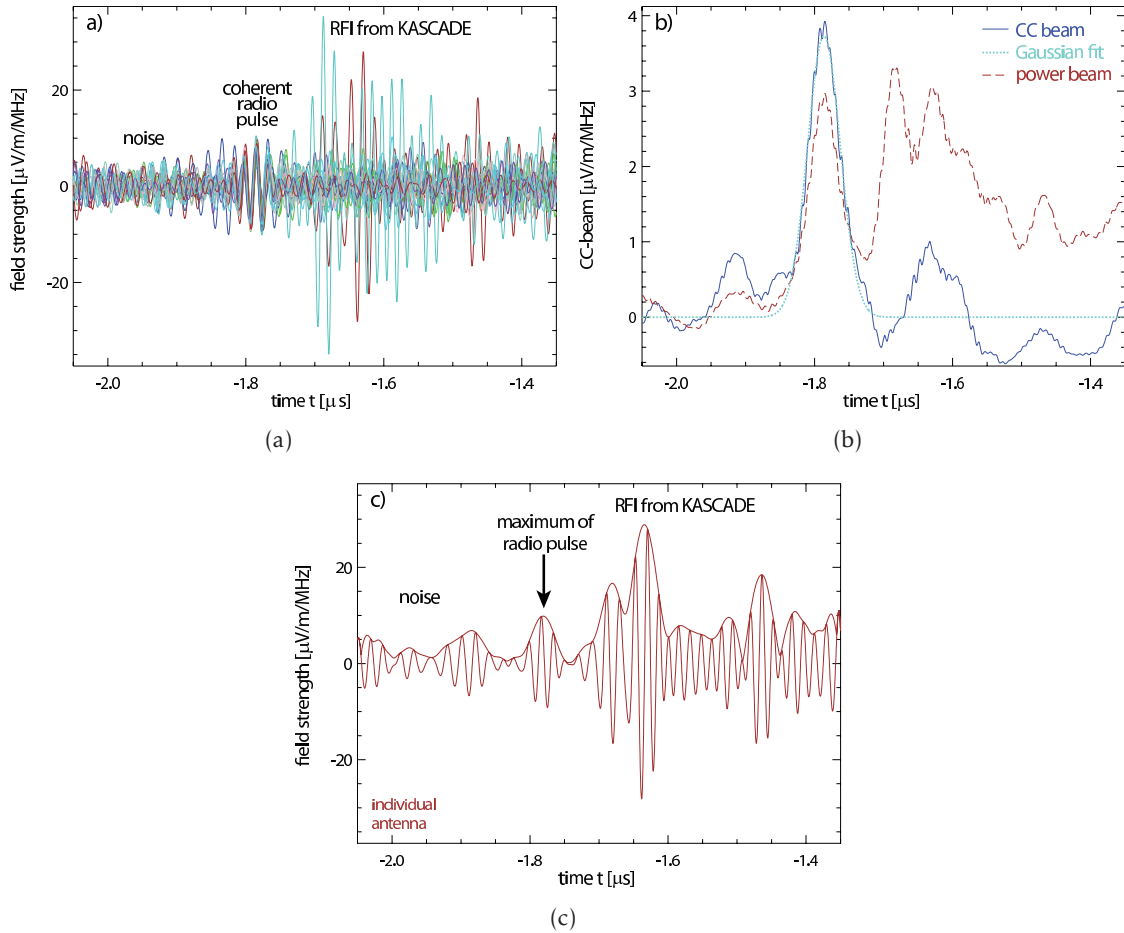


**Figure 3.10:** Example event from 2005 measured with east-west aligned antennas: a) electrical field strength traces of all antennas, b) CC-beam and power-beam, c) electrical field strength trace in an individual antenna with a Hilbert envelope (Apel et al., 2013a). The amplitude of the CC-beam and power-beam is lower than the amplitude of the individual antennas due to the applied block averaging.

### Output of reconstruction pipeline

The final output also contains information from KASCADE-Grande and all other quantities calculated during the analysis pipeline like e.g. time and amplitude of the CC- and power-beam. This output can be used for external analysis. Additionally plots showing the time traces, frequency spectra and calculated beams are saved.

Furthermore it is possible to plot and fit the lateral distribution within the standard pipeline like shown in figure 3.11. There are two options for the fit, an exponential or a Gaussian function. Both are a simplification of the true lateral function which is not symmetric like described in section 2.4. In principle the usage of a symmetrical function results in a wider spread of the data points around this function or in a systematic shift of the amplitude. The first is the case if the shower core is in the middle of the antenna array while the absolute shift occurs if all antennas are at one side of the shower. For LOPES most of the showers have a core inside the array and the degradation of the analysis when using a symmetrical function is negligible and the influence

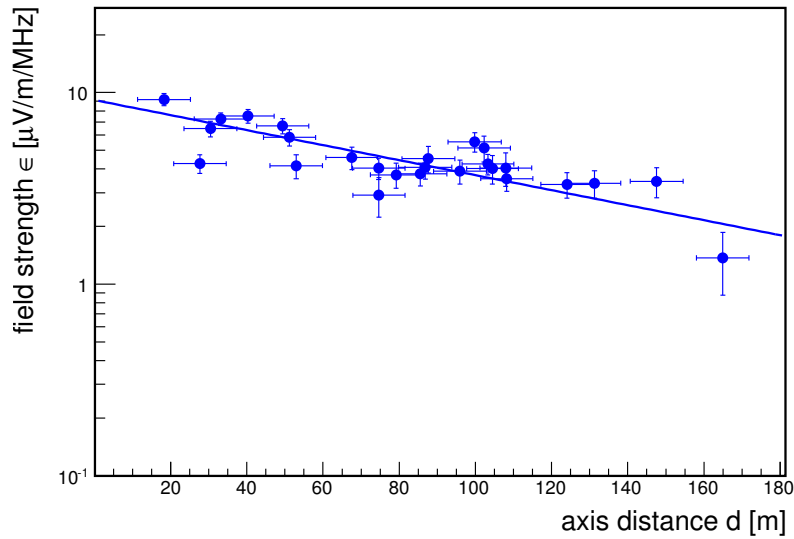


Figure 3.11: Lateral distribution fitted with an exponential function with  $\varepsilon_{100} = 3.7 \mu\text{V}/(\text{mMHz})$  and  $\eta = 0.009/\text{m}$ .

is much smaller than the uncertainty of the amplitude, see also Apel et al. (2014a). For most investigations the exponential function 3.4 is used (Apel et al., 2012c).

$$\varepsilon(d) = \varepsilon_{100} \cdot \exp[-\eta(d - 100 \text{ m})] \quad (3.4)$$

The fit parameters  $\varepsilon_{100}$ , the amplitude at 100 m axis distance, and  $\eta$ , the lateral slope, are also given in the output file and can be used for further investigations.

Furthermore a lateral time distribution of the signal can be calculated. This is the time of the signal in each antenna as a function of the distance to the shower axis in a plane perpendicular to the shower axis. This shows in principle the time difference between a planar wavefront and the true wavefront. A fit to this lateral time distribution is done using the hyperbola formula 3.2. A detailed description on the reconstruction of the wavefront can be found in Apel et al. (2014b). For the lateral time distribution a zero-time needs to be defined. Theoretically this is the time when the wavefront hits the ground. This cannot be determined directly from the measurements. Therefore the zero-time is defined by the maximum time of the CC-beam. Due to this definition and due to noise the lateral time distribution suffers from high uncertainties. Therefore the fit on the lateral time distribution is mostly used for simulation studies while for data analysis the cone angle reconstructed from the former shown beamforming is used.

3.2.1 Summary of reconstructed radio emission parameters

For further analysis four of the reconstructed parameters are mainly used: From the beamforming the amplitude of the CC-beam and the cone angle are used and from the lateral distribution the amplitude parameter  $\epsilon_{100}$  and the slope parameter  $\eta$  are derived.

The amplitude parameter  $\epsilon_{100}$  and the CC-beam amplitude both mainly depend on the energy. But while  $\epsilon_{100}$  should be independent from the mean distance of the antennas to the shower axis the CC-beam amplitude decreases with higher distances since it can be considered as the mean amplitude of all antennas at their mean distance. Further differences occur due to the block-averaging done for the beamforming. This leads to a lowering of the CC-beam amplitude compared to the amplitude of the lateral distribution by a factor of  $\sim 2$ . Figure 3.12 shows the relation of  $\epsilon_{100}$  and the distance-corrected CC-beam amplitude. While the CC-beam amplitude can be used also for low signal-to-noise ratios the advantage of  $\epsilon_{100}$  is its smaller dependence on the mean axis distance.

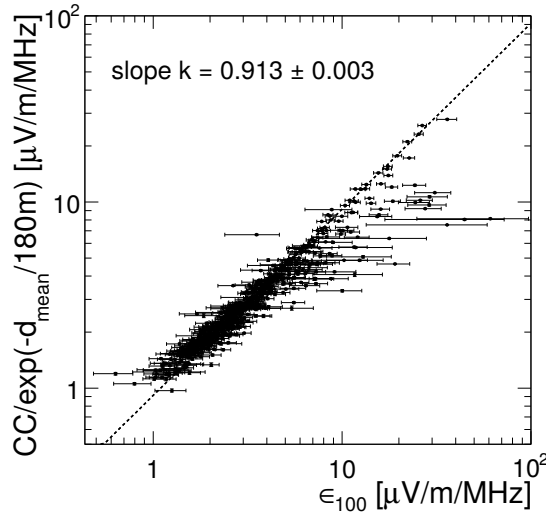


Figure 3.12: Corrected CC-beam amplitude versus the amplitude parameter  $\epsilon_{100}$ . The dashed line is a linear fit with the slope  $k$ .

The cone angle  $\rho_{CC}$  and the slope parameter  $\eta$  are two independent quantities both sensitive to the shower evolution and therefore the depth of shower maximum. The cone angle  $\rho$  can also be determined by a fit to the lateral time distribution but this suffers from high uncertainties for data.

In the appendix A histograms of the described quantities are shown for the complete LOPES data set.

### 3.3 Reconstruction of electric field components

Mathematically the measurement of the electric field is its projection on the antenna plane considering the effective antenna height. The signal measured in the antenna  $S_{ant}$  [V] is calculated with the dot product of the electric field vector  $\vec{E}$  [V/m] and the effective height of the antenna  $\vec{H}$  [m].

$$S_{ant} = \vec{E} \cdot \vec{H} \quad (3.5)$$

This is in principle a 3-dimensional equation system which can be reduced to two dimensions in the shower coordinate system (see figure 3.13) because the radio emission of air showers is a transverse wave and there is no electric field component along the shower axis. A rotation to shower coordinates is possible if the arrival direction of the air shower is known. For a reconstruction of the electric field components still at least two independent measurements at the same position are necessary. For the LOPES experiment this requirement was not generally fulfilled. Even during the dual polarized setup only five stations are equipped with both, a north-south and east-west aligned antenna, while the other stations are only equipped with one or the other. To anyhow reconstruct the electric field components a simplified reconstruction is used.

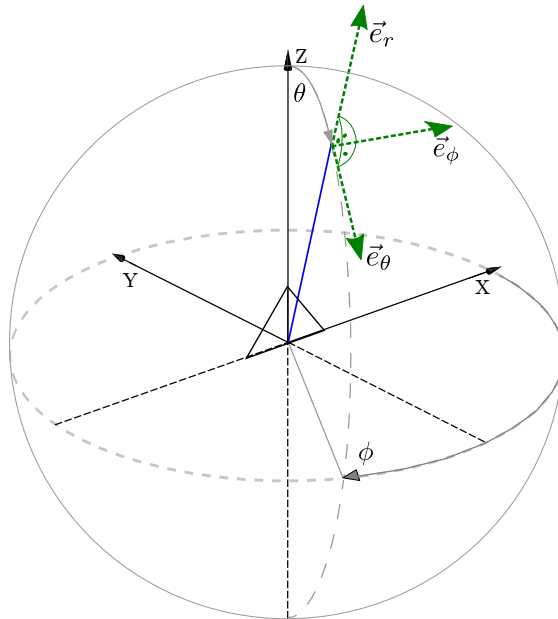


**Figure 3.13:** Sketch of the shower coordinate system with a LOPES antenna at the center. The direction of the incoming shower is defined by the azimuth angle  $\phi$  and the zenith angle  $\theta$  with  $\phi = 0^\circ$  pointing to north and  $\phi = 90^\circ$  to east. Along the  $\vec{e}_r$  axis no signal is expected.

The effective antenna height is proportional to the square root of the gain  $\vec{G}$  of the antenna which describes the directional sensitivity of the antenna. This gain can be expressed in shower coordinates, see figure 3.13, by two components  $G_\phi$  and  $G_\theta$ :

$$H_i = \sqrt{\frac{c}{4\pi\mu_0\nu^2}} \cdot G_i \quad \text{with } i = \varphi, \theta$$

$$\vec{G} = \begin{pmatrix} G_\varphi \\ G_\theta \end{pmatrix} \quad (3.6)$$

For the simplified reconstruction a “total gain” is used, calculated like:

$$G_{\text{tot}} = G_\varphi + G_\theta \quad (3.7)$$

From this total gain the electric field component is calculated with the following formula:

$$E_{\text{ant}} = \sqrt{\frac{4\pi\mu_0\nu^2}{c}} \frac{S_{\text{ant}}}{\sqrt{G_{\text{tot,ant}}}} \quad (3.8)$$

The reconstructed electric field component corresponds to either an east-west or north-south aligned antenna but is not exactly the east-west respectively north-south component of the electric field. For a comparison with simulations it is assumed that the electric field component calculated from the east-west aligned antenna is comparable with the east-west component of the electric field. The performance of the simplification depends on the interaction of the polarization of the air shower with the gain of the antenna. Both depend themselves on the geometry of the air shower, therefore also a dependence of the accuracy of the simplification on geometry is expected. How precise this simplification reconstructs the true amplitudes is not known so far and is investigated within this work.

### 3.4 Status before improved analysis

LOPES was originally built for a proof-of-principle and not with the idea of providing high-quality air shower measurements. During operation time it turned out that the available data is actually providing more information than expected and detailed studies of the characteristics of air shower radio emission were performed. As shown in section 3.1 LOPES was very successful and played a major role bringing forward the field of radio detection. But especially in the beginning the analysis was not based on a common structure and even an automatized events selection was missing and several open questions remained:

- Is the simplified reconstruction really valid and does it provide the correct electric field component?
- How precise is this reconstruction and how does it influences the results?
- How does noise influence the signal and is the application of the noise correction sufficient?
- How can we perform an interferometric beamforming using simulations?

- Some analyses are based on simulation studies with different treatment of data and simulations, e.g., the calculation of the cone angle is once done using the lateral time distribution and once using beamforming. Is it possible to do these analyses based on quantities derived in the same way for data and simulations?
- Where does the difference in the amplitude reconstructed by LOPES and simulated by CoREAS come from?

Especially the last question is very important since the comparison of data with state-of-the-art simulations for air shower radio emission was all the time an important aspect. When starting this work the REAS2 simulation code was common which was further developed to REAS3 and later was implemented to CORSIKA (Heck et al., 1998) to the now used CoREAS code (Huege et al., 2007; Ludwig and Huege, 2011; Huege et al., 2013). The comparison of LOPES lateral distributions with simulated ones from REAS2 showed some discrepancies, mainly for the slope of the lateral distribution. On average measured events have a flatter slope compared to REAS2 and there are even some events with a decreasing slope towards the shower core, which was not seen in the simulations (Nehls, 2008). With REAS3 this decreasing slope also appears in the simulations and in 2013 a comparison of data and simulations was published showing good agreement of LOPES data with REAS3.11 simulations (Apel et al., 2013a). Not only a comparison with REAS3.11 but also a comparison with the newly developed CoREAS code was performed. The slope of the lateral distribution is similar for REAS3 and CoREAS and both predict the measured slope very well. However the amplitudes predicted by CoREAS are about a factor of two lower than those predicted by REAS3. While REAS is based on histograms of the particle distributions provided by CORSIKA, CoREAS is directly implemented in CORSIKA. Therefore the CoREAS code was trusted to predict the correct amplitudes. But compared to LOPES data a difference by a factor of  $\sim 2.5$  was observed for CoREAS-simulated amplitudes, see also figure 3.14. The discrepancies of LOPES data and simulations always led to the question whether there are any unclear systematics in the LOPES data and the corresponding analysis or whether there is a real divergence between data and simulations which would mean that the emission physics were not fully understood. But only if the radio emission physics are understood the radio measurements can provide an independent energy reconstruction. At that time no other experiment could answer these question due to missing amplitude calibrations. One aim of this work was to investigate all steps in the analysis to exclude any inconsistency coming from the LOPES reconstruction. A qualitative and quantitative agreement of data and simulation is of high importance for the understanding of the radio emission of cosmic rays. Only if the radio emission is correctly understood the full potential of this detection technique can be used. Comparisons with simulations that are based on first-principles calculations like CoREAS provide an independent determination of the cosmic ray energy scale which gives complementary information to particle or fluorescence detectors. Nowadays such analyses are done with AERA, see Aab et al. (2016a), and show once more the advantage of hybrid detection including radio measurements. To answer all the above questions and to rule out any inconsistency within the LOPES analysis pipeline, the complete analysis procedure previously used in LOPES was scrutinized, including the amplitude calibration, and a detector simulation was developed. After this review the open questions can be answered. The review starts with providing

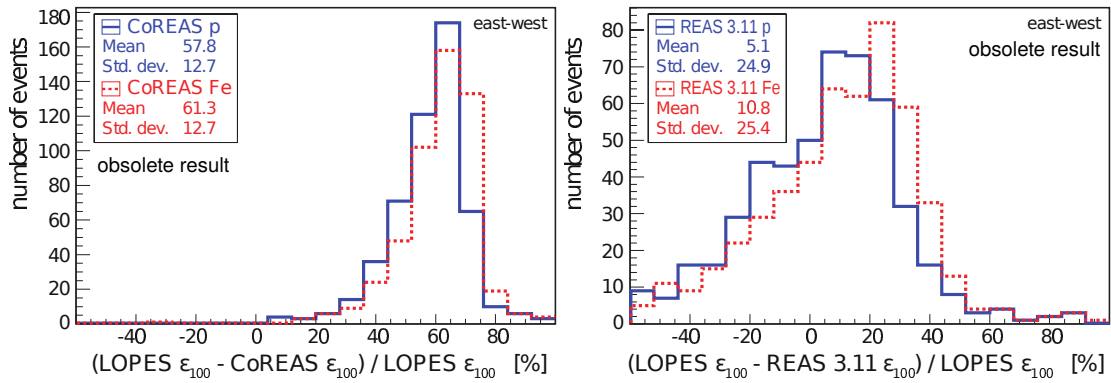


Figure 3.14: Relative deviation of the amplitude parameter  $\epsilon_{100}$  for LOPES data and simulations. Left the comparison with CoREAS simulations is shown and on the right with REAS3.11 (Apel et al., 2013a).

a common basis for future analyses and in the end an improved analysis is provided. Overall the following topics are discussed:

**Basic event selection** So far the event selection was done by eye which is of course very subjective. Furthermore, with increasing statistics it was absolutely necessary to automatize the selection procedure. A pre-selection based on KASCADE-Grande parameters as well as a quality selection based on radio quantities was developed and the results are presented in section 3.5.

**Detector simulation** A detailed detector simulation is used to apply the detector response to the simulations. The output can then be used as input for the standard LOPES pipeline. With such a detector simulation different aspects can be investigated. First of all it allows to compare the true east-west signal from simulations with the reconstructed east-west signal from the LOPES pipeline. This allows to quantify the impact of the simplified reconstruction and to identify any inconsistencies within the reconstruction of the amplitudes of single antennas. Another aspect is the influence of noise on the reconstructed parameters. Since the detector description allows to add measured noise to simulation its impact can be tested and the implemented noise correction can be revised. Former results were partly based on different reconstruction method for data and simulations, mainly since no interferometric analysis was possible for simulations. Using the detector simulation also the standard reconstruction pipeline with the interferometric analysis can be used for simulations. This provides the possibility of applying the same analysis method on data and simulations. This is discussed in chapter 4

**Amplitude Calibration** The amplitude calibration can not be tested with the detector simulations since it is convolved within the detector simulation and deconvolved within the standard reconstruction. Therefore it is separately reviewed. It consists of two main parts: The gain pattern of the antenna, which is simulated, and the absolute calibration, which is measured with an external reference source. Both parts were overhauled and the results are presented in chapter 5.

**Influence on former results** After reviewing the whole analysis procedure one important question is how the results and improvements influence former results.

Therefore a comparison of data and simulations and the reconstruction of air shower characteristics are repeated and expanded with an up-to-date improved analysis pipeline and using the detector simulation. This is done in chapter 6.

### 3.5 Event selection

LOPES measured in total for ten years with different setups. For the current analysis data taken from December 2005 to October 2009 is used. Before December 2005 no proper amplitude calibration is available and after October 2009 the reconfiguration to the Tripole setup started and due to the different antenna type no combined analysis was done.

Starting with more than 4.5 million events triggered by KASCADE and KASCADE-Grande the number of events is reduced by applying different quality cuts. First of all a successful reconstruction by KASCADE-Grande is required, applying their standard quality cuts as listed in Cossavella (2009). Beside some hardware cuts these are mainly cuts on the core position which must be either inside the KASCADE or KASCADE-Grande fiducial area, a cut on a zenith angle below  $45^\circ$  and a cut on the age parameter. Since the number of events is still quite high, with most of the events below the detection threshold of LOPES, further possible cuts are investigated to reduce computational time. To this end, a complete data set from a certain time period without additional cuts is analysed with the standard analysis pipeline. Afterwards it is investigated how many of the analysed events survive a certain cut on the signal-to-noise ratio of the CC-beam. The cumulative number of events above a certain signal-to-noise ratio is plotted as a function of this signal-to-noise ratio. From the selection by eye it was found that events with a signal-to-noise ratio of around ten are actually measurable with LOPES and should not be rejected by an additional cut. The total number of events defines the calculation time and should be reduced by an additional cut. Different cuts are applied on the data set and the impact on the cumulative number of events above the signal-to-noise ratio is studied. An additional energy cut on energies above  $10^{17}$  eV was found to be optimal to reduce computational time drastically with only losing a minor number of actual measurable events with a minimum signal-to-noise ratio of ten. Figure 3.15 shows how the number of events for this cut is reduced. While the total number of events is reduced by a factor of two the number of events above a signal-to-noise ratio of ten is almost the same. For most of the analyses even a signal-to-noise ratio of 14 is required where the impact of the additional cut is even lower. The additional energy cut reduces the total number of events to  $\sim 4000$ .

These preselected events are processed with the standard analysis pipeline and further quality cuts are applied. For events with measurement of the atmospheric electric field, which are all events after 2006, an atmospheric electric field below 3000 V/m is required. It turned out that just a simple cut on the signal-to-noise ratio of the CC-beam is not sufficient but also the fraction of power in the CC-beam compared to the total power is important. The fraction of power in the CC-beam has to be at least 80% of the total power. The signal-to-noise ratio depends on the number of antennas available for the individual event due to the normalization of the CC-beam, see formula 3.3, so the signal-to-noise ratio is normalized to the number of available antennas with the factor  $\sqrt{N_{ant}/30}$ . The ratio itself can be chosen for each analysis individually depending

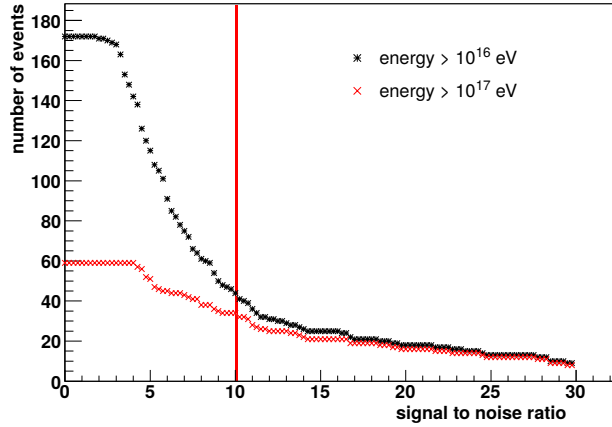


Figure 3.15: Number of events that pass a certain signal-to-noise ratio for two different energy cuts. The red line indicates the minimal required signal-to-noise ratio for a detectable radio event.

Table 3.1: Number of events after applying different quality cuts grouped into the different LOPES setups and divided into KASCADE (K) and KASCADE-Grande (G) selections.

setup	LOPES 30 K	LOPES 30 G	LOPES Dual K	LOPES Dual G	sum
triggered events	978,158		3,527,705		4,505,863
quality cuts KG	564,969	41,758	1,902,854	326,799	2,791,727
energy > $10^{17}$ eV	547	757	1,410	2,379	4,092
atmospheric E-field < 3 kV/m	546	754	1,390	2,344	4,043
quality cuts CC-beam	91	40	244	186	527

whether only high quality events are needed or higher statics. For most analyses a value of 14 is chosen like for the event numbers shown in table 3.1.

### 3.5.1 Simulations of measured events

For each of the remaining 527 events corresponding CoREAS simulations were performed, using the CORSIKA version 7.3 (Heck et al., 1998) with the interaction models QGSJet II.03 (Ostapchenko, 2006) and FLUKA (Battistoni et al., 2016) and with a thinning level of  $10^{-6}$ . The energy and arrival direction reconstructed by KASCADE-Grande are used as input for one proton- and one iron-initiated shower. From these simulations the three components of the electric field vector are provided and after applying a rectangular filter from 43 MHz to 74 MHz the maximum field strength and pulse arrival time in each component are calculated. These values are used for the comparison with data mainly via the lateral distribution. Only within this work a detector description was developed allowing a more detailed comparison of data and simulations with a complete end-to-end simulation including all detector effects.

With the energy and arrival direction as input to the simulations still high shower-to-shower fluctuations are present. In principle a selection of the most proper shower by the shower maximum would be the best way. But neither LOPES nor KASCADE provide a measurement of this quantity. However KASCADE-Grande provides the number of measured muons which is used to select a shower as close as possible to the true mea-

sured shower. Therefore a couple of different showers were simulated for each event and for the one with the best fitting muon number the radio emission was simulated. This needs to be considered for comparison of data and simulation since still the true and the simulated shower maximum are not necessarily compatible. The amplitude of the radio emission is mainly determined by the energy, while the slope mainly depends on the shower maximum. We expect to reproduce the amplitude for single events which means a per-event comparison of the amplitude is suitable while parameters sensitive to the shower maximum, e.g. the slope, are only reproduced on a statistical level.



# 4

## Detector simulation

*In the scope of this work, parts of the analysis presented in this chapter have already been published as a contribution to the following papers:*

- Apel, W. D. et al. (LOPES-Collaboration), *Improved absolute calibration of LOPES measurements and its impact on the comparison with REAS 3.11 and CoREAS simulations*, *Astroparticle Physics*, 2016 (Apel et al., 2016)
- Schröder, F. G., Link, K. et al. (LOPES-Collaboration), *New results of the digital radio interferometer LOPES*, *Proceedings, ICRC 2015* (Schröder et al., 2016)
- Link, K. et al. (LOPES-Collaboration), *Comparison of LOPES data and CoREAS simulations using a full detector simulation*, *Proceedings, ICRC 2013* (Link et al., 2013)
- Link, K. et al. (LOPES-Collaboration), *Improved Radio Data Analysis with LOPES*, *Proceedings, ICRC 2011*, (Link et al., 2011)

---

The signal recorded by any experiment is affected by the used hardware. For a comparison of this signal with simulations or other experiments it is necessary to know the influence of the detector and to correct for it. This can either be done by unfolding the detector characteristics from the measured data, like it is done in the LOPES standard analysis pipeline, or by folding in the detector characteristics to the simulations. For the LOPES experiment such a detector simulation was prepared earlier to apply the LOPES detector response to REAS simulations (Ludwig and Huege, 2011) but it was never used and proven to be correct. Therefore it was unknown how the detector response influences the simulated signal and the reconstructed parameters. This was one possible explanation for the observed discrepancy in the amplitude between data and CoREAS simulations.

In the scope of this work the detector simulation was improved and extended, further

developed to handle also CoREAS simulations (Huege et al., 2013) and included into the standard analysis. Using such a detector simulation has several advantages:

- So far data and simulations were treated in different ways for a comparison. The simulated event which did not include noise was bandpass filtered to the LOPES effective bandwidth of 43-74MHz and then the maximum peak amplitude and peak time was calculated. Such a direct calculation is not possible for the measurements: First the electric field component is reconstructed using the simplification explained in section 3.3. Then the real peak from the air shower needs to be identified since noise can induce additional peaks. The peak time is therefore calculated from the CC-beam and with this time information the maximum of the closest peak is determined. Then for both, data and simulation a lateral distribution is fitted and compared to each other. Using a detector simulation it is possible to perform the same procedure as on data also on simulated events, even including noise. This allows a comparison of data and simulations based on a lateral distribution obtained in the same way.
- The optional inclusion of measured noise helps to understand, how noise influences the reconstructed parameters. A noise study was already performed earlier but this was not based on simulated air shower pulses but on test pulses of different shape (Schröder et al., 2012). From this noise study a noise correction was derived which is applied in the standard reconstruction. With the detector simulation this noise correction can be validated.
- Furthermore the usage of the standard pipeline with simulations directly provides an interferometric analysis for the simulations, which was never done before. In addition to a comparison based on the lateral distribution a comparison based on the CC-beam height and on the cone angle  $\rho_{CC}$  obtained during the beamforming is possible. Up to now the cone angle for simulations was obtained by a fit to the lateral time distribution which was not done for data. Using the detector simulations a common determination of the cone angle for data and simulations is possible.
- Of special interest is also the reconstruction of the electric field components. For LOPES only one polarization is measured and therefore a correct reconstruction of the electric field vector is not possible but only a simplified reconstruction, see section 3.3. For simulations the true amplitudes are directly given. For a comparison with data they are just bandpass filtered and are referred to as pure simulations. Comparing these pure simulations with those that undergo the detector simulation and the standard reconstruction, the end-to-end simulations, allows to quantify the influence of the simplified reconstruction. So far it was unclear whether the simplified reconstruction is valid at all.

In the following sections the single steps of the detector simulation and how they are implemented in the software *reas2event* are described. In principle the impact of each component of the detector on the signal is calculated in the same order as it happens in the experiment. Starting with the simulated signal first the antenna itself is considered to calculate the signal at the footpoint of the antenna. Then the influence of the analogue electronics is simulated up to the input of the ADC (analogue to digital

converter). For simulating the ADC the conversion to a digital trace with the same properties as in the experiment is performed. Finally a binary file is written using the same structure as for the measured events.

In the last part of this chapter the detector simulation is used to investigate the impact of noise and the simplified reconstruction of the electric field components on different parameters calculated in the standard analysis pipeline.

## 4.1 Structure of *reas2event*

In this part the individual steps of the detector simulation are explained and the impact of each step is shown for one event. The chosen event was simulated for an azimuth angle of  $16^\circ$  and a zenith angle of  $15^\circ$  for an iron primary particle with an energy of  $1.3 \times 10^{17}$  eV. This event was measured by the LOPES Dual setup and as example two out of the 30 antennas are shown, one east-west and one north-south aligned.

### 4.1.1 Requirements

For the full detector simulation done in *reas2event* a REAS or CoREAS simulation is needed as input. The output of these simulation codes is one file for each antenna containing the time series of the vectorial electric field at the antenna position, given by its three components  $E_{EW}$ ,  $E_{NS}$  and  $E_{VE}$ . For REAS2 simulations the sampling of the time series was constant and the same for all antennas. For REAS3 and CoREAS simulations this is not true anymore. Therefore the time series needs to be resampled for REAS3 and CoREAS simulations before using *reas2event*. To this end, a new version of the C++ code *reasplot* is developed.

### 4.1.2 Upsampling of the raw simulations

The original version of *reasplot* is distributed with the REAS code and is originally used for plotting REAS simulations. In the scope of this work the code was improved to allow for any desired sampling. For the analysis done in this work a sampling rate of 0.1 ns is chosen to minimize the influence of interpolation in the downsampling done in *reas2event*, see also figure 4.1: Since the LOPES detector is working with a sampling rate of 12.5 ns the simulated signal also will be downsampled to 12.5 ns. The zero time  $t_0 = 0$  is defined as the arrival time of the particle front. Due to different sampling rates the time steps are different for different antennas. The absolute starting time of the simulated traces is therefore also not necessarily the same for all antennas. In the LOPES event files not the time and the signal height is saved but just the height and a starting time. Therefore a linear interpolation is done to get the value between two time bins. For a high sampling rate the influence of this interpolation is minimized. In figure 4.2 the upsampled and original east-west component of the electric field is shown. The up-sampling is done by adding zeros in the frequency domain. Since the simulations fulfil the Nyquist sampling criteria the complete information is available and an up-sampling reproduces the exact values. The traces of the upsampled simulations can then be used as input for *reas2event*.

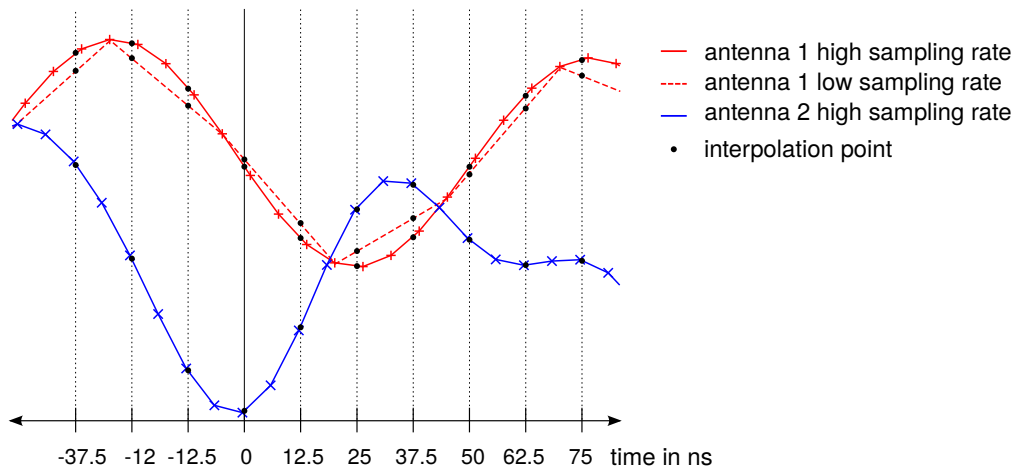


**Figure 4.1:** Illustration of the applied interpolation of the upsampled data: The solid and dashed red lines show how the upsampling rate influences the accuracy of the interpolation. The solid blue and solid red lines show that even with the same high sampling rate an interpolation is necessary since the absolute time values differ for different antennas. The black points indicate the interpolation done to achieve the LOPES sampling rate of 12.5 ns.

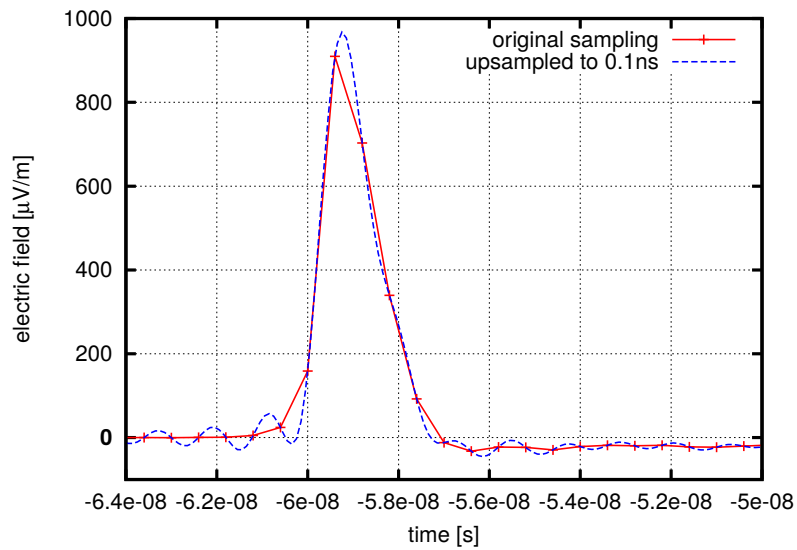


**Figure 4.2:** Original and upsampled simulated east-west component of the electric field. The simulations are done with CoREAS and the upsampling with *reasplot*

### 4.1.3 Reading simulations

The first step of *reas2event* is to read in information about the simulated shower, e.g. the direction. Then the time stamps and the corresponding electric field vectors for each antenna position are imported from the files created with *reasplot*. Figure 4.3 shows all three components of the electric field vector for the example event.

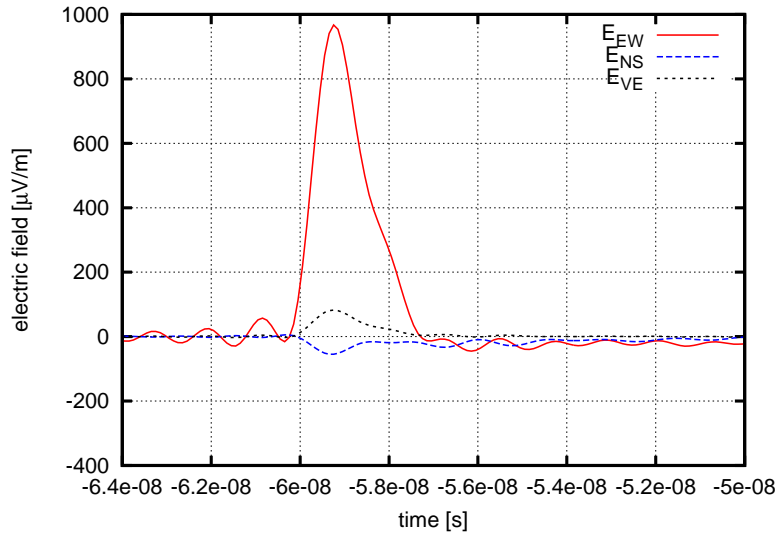


Figure 4.3: Components of the electric field vector in the Cartesian coordinate system as imported by *reas2event*.

#### 4.1.4 Calculate signal at antenna footprint

To get the voltage  $V$  induced at the footprint of each antenna the signal has to be calculated considering the gain of the respective antenna. The antenna characteristics are described by the complex gain  $G^*$  which has been simulated (Arts, 2002) and is provided in the *CalTables* of the LOPES software. The amplitude of the gain describes the spatial behaviour of the antenna and the phase counts for effects like group delay or dispersion. In the scope of this work the gain pattern of the antenna was revised, details are explained in section 5.1. For each antenna the amplitude and phase of the gain vector is given in shower coordinates depending on frequency  $\nu$  and arrival direction expressed by the azimuth angle  $\varphi$  and zenith angle  $\theta$ . The time series data of the electric field components are rotated into the shower coordinate system, which is perpendicular to the shower axis, see figure 3.13 in section 3.3, using the following rotation:

$$\begin{pmatrix} E_\varphi \\ E_\theta \end{pmatrix} = \begin{pmatrix} \cos \theta \sin \varphi & -\cos \theta \cos \varphi & 0 \\ -\cos \theta \cos \varphi & -\cos \theta \sin \varphi & -\sin \theta \end{pmatrix} \cdot \begin{pmatrix} E_{NS} \\ E_{EW} \\ E_{VE} \end{pmatrix} \quad (4.1)$$

Then the time traces are transformed to the frequency domain using a fast Fourier transformation resulting in a complex frequency spectrum. The rotation to shower coordinates has the advantage that the three-dimensional problem reduces to two dimensions since no radio emission is expected along the shower axis. The three-dimensional electric field expressed by  $E_{EW}$ ,  $E_{NS}$  and  $E_{VE}$  reduces to a two-dimensional electric field expressed by  $E_\theta$  and  $E_\varphi$ . The time series in the shower system is shown in figure 4.4.

The voltage at the footprint of each antenna is then calculated from the complex electric field components  $E_\theta^*$  and  $E_\varphi^*$  in the frequency domain using the following equation.

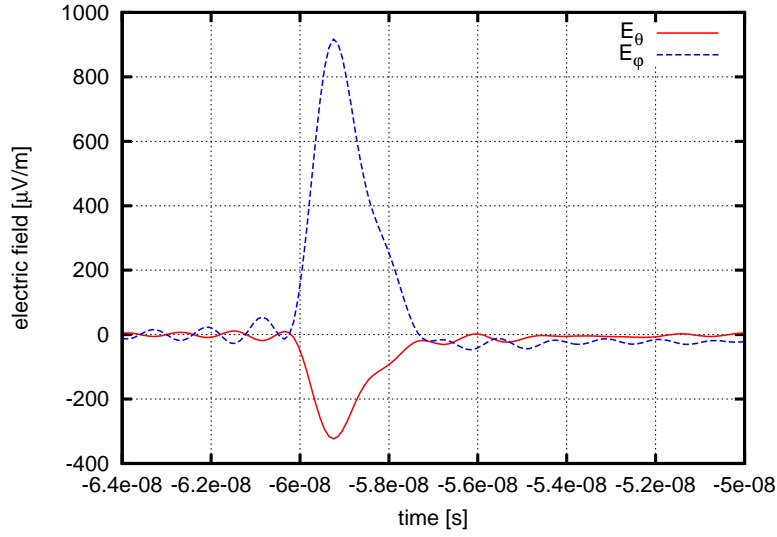


Figure 4.4: Components of the electric field vector rotated to the shower coordinate system.

$$\begin{aligned}
 V_{\text{ant}} &= \vec{E}^* \cdot \vec{H}^* = E_{\varphi}^* \cdot H_{\varphi,\text{ant}}^* + E_{\theta}^* \cdot H_{\theta,\text{ant}}^* \\
 &= |E_{\varphi}| \cdot e^{i\Phi_E} \cdot |H_{\varphi,\text{ant}}| \cdot e^{i\Phi_{H,\text{ant}}} + |E_{\theta}| \cdot e^{i\Theta_E} \cdot |H_{\theta,\text{ant}}| \cdot e^{i\Theta_{H,\text{ant}}} \\
 &= \sqrt{\frac{c}{4\pi\mu_0\nu^2}} \cdot \left( |E_{\varphi}| \cdot \sqrt{|G_{\varphi,\text{ant}}|} \cdot e^{i(\Phi_{G,\text{ant}}+\Phi_E)} + |E_{\theta}| \cdot \sqrt{|G_{\theta,\text{ant}}|} \cdot e^{i(\Theta_{G,\text{ant}}+\Theta_E)} \right)
 \end{aligned} \tag{4.2}$$

with

- ant → alignment of antenna
- $V_{\text{ant}}$  → Voltage at footpoint for specific antenna
- $\varphi$  → azimuth angle of arrival direction
- $\theta$  → zenith angle of arrival direction
- $\vec{E}^*$  → electric field vector
- $|E_{\varphi}| \cdot e^{i\Phi_E}$  → Amplitude and phase of the electric field in  $\varphi$  – direction
- $|E_{\theta}| \cdot e^{i\Theta_E}$  → Amplitude and phase of the electric field in  $\theta$  – direction
- $\vec{H}^*$  → effective antenna height vector
- $|H_{\varphi}| \cdot e^{i\Phi_H}$  → Amplitude and phase of the antenna height in  $\varphi$  – direction
- $|H_{\theta}| \cdot e^{i\Theta_H}$  → Amplitude and phase of the antenna height in  $\theta$  – direction
- $|G_{\varphi,\text{ant}}| \cdot e^{i\Phi_{G,\text{ant}}}$  → Amplitude and phase of the antenna gain in  $\varphi$  – direction
- $|G_{\theta,\text{ant}}| \cdot e^{i\Theta_{G,\text{ant}}}$  → Amplitude and phase of the antenna gain in  $\theta$  – direction

Here the simulated phases are considered while in the simplified reconstruction of the standard pipeline the phases are neglected. Figure 4.5 shows the signal at the antenna footpoint calculated for both, an east-west and north-south aligned antenna as induced by the electric field shown in figure 4.3.

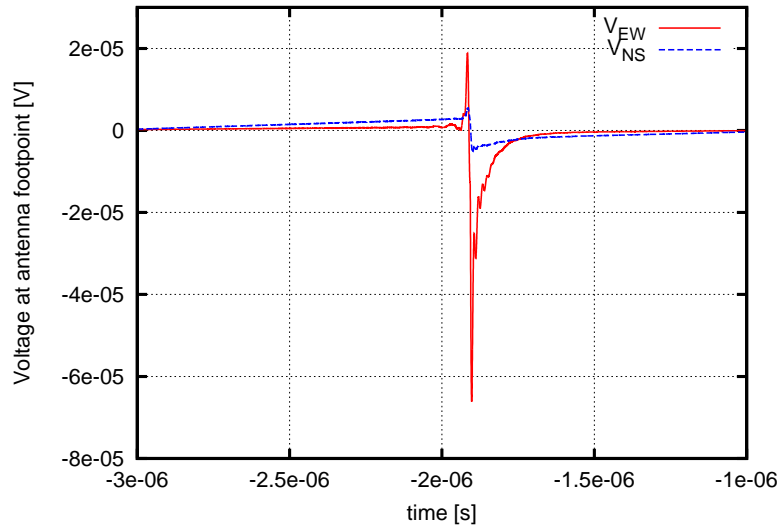


Figure 4.5: Voltage at the footprint of the antenna calculated using the complex gain of an east-west and north-south aligned antenna, respectively.

#### 4.1.5 Calculate signal at ADC

In the next step the electronic chain is considered. This includes the filter effects, like attenuation and dispersion, and time delays due to e.g. different cable lengths. These effects have been directly measured for the filters and the cable delay. The influence of the antenna itself and any other electronics was measured using an external reference antenna performing a full signal chain calibration. For details on this absolute amplitude calibration see chapter 5 and Nehls et al. (2008). After applying these instrumental effects the voltages at the ADC inputs are derived as shown in figure 4.6. As a last step the influence of the ADC itself needs to be simulated. LOPES uses a 12-bit ADC with a maximum input voltage of  $\pm 1\text{V}$  and with 80 MHz sampling. From the time range of all antennas the common range is calculated and an initial time axis with 12.5 ns sampling is defined. Then the amplitude at each time bin is calculated for each antenna using a linear interpolation, like illustrated in figure 4.1. The obtained time traces are converted into ADC values by multiplying with 2048, which are the steps per volt from the ADC, and a conversion to an integer value. This directly takes into account quantisation-effects. The obtained time trace is shown in figure 4.7.

#### 4.1.6 Noise treatment

For a realistic comparison of data and simulations noise needs to be included which can be optionally added during the detector simulation. Therefore a library of around 10 000 measured events without visible cosmic ray signals was generated. Events triggered by KASCADE with a reconstructed primary energy below  $10^{15}$  eV are used for that purpose since air showers with this energy induce a radio signal which is too low to be measured in the presence of such environmental noise like for LOPES. Before writing an output file the ADC trace of the noise events is added to the simulated signal of the air shower. The noise event is randomly chosen for each event considering the

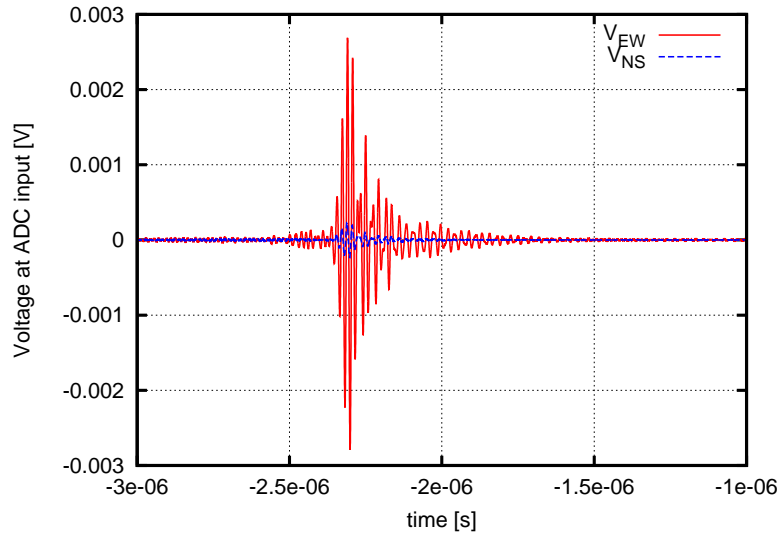


Figure 4.6: Voltage at the input of the ADC including the electric gain.

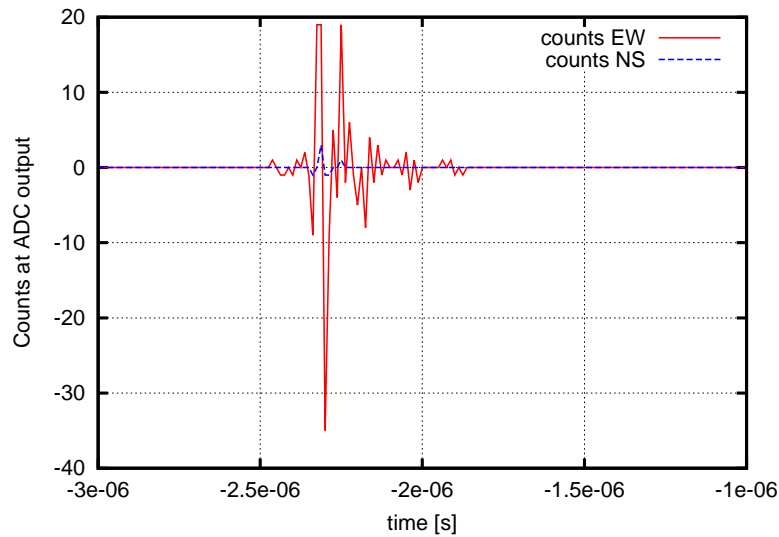


Figure 4.7: Resampled and discretized trace at the output of the ADC. Before writing the event file the time axis is adjusted.

actual LOPES antenna setup. The optional adding of noise allows to study its influence on reconstruction parameters like the CC-beam or the lateral distribution. This can be used to either verify or calculate the uncertainty for these parameters as shown in section 4.2. The example event including noise is shown in figure 4.8. The pulse of the air shower is not visible since it is below noise level. Only after filtering of the narrowband RFI (radio frequency interference) the pulse becomes visible.

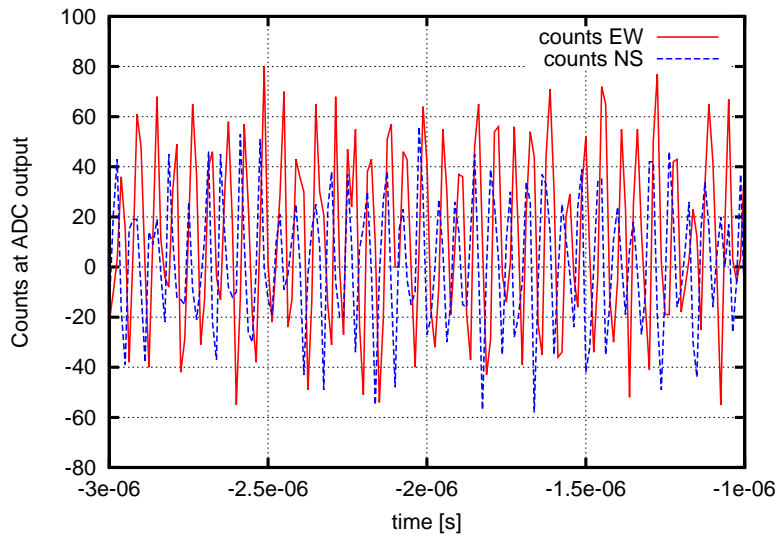


Figure 4.8: ADC counts of a simulated signal with noise measured by the LOPES experiment. The radio pulse of the air shower is below the noise level.

#### 4.1.7 Write LOPES .event file

The last step is to write a binary .event file which does not only has the same structure as the regularly measured LOPES files but it is an event as close as possible to a real measured one especially if measured noise is added. The structure is given in figure 4.9. In these event files not the complete time axis is stored but only the recorded counts for 65536 samples. On average the air shower signal at the LOPES antennas is recorded  $1.85 \mu\text{s}$  before the trigger from the KASCADE-Grande experiment is released which defines zero-time. With the presync in the header file the number of samples before the trigger time is defined. This value needs to be defined for the simulations. This is done by calculating the mean time of the simulated air shower pulse in all antennas which is then transformed to a presync value fitting to an arrival time of the pulse also at  $-1.85 \mu\text{s}$ . The generated event file has the same properties and information as the regular data files and can be used in the standard analysis pipeline.

## 4.2 Influence of noise on reconstruction parameters

With the detector simulation a study on the influence of noise on reconstructed radio emission parameters is possible. For this study a set of realistic simulations is used, corresponding to the selected LOPES events triggered by KASCADE, see section 3.5. For all events both an iron- and a proton-initiated shower is simulated resulting in 782 events in total. These simulated events undergo the detector simulation and standard analysis pipeline once including noise and once without noise. Afterwards the standard selection criteria are applied resulting in  $\sim 560$  events for the east-west antennas and  $\sim 120$  events for the north-south antennas. A comparison of the two resulting simulation sets shows how noise can affect the radio emission quantities and their uncertainty. One aspect should be kept in mind: The simulated events used here are selected to have a high signal to noise ratio. Therefore it is expected that the influence of noise is not that

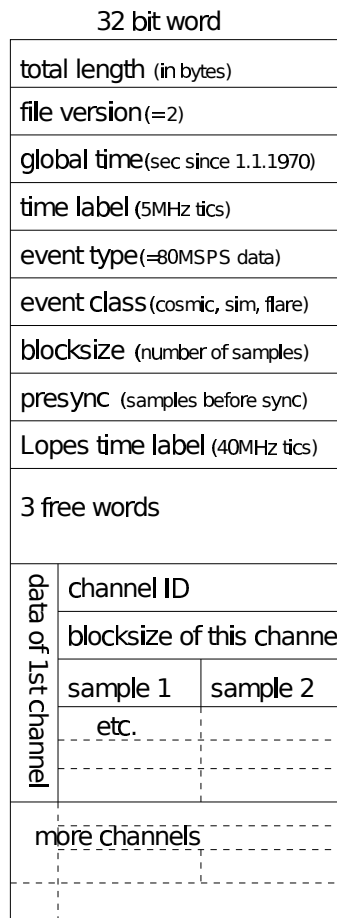
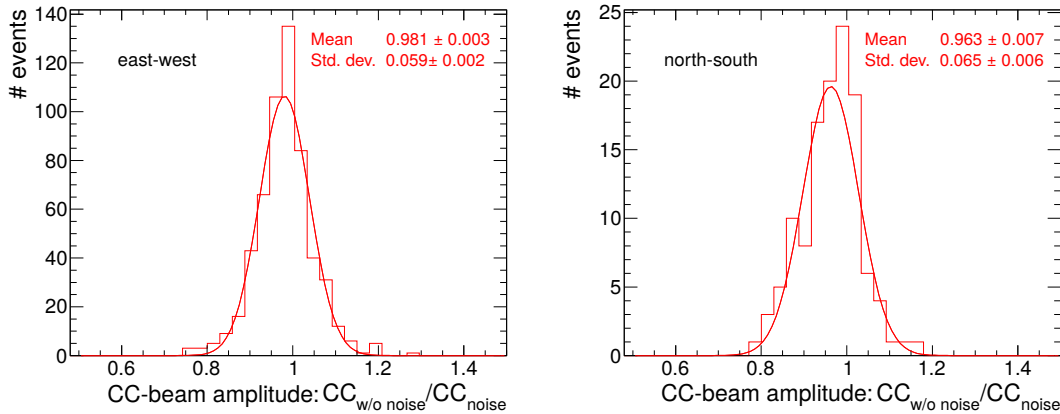


Figure 4.9: Structure of the binary LOPES event file (Horneffer, 2006).

important. To be independent from such a selection bias a high number of simulated events including hardly detectable events needs to be analysed which is not done here. For the amplitude of single antennas a noise correction is already implemented in the standard analysis pipeline (see section 3.2 and Schröder et al. (2012)). This noise correction is not considered for the simulations without noise. If the noise correction is working properly only small remaining effects are expected on all properties based on single antennas. These are all quantities derived from the lateral distribution while all quantities using the cross-correlation beam are not influenced by the noise correction. With the detector simulation it is possible to check if the applied noise correction is valid and sufficient and how noise influences the other parameters.

### CC-beam amplitude

The CC-beam amplitude obtained for simulations without noise is compared to the CC-beam amplitude obtained for simulations including noise. The ratio of both is shown in figure 4.10.



**Figure 4.10:** Ratio of the CC-beam amplitude with noise  $CC_{noise}$  and without noise  $CC_{w/o\ noise}$  obtained with the standard analysis pipeline for CoREAS simulated events, on the left for the east-west antennas and on the right for the north-south antennas.

The fitted Gaussian function has a mean of 0.981 and 0.963 and a standard deviation of 0.059 and 0.065 for the east-west and north-south antenna, respectively. In consequence of its construction a determination of the CC-beam uncertainty was not done before. From the standard deviation of the ratio distribution an estimate for the statistical uncertainty on the height of the CC-beam is possible, which is 6% for the east-west signal and 7% for the north-south signal for high quality events. Still this result needs to be handled with care since the impact of noise for events with small signal to noise ratio is expected to be much higher. Especially since an analysis based on CC-beam amplitudes is mainly interesting for low signal to noise ratio events. For a determination of the influence of noise on such events a different set of simulations is necessary.

### Cone angle of the wavefront

The wavefront was found to be of a hyperbolic shape (Apel et al., 2014b) and the most interesting parameter is the opening angle  $\rho$  of the asymptotic cone since this provides information on the depth of the shower maximum. The cone angle can be determined in two different ways. First during the interferometric reconstruction and second from a fit to the lateral time distribution measured in the individual antennas.

In previous studies (Apel et al., 2014b; Schröder, 2011) for simulations the fit to the lateral time distribution was used while for data the cone angle was derived from the interferometric reconstruction. With the newly developed detector simulation the interferometric reconstruction of the standard pipeline can be used also for simulations and for the first time the cone angle can be derived in the same way as for data also for simulations. In the following the influence of noise is discussed first for the interferometric reconstruction and then for the lateral time distribution.

$\rho_{CC}$  reconstructed via beamforming

For the reconstruction of the cone angle  $\rho_{CC}$  with the interferometric analysis, no statistical uncertainty is provided. But an estimation of this statistical uncertainty is now possible using the detector simulation and can be determined from the absolute deviation of the cone angle derived with and without noise. In figure 4.11 (left) it is visible that the mean difference is almost zero while the standard deviation is  $0.15^\circ$  and  $0.16^\circ$  for east-west and north-south antennas, respectively. These values are used as an estimate for the statistical uncertainty on the cone angle which on average amounts to about 12 %, see figure 4.11 on the right.

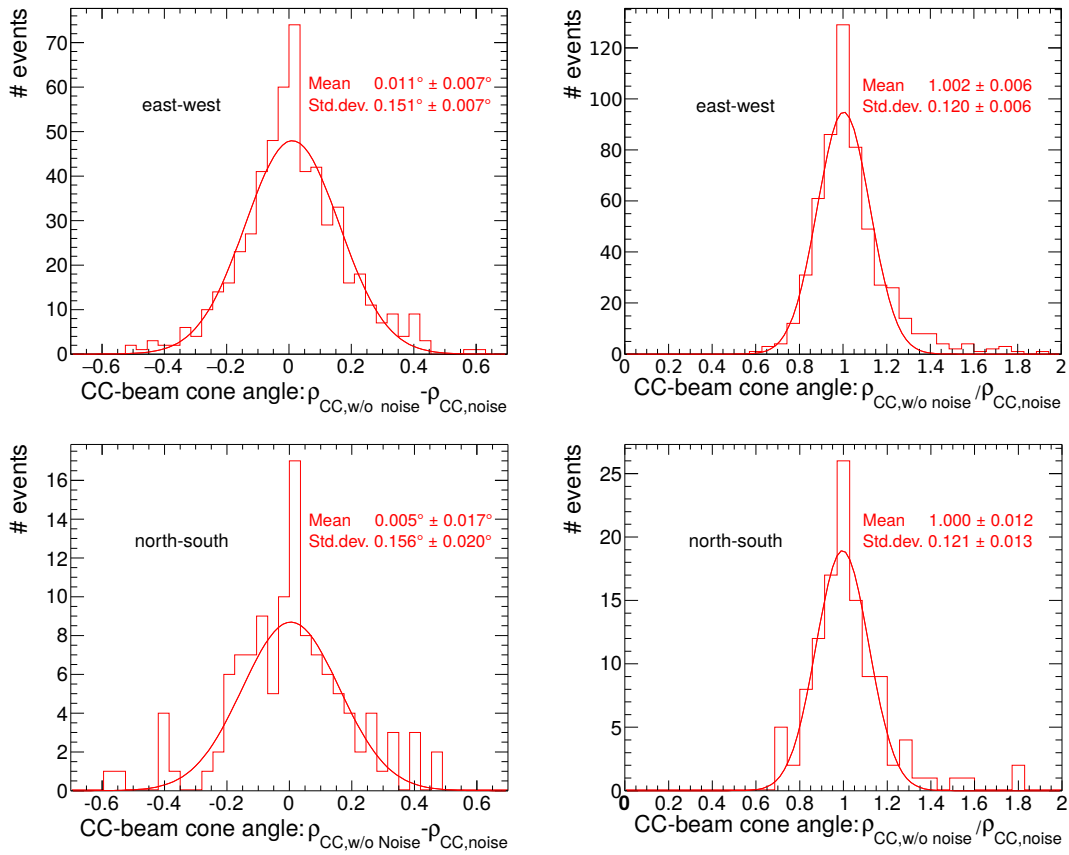


Figure 4.11: Absolute (left) and relative (right) difference of the cone angle with noise  $\rho_{CC,noise}$  and without noise  $\rho_{CC,w/o noise}$  obtained by the interferometric analysis for CoREAS simulated events, in the upper row the cone angle is calculated using the east-west antennas and in the lower row the north-south antennas.

### $\rho$ reconstructed from lateral time distribution

The lateral time distribution was formerly calculated for data in slightly different way as for simulations. The differences between both lateral time distributions is discussed in section 4.5. The main difference is the determination of the zero-time. With the detector simulation it is possible to obtain a lateral time distribution for simulations in the same way as for data, with the zero-time obtained within the standard reconstruction, see section 3.2.

After the determination of the lateral time distribution from the standard pipeline a fit is performed using the hyperbolic function for a fixed offset of  $-3\text{ns}$ , see formula 3.2. The mean deviation between the cone angle reconstructed for events including noise and events without noise is only 2% using east-west antennas and 15% using north-south antennas, see figure 4.12, left. The bigger impact on the north-south signal might be due to a smaller number of events and less numbers of antennas: For this analysis events from the LOPES 30 and the LOPES Dual setup are used, this means that the east-west events are partly measured by 30 and partly by 15 antennas while all the north-south events are only measured by 15 antennas.

The influence of noise on the statistical uncertainty derived from the fit of the lateral time distribution is shown in figure 4.12, right. A mean statistical uncertainty for the cone angle  $\rho$  is derived in the order of 60% for simulations with and between 26-30% for simulations without noise. The statistical uncertainties for the simulations without noise are only due to the definition of the zero-time and from a not rotational-symmetric lateral time distribution. In Apel et al. (2014b) the uncertainty from the asymmetry is calculated to be less than 4.6%. Quadratically subtracting this from the total uncertainty for events without noise gives the uncertainty caused by the definition of the zero-time which is  $\sim 25.6\%$  for the east-west antennas and  $\sim 30.7\%$  for the north-south antennas. Both uncertainties, the one caused by the asymmetry and the one caused by the zero-time, are expected to be highly correlated for events with and without noise. This explains why the standard deviation of the ratio of events with and without noise is only 36% for east-west and 31% for north-south antennas which is less than the quadratic sum of the single uncertainties, see figure 4.12.

Comparing the influence of noise on the two different ways of calculating the cone angle shows, that noise hardly affects the cone angle derived by the beamforming method, but strongly influences the cone angle derived from the lateral time distribution. This means that the cone angle from the lateral distribution derived for measurements is also strongly influenced by noise. This is the main reason why the beamforming method should be preferred for the measurements.

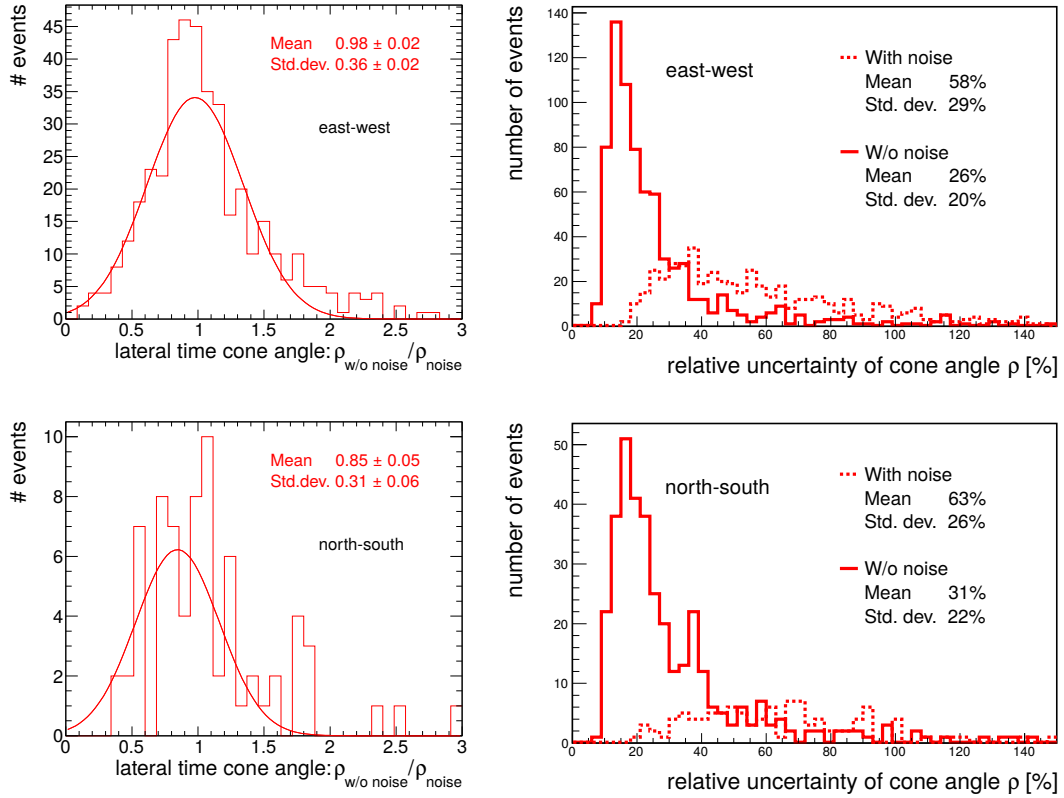


Figure 4.12: Left: Ratio of the cone angle with noise  $\rho_{noise}$  and without noise  $\rho_{w/o\ noise}$  obtained by a fit of the lateral time distribution for CoREAS-simulated events. Right: Statistical uncertainty from the fit of the lateral time distribution for CoREAS-simulated events with and without noise. Upper row for east-west antennas, lower row for north-south antennas.

### Lateral distribution

In this section the influence of noise and the application of the noise correction is discussed. The fit on the lateral distribution using an exponential function, as given in formula 3.4, is applied during the standard reconstruction pipeline, with the noise correction for those events with added noise and without noise correction for the others.

The impact of noise on the amplitude parameter  $\epsilon_{100}$  is shown in figure 4.13. The mean value of the ratio is 0.99 and 0.98 for the east-west antennas and for the north-south antennas, respectively, with a standard deviation of 0.07 for both antenna alignments. The statistical uncertainty of the amplitude  $\epsilon_{100}$  is 8% for east-west and 10.6% for north-south events including noise and 2.5% for east-west and 5.2% for north-south events without noise, see figure 4.13 on the right. The increase of the statistical uncertainty for the inclusion of noise is in the same order as the standard deviation of the ratio of events without noise and with noise. This and the mean values of almost one confirm that the noise correction applied in the standard analysis pipeline indeed successfully corrects for amplitude biases.

For a comparison of the slope parameter  $\eta$  not the relative but the absolute changes are investigated: Since the slope can get close to zero the relative differences can get really

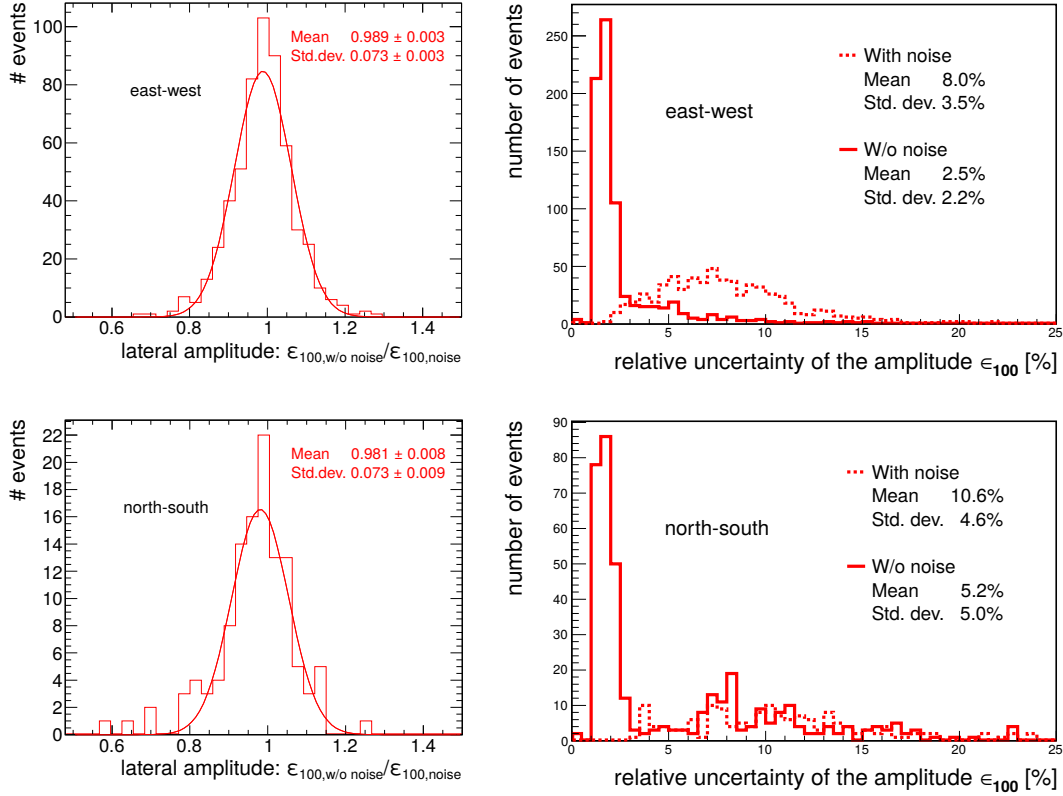


**Figure 4.13:** Left: Ratio of the fitted amplitude parameter with noise  $\epsilon_{100,noise}$  and without noise  $\epsilon_{100,w/o\ noise}$  for CoREAS simulated events. Right: Statistical uncertainty from the fit of the lateral distribution for CoREAS-simulated events with and without noise. The upper row shows the amplitudes calculated for the east-west antennas and the lower row for the north-south antennas.

high although the slope is still similar. Such high relative differences would dominate and therefore distort the resulting distribution. The statistical uncertainty for the slope parameter  $\eta$  is about  $1.7\text{ km}^{-1}$  for east-west and  $2.3\text{ km}^{-1}$  for north-south events, see figure 4.14. Related to a mean value of  $\eta=4.65\text{ km}^{-1}$  for proton and iron events (see also appendix A) this is about 36% for the east-west events. From the statistical uncertainties a bigger influence of noise is expected for the north-south antennas which is not seen in the ratios. But the higher statistical uncertainties can also be explained by the smaller number of antennas. On average the noise lowers the slope parameter by  $1\text{ km}^{-1}$  for east-west and  $0.5\text{ km}^{-1}$  for north-south which corresponds to flatter lateral distributions. This could influence the reconstruction of the shower maximum and needs to be considered later, see also section 4.4. Furthermore it shows that the applied noise correction is insufficient concerning the slope of the lateral distribution. The noise correction already leads to a lower slope but the effect is too small.

The noise measured by LOPES is the main generator for statistical uncertainties on the parameters of the lateral distribution. Realistic noise raises the mean uncertainty from the fit for the amplitude parameter  $\epsilon_{100}$  from around 2.5% to 8% and 5.2% to 10.6% for east-west and north-south events, respectively, as shown in figure 4.13 on the right. For the slope parameter  $\eta$  the relative statistical uncertainty can be quite

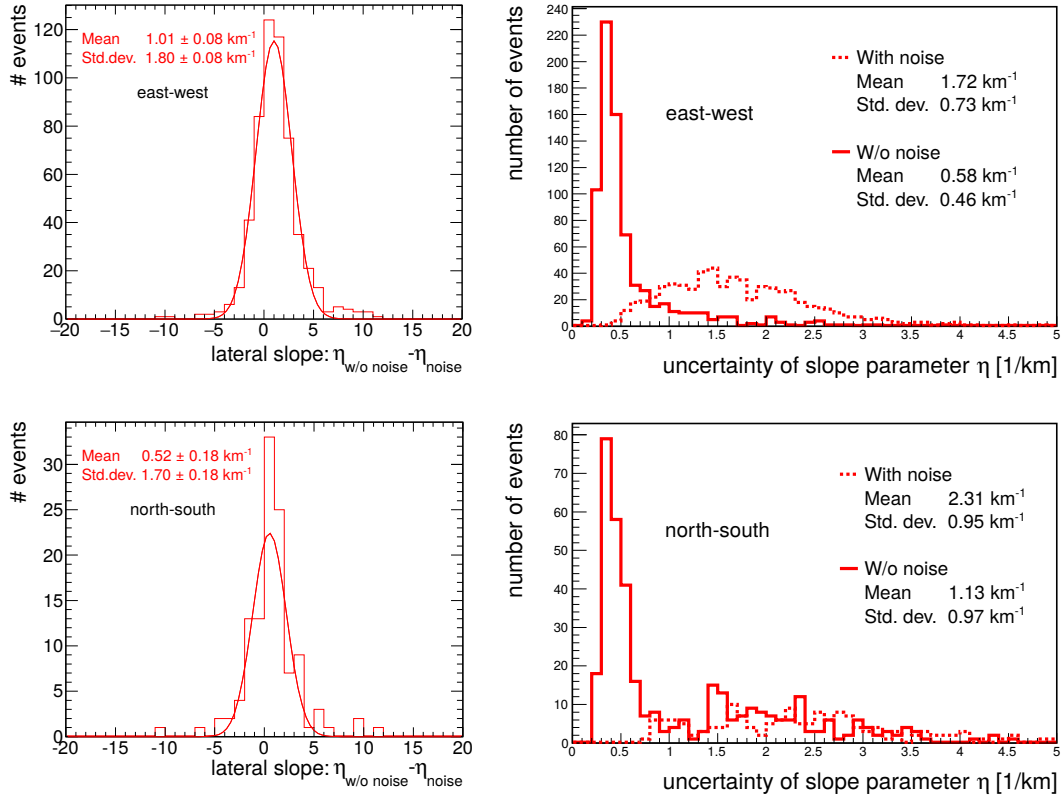


Figure 4.14: Left: Absolute deviation of fitted slope parameter with noise  $\eta_{noise}$  and without noise  $\eta_{w/o\ noise}$  for CoREAS simulated events. Right: Absolute statistical uncertainty from the fit of the lateral distribution for CoREAS-simulated events with and without noise. The upper row shows the slope calculated for the east-west antennas and the lower row for the north-south antennas.

large especially for flat events which have a slope parameter close to zero. Since these can distort the distribution the absolute uncertainties are shown. Noise increases the mean absolute uncertainty from  $0.6\text{ km}^{-1}$  to  $1.7\text{ km}^{-1}$  for east-west and from  $1.1\text{ km}^{-1}$  to  $2.3\text{ km}^{-1}$  for north-south events, see figure 4.13 right.

### 4.3 Influence of the simplified reconstruction on the electric field components

With the detailed detector simulation it is possible to check the impact of the standard analysis pipeline on the reconstruction of the electric field components. In principle all detector effects are unfolded in the standard analysis pipeline. But as explained in section 3.3 a correct reconstruction of the electric field vector is not possible for LOPES. Therefore, a simplified reconstruction is used. How this simplification affects the reconstructed signal was never studied before and could be one explanation for the observed discrepancy between LOPES data and CoREAS simulations, as discussed in sections 3.3 and 3.4. With the developed full detector simulation the influence of the simplified reconstruction can be determined using CoREAS simulations. But beside

the simplified reconstruction the quantization of the signal due to the ADC can change the amplitude of the input simulation. This cannot be corrected for in the standard analysis pipeline and is always contained in the detector simulation. It is not possible to discriminate whether the reconstructed amplitude differs from the true amplitude due to the quantization or the simplification. The simplified reconstruction always contains the influence of the quantization but in the following this is no longer explicitly mentioned.

For this study not only the simulation set described in section 3.5 is used but also a library of 144 events all with identical energy and with arrival directions distributed regularly over the whole sky. For this analysis no noise was added to the simulations to get the pure impact of the simplified reconstruction. For the comparison the pure simulations, just filtered to the LOPES bandwidth, are compared to the simulations that undergo the detector simulation and standard analysis pipeline. The pure simulations represent the true east-west and north-south components of the electric field, while the simplified components are those reconstructed by the standard analysis pipeline for an east-west and north-south aligned antenna, respectively. The influence of the simplification is expected to depend on the polarization of the signal with respect to the alignment of the antenna.

#### Amplitude reconstructed for single antennas

For the true electric field component the simulations are filtered to the LOPES bandwidth of 43-74 MHz and the maximum pulse amplitude in each antenna is calculated. The simplified electric field component is derived from the simulations that undergo the full detector simulation and the standard analysis pipeline and the signal of each antenna is determined as described in section 3.2. In a first step the influence of the simplification for the signal of a single antenna is studied. Figure 4.15 shows the ratio of the true and simplified electric field components for the event library, both for an east-west (left) and north-south (right) aligned antenna. Only two antennas are shown but all antennas have a similar behaviour. Differences for single antennas are probably due to the Askaryan effect which influences the polarization and depends on the position of the antenna relative to the shower axis.

An overall shift is visible for both components, which indicates an underestimation of the electric field due to the simplified reconstruction. The influence strongly depends on shower geometry which defines the polarization of the signal.

For this study all events of the simulation library are considered, even those with a very low signal, far below the noise level of LOPES. The largest effect of the simplified reconstruction is occurring for these very low signals. Therefore such large differences are not expected for actually measured events. For a more realistic picture a set of simulations of actually measured events is used.

The simulation set of KASCADE triggered events is used, but only considering iron primaries. Additionally a minimum signal of  $1\mu\text{V}/\text{m}/\text{MHz}$  for the example antennas is required. This leads to a total number of 238 events for the east-west antenna and 129 events for the north-south antenna. The lower number of events for the north-south antenna has two reasons: The expected signal for the north-south polarization is lower than for the east-west signal and the events were originally chosen to have a good east-west signal. Figure 4.16 shows the ratio of the electric field component for the realistic

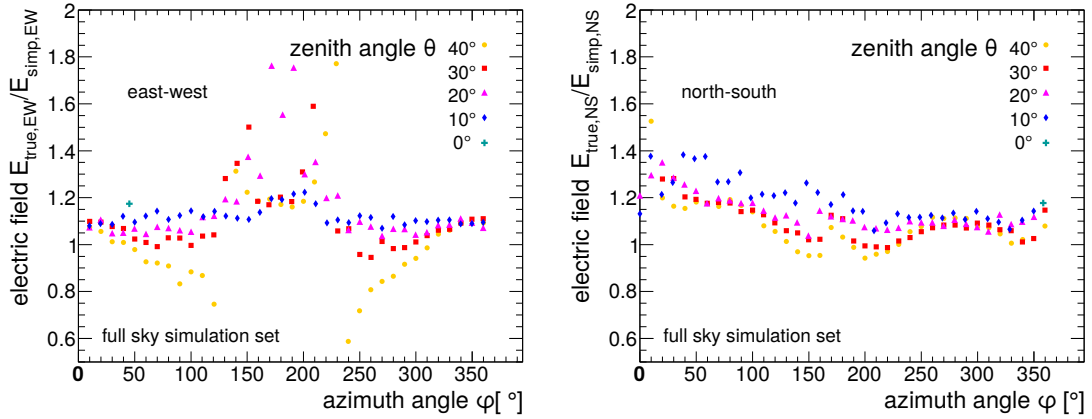


Figure 4.15: Ratio of the true  $E_{true,(EW/NS)}$  and simplified  $E_{simp,(EW/NS)}$  electric field components for the event library of the whole sky. The different colours represent different zenith angles. On the left the amplitude of an east-west aligned antenna, that is the east-west component of the electric field, is shown and on the right for a north-south aligned antenna.

angular and energy distribution.

As already for the library also for the realistic data set a systematic shift is observed for both polarizations. Yet the width of the distribution gets smaller since those arrival directions with the highest reconstruction differences are outside the sensitive region of LOPES. For a quantitative conclusion a Gaussian is fitted on the distribution of the ratio. For the east-west component a mean value  $\mu_{EW} = 1.045$  with a standard deviation of  $\sigma_{EW} = 0.058$  is found and for the north-south component  $\mu_{NS} = 1.074$  and  $\sigma_{NS} = 0.051$ . The influence of the simplified reconstruction is below the measurement uncertainty of LOPES data which is, depending on the signal to noise ratio, mainly above 10%. The histograms and the Gaussian fit are also shown in figure 4.16.

#### Amplitude of the lateral distribution

In most of the analyses not the amplitude of single antennas but the quantities corresponding to a fit on the lateral distribution are used. Therefore the influence of the simplified reconstruction on the amplitude parameter  $\epsilon_{100}$  and in the next section on the slope parameter  $\eta$  of the exponential function (see formula 3.4) is studied.  $\epsilon_{100}$  represents the amplitude of the electric field of the complete shower instead of a single antenna electric field, but the essential behaviour should be comparable. Since  $\epsilon_{100}$  relies on a fitted function only events fulfilling the criteria for a succeeded fit are used. For higher statistics the complete simulated event set, including KASCADE-Grande events, is used. Additional cuts on a successful fit are required. For the east-west aligned antennas this results in 593 events for each primary particle and for the north-south aligned antennas 229 for iron and 252 for proton primaries remain. A per-event comparison of the true and simplified  $\epsilon_{100}$  and the distribution of their ratio is shown in figure 4.17. The mean deviation is less than 2% for the east-west component and around 7% for the north south component. This difference is due to the fact, that the simplified reconstruction strongly depends on the polarization of the signal. Since  $\epsilon_{100}$  is derived from a fitting procedure the systematic shift is smaller than the one observed for the single

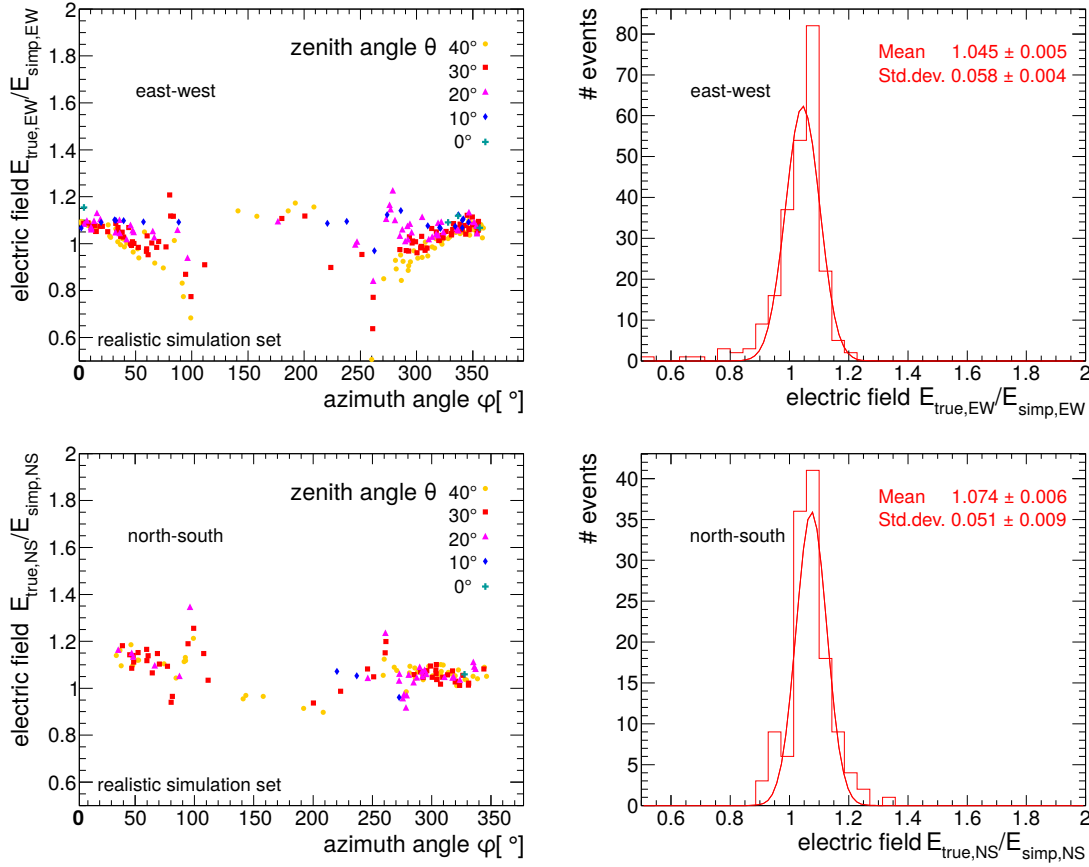


Figure 4.16: Ratio of the true  $E_{true,(EW/NS)}$  and simplified  $E_{simp,(EW/NS)}$  electric field components for a realistic set of simulations. The different colours represent different zenith angles. On the upper left the amplitude of an east-west aligned antenna is shown and on the lower left the amplitude of a north-south aligned antenna. On the right the corresponding distributions are shown.

antennas while the standard deviation is slightly higher.

For comparing the LOPES signal with other experiments the shift can be considered as additional systematic uncertainty while for future comparisons of data and simulations the simplified reconstructed electric field can be used. Former results comparing data and simulations on the basis of  $\epsilon_{100}$  can only change by a few percent which cannot resolve the observed difference between LOPES data and CoREAS simulations.

### Slope of the lateral distribution

The slope of the lateral distribution is mainly important for the reconstruction of the shower maximum. In contrast to the amplitude, the slope of data and simulation shows no discrepancies, neither for REAS nor for CoREAS.

An overall shift in the amplitude of all antennas should not influence the slope of the lateral distribution. But as mentioned earlier the change in the amplitude of the single antennas is not exactly the same for all antennas. Therefore also a change of the fitted slope  $\eta$  is possible. Figure 4.18 shows the comparison of the simplified and true  $\eta$  and the corresponding histograms of the absolute difference. For the calculation of

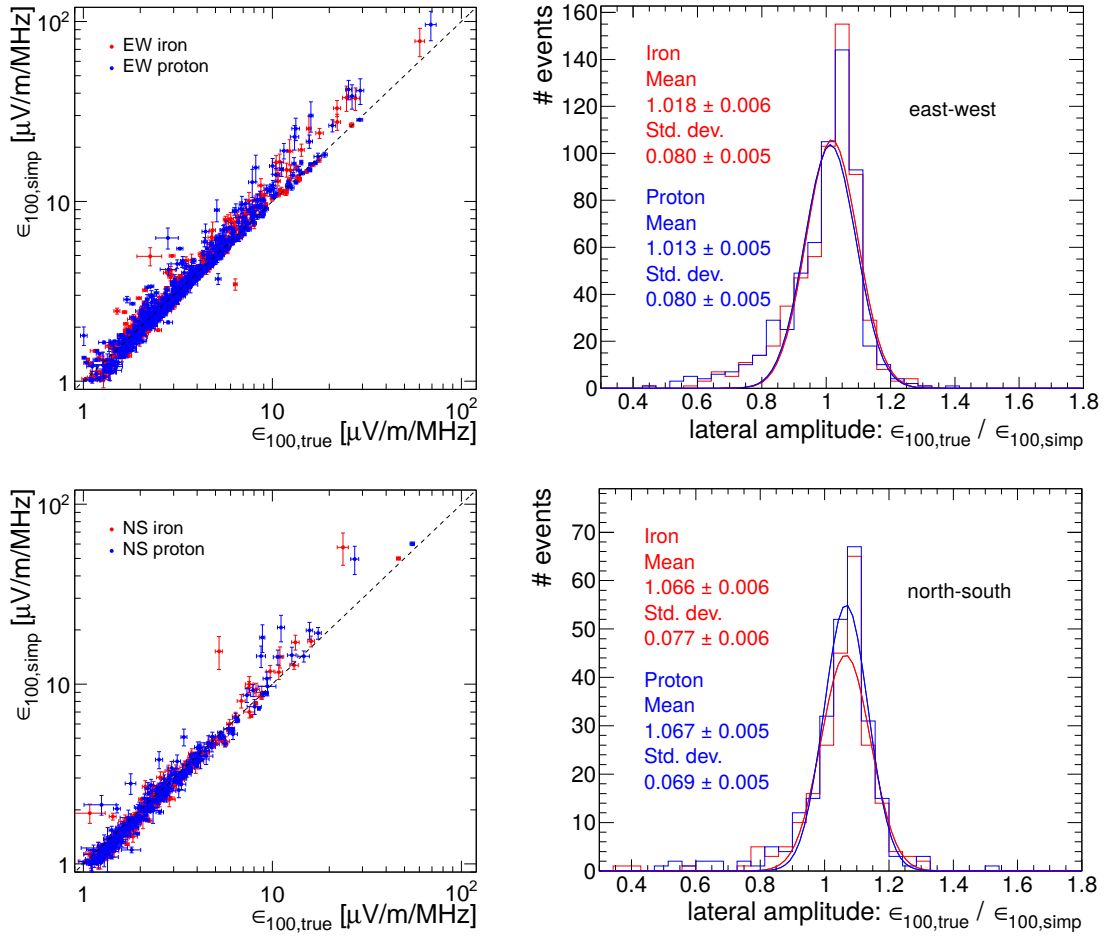


Figure 4.17: Left: Comparison of the simplified  $\epsilon_{100,simp}$  and true  $\epsilon_{100,true}$  for a realistic set of simulations including KASCADE and KASCADE-Grande data for both, iron and proton initiated showers. On the upper row for an east-west and on the lower row for a north-south aligned antenna. Right: The corresponding distributions of the ratio of the true and simplified  $\epsilon_{100}$ .

the mean and the standard deviation the outliers, not shown in the histogram either, are excluded. The simplified reconstruction overestimates the slope by around  $1\text{km}^{-1}$  which is, related to the mean values shown in the appendix A, in the order of 20% to 25%. This means that the slopes reconstructed with the LOPES standard pipeline are steeper than the true slope directly obtained by pure simulations which is of interest for the results on the depth of shower maximum. But this comparison did not include noise so far and in the former section it was shown that noise leads to flatter slopes. Further investigations combining both effects are done in the next section.

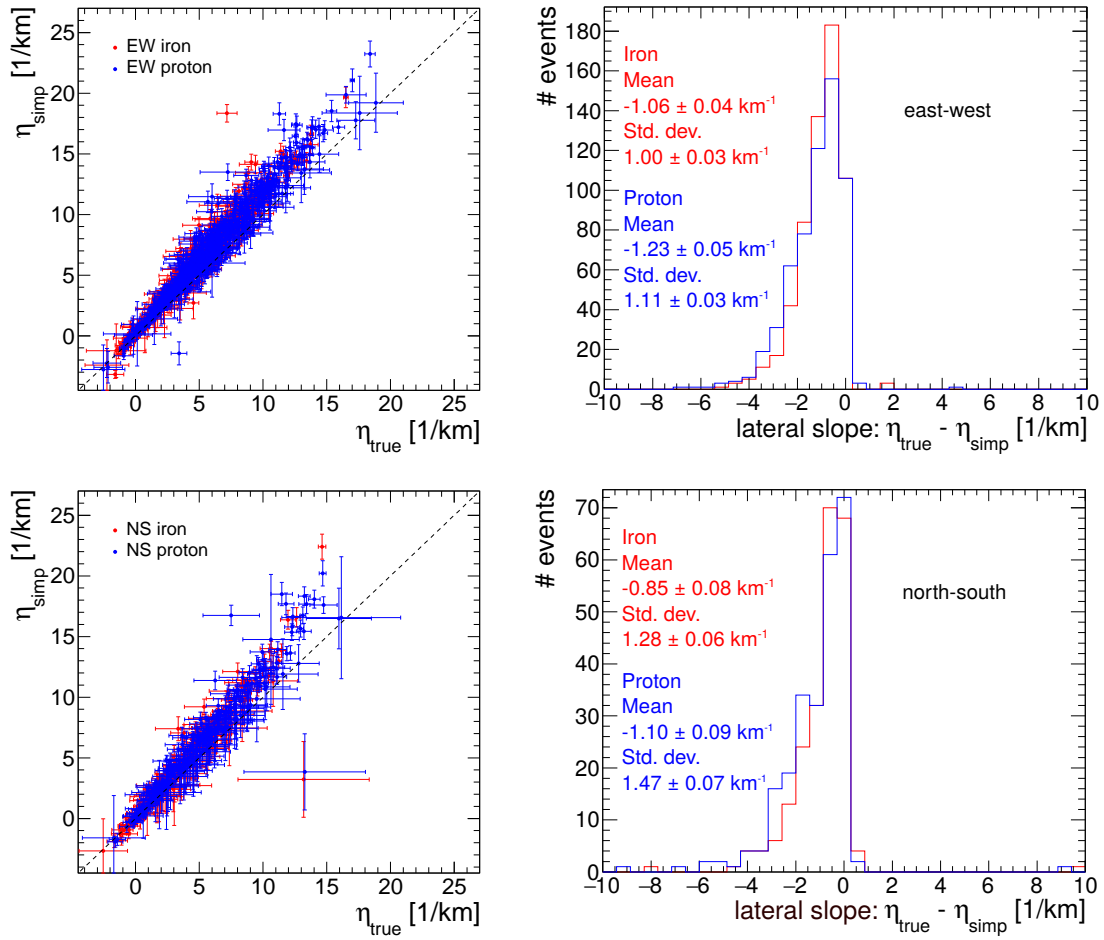


Figure 4.18: Left: Comparison of the simplified  $\eta_{simp}$  and true  $\eta_{true}$  for a realistic set of simulations including KASCADE and KASCADE-Grande data for both, iron and proton initiated showers. On the upper row for an east-west and on the lower row for a north-south aligned antenna. Right: The corresponding distributions of the difference between the true  $\eta$  and simplified  $\eta$ .

#### 4.4 Comparison of pure simulations and simulations including noise

In the sections above first the pure influence of noise was studied and afterwards the pure influence of the simplified reconstruction. In the end, for a comparison with data, both aspects must be considered. For this purpose the pure simulations from CoREAS, only using a bandpass filter, are compared to the end-to-end simulations which ran through the whole detector simulation and the standard reconstruction including noise.

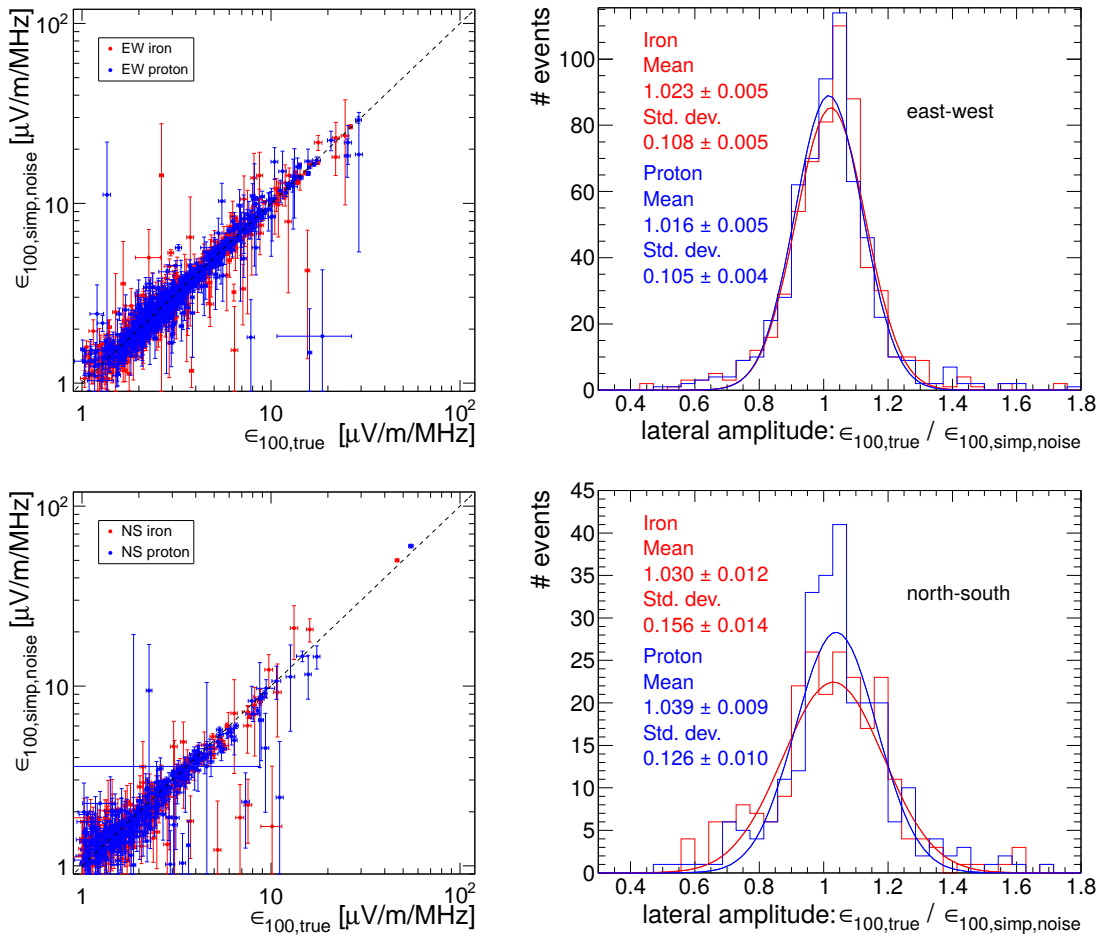


Figure 4.19: Per-event comparison (left) and ratio (right) of the true east-west and north-south amplitude parameter  $\epsilon_{100, \text{true}}$  and of the simplified reconstructed east-west and north-south amplitude parameter including noise  $\epsilon_{100, \text{simp, noise}}$  for CoREAS simulations.

For the pure simulations, which represent the true amplitude, no interferometric analysis is performed. All comparisons are therefore based on the lateral distributions. From the inclusion of noise we expect almost no influence on  $\epsilon_{100}$  and a decrease of the slope  $\eta$  in the order of  $1 \text{ km}^{-1}$  for east-west and  $0.5 \text{ km}^{-1}$  for north-south events as obtained in the above sections. From the simplified reconstruction a mean decrease of  $\epsilon_{100}$  by 1.5% for east-west and  $\sim 7\%$  for north-south is expected and a mean increase of  $\eta$  by  $1.15 \text{ km}^{-1}$  for east-west and  $\sim 1 \text{ km}^{-1}$  for north-south. So in total a small decrease of  $\epsilon_{100}$

is expected and a small increase or even a cancellation of both effects for  $\eta$ . Figure 4.19 shows a decrease of the amplitude for the simplified reconstruction in the order of 2 % for east-west and 3-4 % for north-south events which is significantly below the mean statistical uncertainty for  $\epsilon_{100}$  for simulations including noise which is 8 % and  $\sim 11$  %, respectively, see figure 4.13. The standard deviation of the ratio between the true and reconstructed amplitude is around 10 % for east-west and below 16 % for north-south events which fits to the scatter expected due to the statistical uncertainty. For the slope obtained with the east-west antennas almost a cancellation is observed, see figure 4.20. The mean change of the slope is less than  $0.2 \text{ km}^{-1}$  which is negligible compared to the statistical uncertainties of  $\eta$  for simulations including noise which is in the order of  $1.7 \text{ km}^{-1}$ , see figure 4.14. For the north-south component the shift is higher, around  $0.5\text{-}0.66 \text{ km}^{-1}$ , but also the statistical uncertainty is higher, namely  $2.3 \text{ km}^{-1}$ . Still the shift of the slope obtained for the north-south component should to be considered for future analyses. While the comparison of the pure and end-to-end simulations without noise showed an asymmetric distribution the distribution of  $\eta$  becomes symmetric for the inclusion of noise. This shows that the scatter induced by noise smears out the influence by the simplified reconstruction.

#### 4.5 Influence of reconstruction method on lateral time distribution

For the lateral time distribution the zero-time needs to be defined, which is theoretically the time when the shower front hits the ground. For simulations this is done by simulating antennas at the shower core while for measurements the zero-time is defined by the CC-beam maximum. This is the main difference for the lateral time distribution obtained within the reconstruction pipeline applied to data and obtained from pure simulations. The distance to the shower core and also the determination of the arrival time is done in the same way. The influence of the different calculations can be studied with the detector simulation. In section 4.2 it was shown that noise does not systematically change the reconstructed cone angle. From figure 4.21 a change in the cone angle is observed for the two methods of calculating the lateral time distribution. Here a comparison is done for the end-to-end simulations without noise to not introduce additional uncertainties and only for the east-west component.

The mean cone angle differs by almost  $0.5^\circ$  for the different treatments of the simulations. Looking at individual events it seems that not the observed cone angle itself differs but the zero-time seems to be incorrect leading to a shift of the cone angle. This has not been observed in the data so far but the measurements also suffer from high uncertainties, see also section 6.1. The cone angle derived from the lateral time distribution is the only property with a significant change for the end-to-end simulations and the reason for this is still unknown.

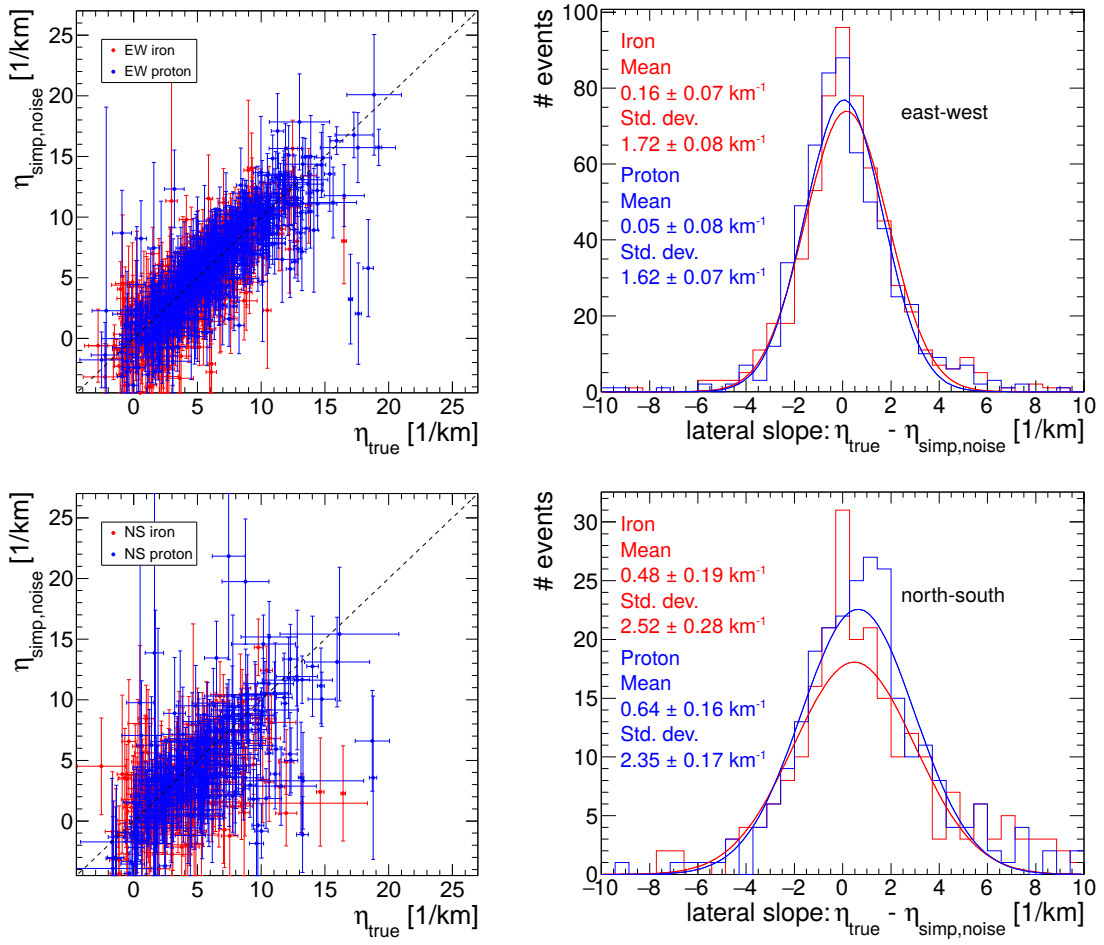


Figure 4.20: Per-event comparison (left) and ratio (right) of the true slope parameter  $\eta_{true}$  and simplified reconstructed slope parameter including noise  $\eta_{simp,noise}$  for the east-west and north-south component of CoREAS simulations.

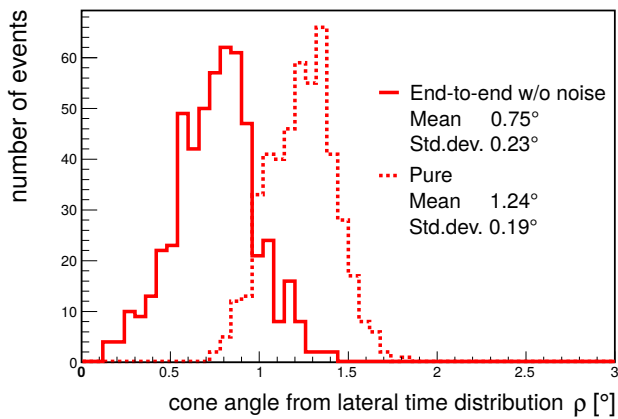


Figure 4.21: Distribution of the cone angle  $\rho$  derived from the lateral time distribution for pure simulations and simulations including the detector simulation for proton-induced air showers.

## 4.6 Conclusion

The developed detector simulation includes all detector characteristics and it is possible to add measured noise to the simulations. It is possible to produce a measured-like event file out of REAS or CoREAS simulations which can be used as input for the standard reconstruction pipeline of LOPES. The detector simulation is a powerful tool for the comparison of data and simulations and allows the validation of the standard reconstruction pipeline which was previously not possible.

Tables 4.1 and 4.2 summarize the results obtained for the comparison of the true and reconstructed signal with and without noise.

**Table 4.1:** Influence of noise on different radio emission quantities. The simplified simulations (also end-to-end simulations) are derived by applying the detector simulation and the standard LOPES pipeline to CoREAS simulations with and without noise.

		$\frac{\text{simp, w/o noise}}{\text{simp, w/ noise}}$	
		Mean	Std. dev.
CC-beam amplitude	EW	0.981	0.059
	NS	0.963	0.065
cone angle $\rho_{CC}$	EW	1.002	0.120
	NS	1.00	0.12
lateral amplitude $\epsilon_{100}$	EW	0.989	0.073
	NS	0.981	0.073
		$(\text{simp, w/o noise}) - (\text{simp, w/ noise})$	
		Mean [km <sup>-1</sup> ]	Std. dev. [km <sup>-1</sup> ]
lateral slope $\eta$	EW	1.01	1.80
	NS	0.52	1.70

The detector simulation allows directly to use the interferometric analysis provided by the reconstruction pipeline of LOPES also for simulations, and the CC-beam and cone angle  $\rho_{CC}$  are calculated for these simulations. It was possible to determine an uncertainty on these quantities induced by noise which are  $\sim 6\%$  for the amplitudes of the CC-beam and  $12\%$  for the cone angles obtained using the east-west and north-south antennas.

Furthermore it is possible to compare properties of measured and simulated events which are reconstructed and analysed in the same way. For example, so far, the cone angles of simulations were obtained by a fit to the lateral time distribution while for data they were derived within the interferometric analysis. Using the detector simulations it is possible to obtain the cone angles for simulated events in the same way as for measured events. A comparison of data and simulations is shown in chapter 6.

Without the presented investigations it was unclear how precise the reconstruction pipeline of LOPES works. It was now possible to show that the reconstructed lateral distribution including noise is compatible within uncertainties with the true lateral distribution for both parameters  $\epsilon_{100}$  and  $\eta$ . This was not necessarily expected due to

**Table 4.2:** Influence of the simplified reconstruction on different radio emission quantities. The simplified simulations (also end-to-end simulations) are derived by applying the detector simulation and the standard LOPES pipeline to CoREAS simulations with and without noise. The true simulations (also pure simulations) are directly derived from the CoREAS simulations without noise only applying a bandpass filter for the LOPES frequency range.

			<u>true</u> simp, w/o noise		<u>true</u> simp, w/ noise	
			Mean	Std. dev.	Mean	Std. dev.
lateral amplitude $\epsilon_{100}$	EW	proton	1.013	0.080	1.016	0.105
		iron	1.018	0.080	1.023	0.108
	NS	proton	1.067	0.069	1.039	0.126
		iron	1.066	0.077	1.030	0.156
			(true) – (simp, w/o noise) [km <sup>-1</sup> ]		(true) – (simp, w/ noise) [km <sup>-1</sup> ]	
			Mean	Std. dev.	Mean	Std. dev.
lateral slope $\eta$	EW	proton	-1.23	1.11	0.05	1.62
		iron	-1.06	1.00	0.16	1.72
	NS	proton	-1.10	1.47	0.64	2.35
		iron	-0.85	1.28	0.48	2.52

the simplified reconstruction applied in the standard pipeline. It is now possible to state that it is valid to use the pure simulations for comparison of data and simulation. This implies that former results obtained with such pure simulations are still valid. For the amplitude it was shown that the noise correction applied in the standard pipeline works properly and also the simplified reconstruction has no significant effect for typical LOPES events. For the slope the noise correction is insufficient but by chance this effect is cancelled out by the effect of the simplified reconstruction, at least on a statistical basis for the east-west events. For individual events, depending on geometry and signal-to-noise ratio, one or the other effect might be dominating. For any analysis based on per-event comparisons this needs to be considered. In this thesis the slope is used for a comparison of data and simulations which is anyhow based on a statistical analysis.

The results obtained with the LOPES experiment were mostly based on the east-west antennas, mainly because for these a bigger data set is available. This has two reasons, first the measurement time using east-west antennas is much longer and second the expected signal in the east-west component is higher due to the geomagnetic origin of the radio emission. In this thesis all further investigations are therefore only done for the east-west antennas.

# 5

## Absolute Amplitude Calibration

*In the scope of this work, parts of the analysis presented in this chapter have already been published as a contribution to the following papers:*

- Apel, W. D. et al. (LOPES-Collaboration), *Improved absolute calibration of LOPES measurements and its impact on the comparison with REAS 3.11 and CoREAS simulations*, *Astroparticle Physics*, 2016 (Apel et al., 2016)
- Link, K. et al. (LOPES-Collaboration), *Revised absolute amplitude calibration of the LOPES experiment*, *Proceedings of Science, ICRC 2015* (Link et al., 2016)
- Schröder, F. G., Link, K. et al. (LOPES-Collaboration), *New results of the digital radio interferometer LOPES*, *Proceedings, ICRC 2015* (Schröder et al., 2016)
- Nelles, A. et al., *Calibrating the absolute amplitude scale for air showers measured at LOFAR*, *Journal of Instrumentation*, 2015, (Nelles et al., 2015b)

---

The previous chapter showed that a correct consideration of the detector influence on the simulations cannot explain the discrepancy between data and CoREAS simulations discussed in section 3.4. The major part which defines the absolute amplitude for data is the calibration of the amplitude itself and the description of the antenna. The spatial behaviour of the antenna is described by the directional gain pattern of the antenna. This gain has been simulated by LOFAR engineers (Arts, 2002) and is only used for a relative description of the antenna depending on the incoming direction of the shower. The absolute amplitude is determined with an absolute calibration using an external reference source. With this reference source the absolute amplitude is calculated only for the zenith direction. In this chapter the simulated gain and the absolute amplitude calibration is scrutinized, which includes the procedure of the calibration and its software analysis, as well as the used reference source. Several improvements were made

whose impact on the reconstruction parameters is described in section 5.6. Additionally, a cross-calibration between LOPES, Tunka-Rex and LOFAR is presented in the last section.

## 5.1 Revision of the simulated antenna gain pattern

The gain pattern of the LOPES antennas was simulated and as output a complex gain as a function of arrival direction and frequency was provided in the shower coordinate system. In the simplified standard reconstruction of the electric field components a total gain is used only considering the amplitude and not the phase of the antenna gain. But for the calculation of the voltage at the antenna footpoint inside the detector simulation also the complex phase is considered. Including the phase and using the original gain pattern a problem arises:

The LOPES antennas are built on top of a metal pedestal. Considering this pedestal in the simulation of the gain pattern leads to a high gradient in the phase at around 58 MHz for some arrival directions as shown in figure 5.1. This leads to multiple pulses in the time domain, like in figure 5.2. But such multiple pulses were never seen in data. In addition to the high gradient in the phase the metal pedestal simulations show a resonance peak in the amplitude at 58 MHz. This effect was already studied in former analyses, see Saftoiu et al. (2012) and Nehls et al. (2008). The peak in the amplitude of the gain pattern did not properly describe the data and it was corrected for by using an interpolation of the gain amplitude at 58 MHz. To avoid the double pulses originating from the high gradient in the phase such a simple interpolation cannot be performed. It seems that the antenna simulations overestimate the influence of the pedestal. Beside the originally used simulations also simulation for a LOPES antenna without pedestal were performed. These simulations seem to describe the data more realistically. The peak in the amplitude and the jump in the phase vanishes for the simulations without pedestal, as demonstrated in figure 5.3. Using this gain pattern no double pulses appear and also the amplitude behaviour is described correctly. Therefore the originally used gain pattern including the metal pedestal was exchanged as a result of the considerations made in this thesis, and the gain pattern without metal pedestal is used for all further studies.

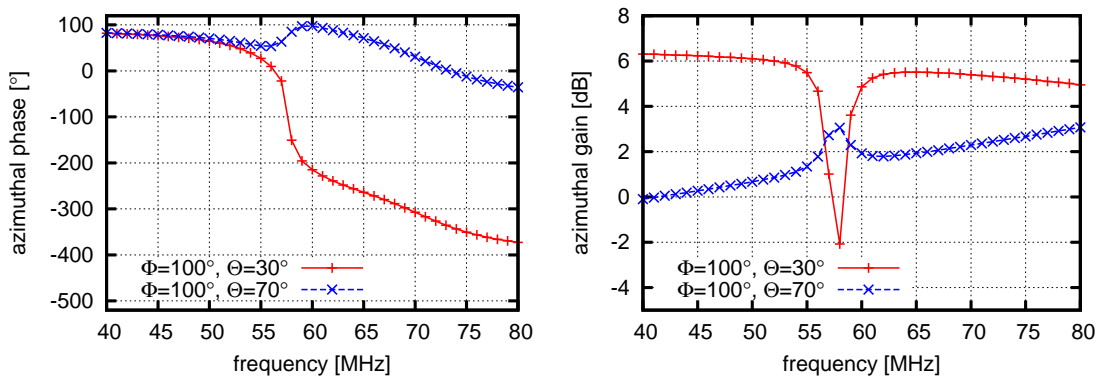


Figure 5.1: Phase (left) and amplitude (right) of the gain pattern with metal pedestal. For data analysis the peak in the amplitude at 58 MHz was avoided by interpolating between 57 and 59 MHz.

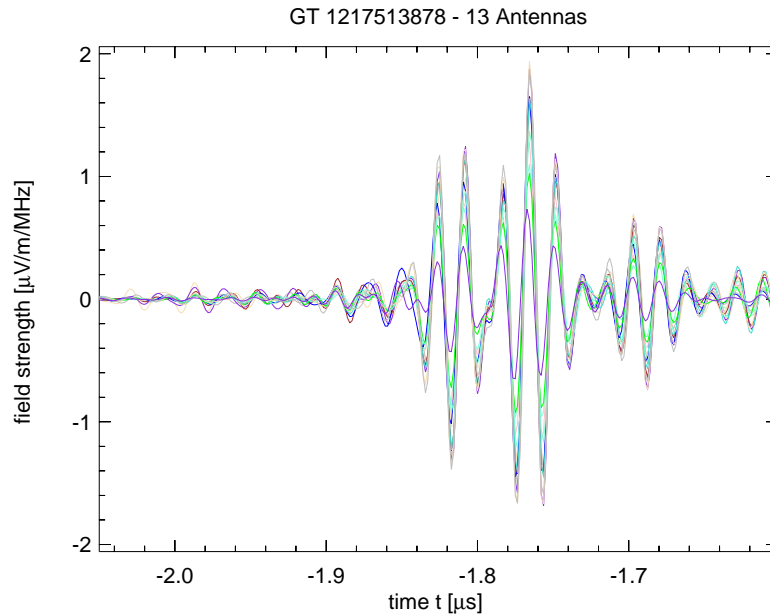


Figure 5.2: Trace of a simulated event using the gain pattern with the metal pedestal. The double pulse observed in this simulated event is not visible in data. This implies that the simulated gain pattern overestimates the influence of the pedestal.

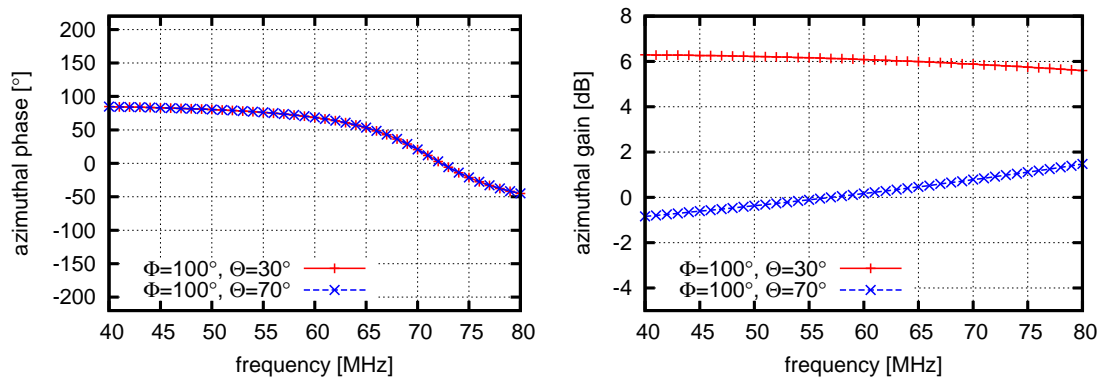


Figure 5.3: Phase (left) and amplitude (right) of the gain pattern without metal pedestal. The high gradient in the phase and the peak in the gain are not present and therefore no interpolation is necessary.

As already mentioned the gain pattern is only used to describe the directional behaviour of the antenna. The absolute amplitude is calculated from the absolute calibration with an external source, taking into account the simulated gain value for the zenith direction. This is slightly different for the simulations without the metal pedestal compared to the simulations including the metal pedestal. Therefore the change of the antenna pattern requires a recalculation of the absolute calibration factor which was performed in the scope of this work. This calibration factor only depends on the frequency.

The spatial behaviour of both simulations, with and without pedestal, differs mainly at frequencies around 58 MHz. Although the amplitude and the frequency behaviour differs slightly for both simulations the influence of the changed gain pattern on reconstructed data is small. This is also due to the fact that in the standard analysis pipeline, used for the reconstruction of data, neither azimuthal nor zenith gain themselves are considered but the “total gain” which is the sum of the individual components as described in section 3.3. In this simplified model only the real gain is considered and therefore the phase is neglected. The total gain with and without pedestal for  $\theta = 30^\circ$  and  $\varphi = 100^\circ$  is shown in figure 5.4. Both total gain values show similar spatial behaviour and comparable amplitudes which explains the minor influence on the reconstruction of data. Since the calibration factor of the absolute amplitude calibration depends on the frequency the different spectral shapes are considered.

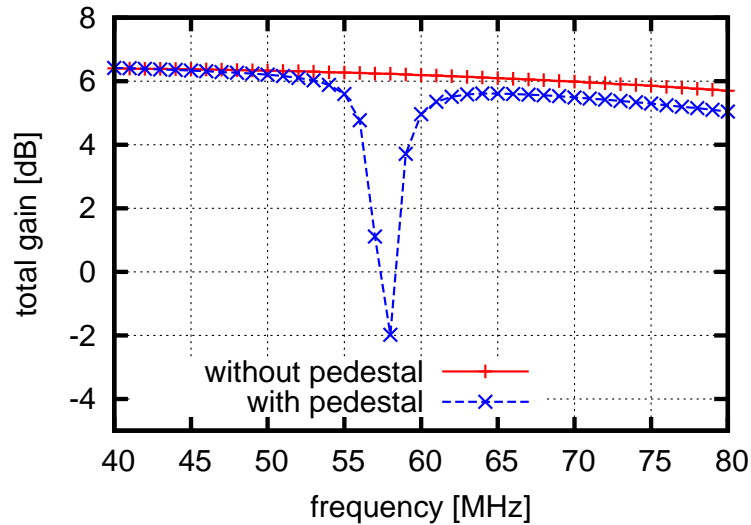


Figure 5.4: Total gain as used in the standard reconstruction pipeline for  $\theta = 30^\circ$  and  $\varphi = 100^\circ$  as a function of the frequency.

## 5.2 Implementation of the absolute amplitude calibration

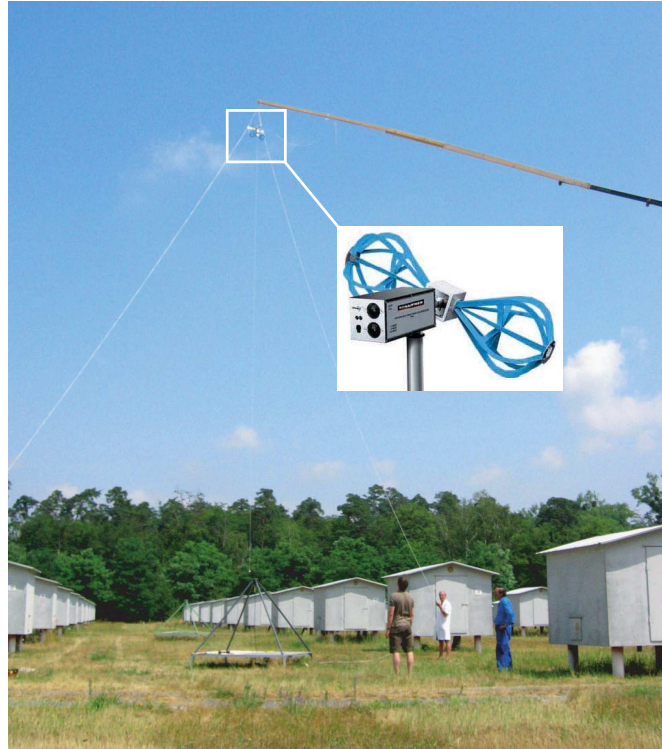


Figure 5.5: Reference source for amplitude calibration mounted on a crane above the LOPES antenna.

The LOPES experiment was the first air shower radio experiment providing an absolute amplitude calibration. The first measurements of radio emission from air showers in the 1960s showed discrepancies in the absolute amplitudes of a factor 100. An absolute amplitude calibration was one of the biggest problems at that days that also led to an interruption of the radio measurements. But for LOPES a successful absolute calibration was performed. A detailed description of this procedure was published in Nehls et al. (2008). For the calibration a reference source is mounted on a crane and positioned ten meters above the antenna as seen in figure 5.5. As reference antenna a biconical antenna, a Schaffner DPA 4000, was attached to the signal comb-generator RSG 1000. A frequency comb with 1 MHz spacing is emitted which results in a pulse train with 1  $\mu$ s periodicity. The reference antenna originally is designed for a frequency band of 300 MHz to 1000 MHz but validated and calibrated down to 30 MHz which fits the frequency range of the LOPES antenna. In the end the received signal at the ADC is compared with the expected signal, calculated from the emitted power of the reference source. In the far-field the ratio of power from the receiving and transmitting antenna is described by the transmission equation of Friis (Friis, 1946):

$$\frac{P_r}{P_t} = G_r G_t \left( \frac{\lambda}{4\pi r} \right)^2, \quad (5.1)$$

with  $P_{r/t}$  the power of the receiving and transmitting antenna, respectively, and  $G_{r/t}$  the corresponding gain.

For the LOPES calibration it has to be considered that for linear polarized antennas power is lost if the axis of both polarizations are not parallel. This loss is proportional to  $\cos^2\beta$  with  $\beta$  the angular difference between both polarization directions. The power  $P_M$  measured by the LOPES antennas is related to the receiving power by the calibration factor  $V$ :  $P_M = V * P_r$ . The receiving and transmitting power depend on the frequency so including Friis' equation the frequency dependent calibration factor is given by:

$$V(\nu) = \frac{P_M(\nu)}{P_R(\nu)} = \left(\frac{4\pi r\nu}{c}\right)^2 \frac{P_M(\nu)}{G_r(\nu)G_t(\nu)P_t(\nu)\cos^2\beta} \quad (5.2)$$

with

- $P_M$  → Power measured with the LOPES antenna
- $P_R$  → Calculated incoming power to the electronics chain of LOPES
- $\nu$  → Frequency of the emitted signal
- $r$  → Distance between LOPES antenna and reference source
- $G_r$  → Gain of LOPES antenna
- $G_t P_t$  → Product of the gain and power of the reference source, calculated from the electric field strength at 10m distance which is given by the manufacturer of the reference source
- $\beta$  → Angle between polarization axis of antennas

This amplification factor is used in the standard analysis pipeline to calculate the absolute electric field. In this chapter the procedure of the amplitude calibration, that is the calculation of the amplification factor, is investigated to eliminate potential inaccuracies in previous treatments which could possibly cause the discrepancy between data and simulations.

### 5.3 Verification of the original calibration analysis

The original evaluation of the amplification factor between the amplitude at the antenna footpoint and the electric field at the antenna was done using Glish scripting, which is integrated in the AIPS++ system (Schiebel, 1996; Croes, 1993). This is a software package mainly used by astronomers. The CASA software is based on AIPS++ and is used in the standard LOPES analysis software (McMullin et al., 2007).

A verification of the whole analysis procedure is performed by comparing the calibrated signal of an event taken during the measurement campaign to the expected signal from the reference source. The manufacturer provides a calibration sheet showing the emitted effective field strength of the reference source for different frequencies at 10 m distance. To get the electric field amplitudes these values have to be multiplied by  $\sqrt{2}$  and for the comparison with LOPES data they are divided by the bandwidth of 31 MHz. For LOPES several measurement campaigns at different dates took place and for each campaign around 20 traces are available. For the comparison these traces undergo the standard analysis pipeline which includes the amplitude calibration. The output are calibrated time traces showing the pulses from the reference source. After a Fourier transformation the frequency comb of the reference source is visible, see figure 5.6.

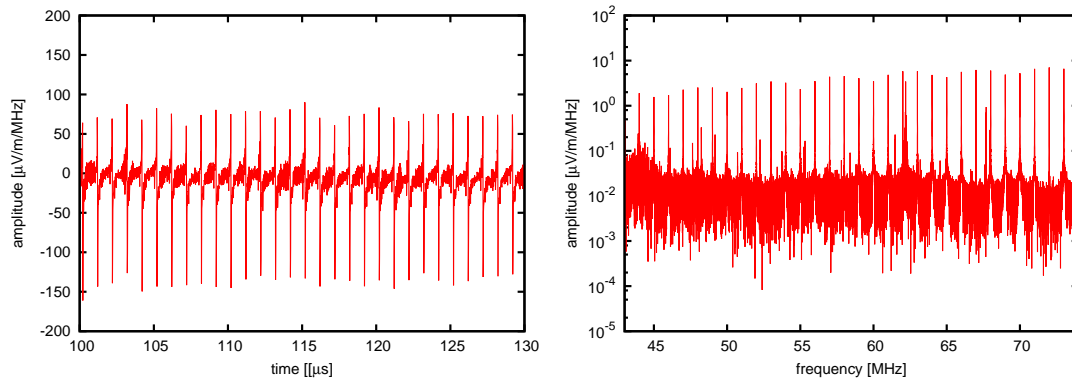


**Figure 5.6:** Reconstructed and calibrated trace (left) and frequency spectrum (right) of a single measurement during a calibration campaign. In the trace the signal of the reference source with  $1\mu\text{s}$  periodicity and in the frequency spectrum the frequency comb with 1 MHz spacing are visible.

If the peaks of the comb spectrum had a high enough resolution and were precisely at the right frequency the Fourier coefficients could be directly interpreted as the electric field amplitude and could be compared to the reference values. Since this is not the case for LOPES the electric field amplitude is calculated by quadratically adding  $\pm 5$  samples around the peak and then extracting the square root. Then the mean of each campaign is calculated, and from this also the mean over all campaigns. If the amplification factor and its application were correct, the reconstructed amplitude for each frequency would fit the one expected from the reference source. Figure 5.7 shows that the reconstructed amplitude is within the uncertainty of the reference source but the slope of the frequency is not reproduced correctly. Although this cannot explain the discrepancy of data and simulation a new calculation of the calibration values was done.

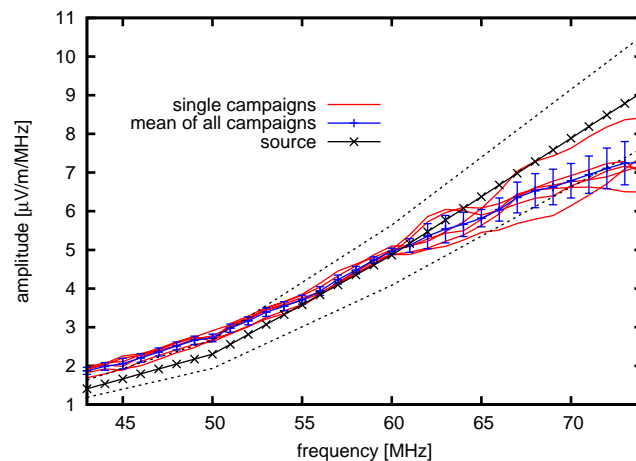


**Figure 5.7:** Mean reconstructed frequency dependence of several events taken during different measurement campaigns (red) compared to the expected frequency of the calibration source (black). In blue the mean and standard deviation of the different campaigns of one antenna are shown and the dashed black lines indicate the uncertainty of the reference source.

## 5.4 Exchange of the calibration software

To be independent of former used analysis tools the whole calculation was redone using independently developed software. The Python-based calibration software developed for Tunka-Rex (Hiller, 2016) was adopted and modified for the needs of LOPES. As an input for the calculation uncalibrated traces are necessary. These are obtained by setting the amplification factor in the LOPES standard analysis pipeline to one. The output traces can then be used as input for the Tunka-Rex software. There are two main parts which have to be revised for LOPES. First the peak amplitude is not calculated from the Fourier coefficients, but by quadratically adding  $\pm 5$  samples around the peak and then extracting the square root. And second, in contrast to Tunka-Rex LOPES not only has one measurement campaign, therefore the mean over all campaigns is calculated in the end. Dividing the expected electric field amplitude by the measured one the amplification factor is derived, see formula 5.2. These amplification factors were included in the standard analysis pipeline. As expected the new amplification factors have a slightly different frequency dependence than the old Glish-calculated ones but the same amplitude range. A comparison of the different amplification factors for one antenna is shown in figure 5.8 on the left. Also the new python-based amplification factors were verified in the same way as for the former Glish-based amplification factors as shown in figure 5.8 on the right. The newly calculated amplification factors do match the source values within uncertainties and better represent the frequency dependence.

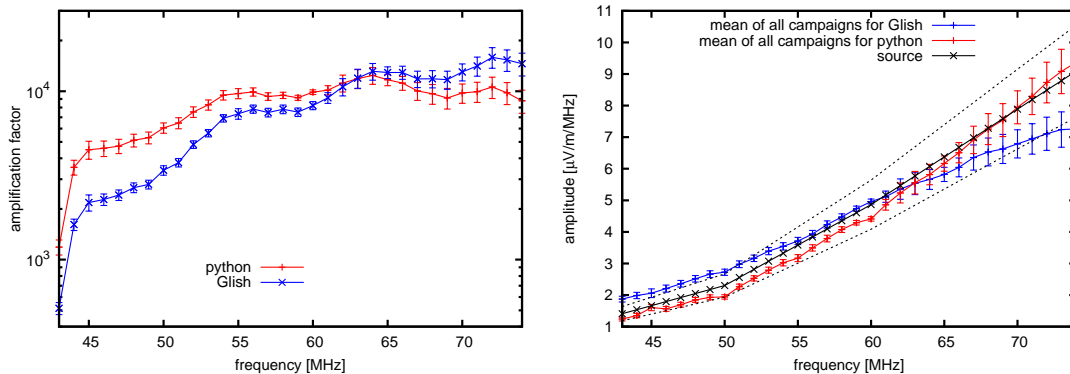


**Figure 5.8:** Left: Amplification factor calculated with different software exemplary for the same antenna as in figure 5.7. The error bars represent the fluctuations due to different environmental conditions for the different campaigns. Right: Mean reconstructed frequency dependence for the Glish- and python-based calibration compared to the expected frequency of the calibration source. The dashed lines indicate the uncertainty from the source.

## 5.5 Revised characterisation of the reference source

Tunka-Rex and LOFAR adopted the measurement technique for their amplitude calibration from LOPES and use the same reference source (Nelles et al., 2015b). This allows a comparison of the amplitudes independent of any systematic uncertainties of the reference source, which causes the main uncertainty of the amplitude scale. In the scope of such a comparison it turned out that the values from the manufacturer for the reference source do not correctly fit the needs for calibrating air shower detectors.

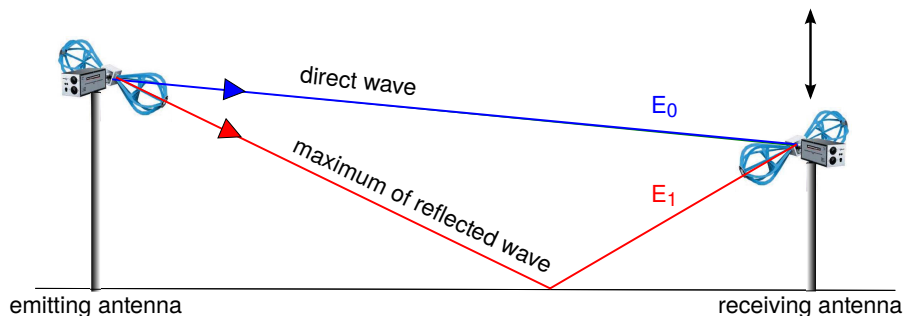


Figure 5.9: Sketch of the calibration measurements for the source antenna performed by the manufacturer.

The calibration of the source was done for free-field conditions. This includes reflections from the ground. In figure 5.9 a sketch of the calibration measurement is shown. For free-field measurements the receiving antenna is moved up and down until the maximal electric field is measured, which is the combination of  $E_0$  and  $E_1$ . For the application in air shower measurement only the direct wave of the radio signal is needed which is only  $E_0$ . For this purpose a recalibration of the reference source by the manufacturer was requested for so-called free-space conditions. Since such a measurement is hardly realisable the values are calculated from free-field measurements, by subtracting the reflected signal. This lowers the measured field strength significantly. These new reference data given by the manufacturer are shown in the appendix B and were used for a new calculation of the amplification factor using the newly developed python based software. Figure 5.10 shows the up-to-date amplification factor as well as the two outdated ones.

The rise of the amplification factor leads to a lowering of the calibrated LOPES amplitudes. On average the amplitude of the calibrated data drops by a factor of  $\sim 2.6$ . This is of the same order as the discrepancy between CoREAS simulations and LOPES data (see section 3.4) and in fact does resolve it. An updated comparison is shown in section 6.2 and was published in Apel et al. (2016). In figure 5.11 the calibrated traces for the same event are shown for both amplification factors. It is apparent that beside the considerable change of the amplitude also the frequency dependence changes slightly. Both aspects affect reconstructed parameters like the CC-beam and the lateral distribution. This has a big impact especially on all results based on the amplitude, including the comparison of data and simulation. In the next section the impact on the reconstructed parameters is shown.

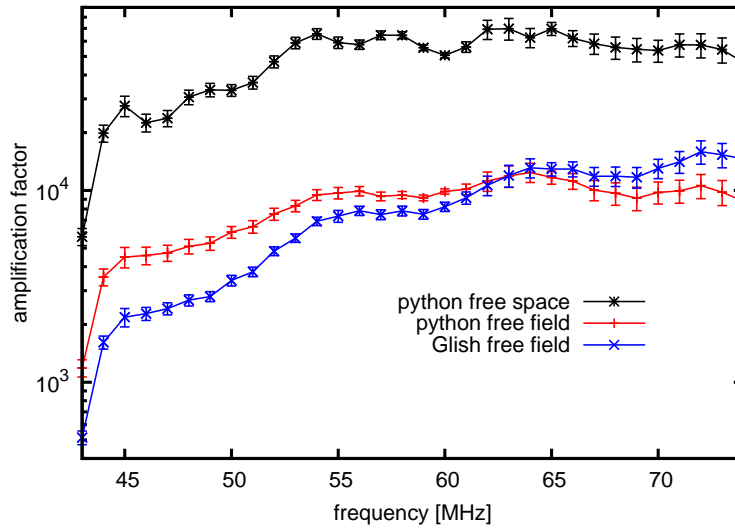


Figure 5.10: The new calculated amplification factor using the free-space condition for the reference source in comparison to the former used amplification factors for an exemplary antenna.

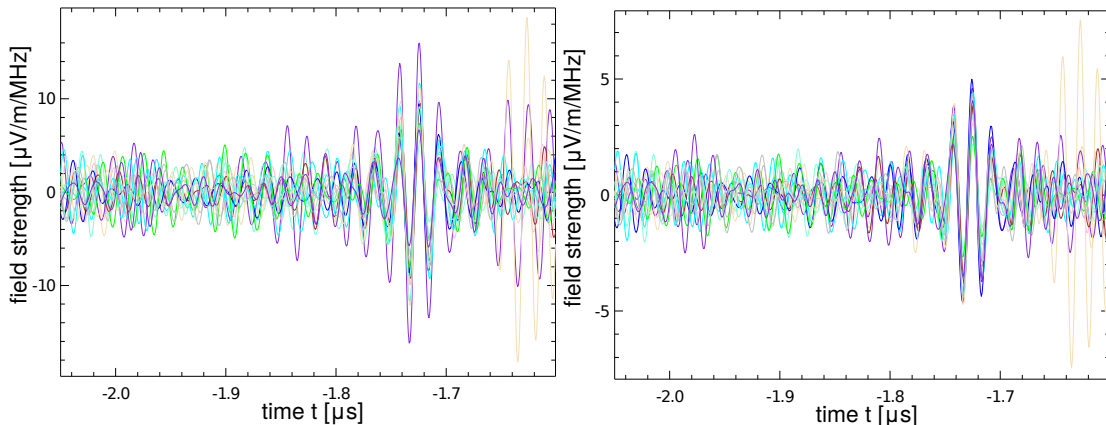


Figure 5.11: Time trace of the identical event once calibrated with the former amplification factors (left) and with the updated ones (right) using the free-space conditions. Note the different scaling.

## 5.6 Impact of revised amplitude calibration on reconstructed quantities

To describe the radio emission of air showers different parameters are used. For LOPES the most important are the lateral distribution function, described by the slope and amplitude (formula 3.4), the radio wavefront, described by the cone angle and the offset parameter (formula 3.2) and the cross-correlation beam (CC-beam) (formula 3.3). The impact of the new calibration values on each of these parameters is discussed in the following.

## CC-beam

The CC-beam is calculated inside the standard analysis pipeline to determine the time of the air shower pulse which is needed to reconstruct the measured amplitude in the single antennas as described in section 3.2. The updated calibration, now for free-space instead of free-field conditions, should not influence the coherence of the signal but only lower the amplitude. But due to the different frequency behaviour it nevertheless can slightly change the coherence and therefore the signal-to-noise ratio. This might also influence which events are selected for the analysis.

All preselected events (see section 3.5) are analysed with the same version of the the standard analysis pipeline as before, only now using the new calibration values instead of the old Glish-calculated ones. In total 487 events survive the standard quality cuts for both calibration values. For the old values 33 additional events were selected while for the updated calibration 84 additional events were selected. These additional events are mostly very close to the detection threshold and small changes in the frequency response can make the difference whether the event is selected or not. For all studies comparing both calibration values only common events are used. In figure 5.12 the resulting amplitudes of the CC-beam are compared. The error for the CC-beam amplitude is the quadratic sum of the error from the Gaussian fit of the CC-beam and the error caused by noise which was determined to be about 6 %, see section 4.2. The amplitude of the CC-beam drops by a factor of 2.58 for the revised calibration, as already expected from the difference of the calibration values. The linear correlation and the small scatter, as seen in the left plot, show that the coherence of the signal is almost not affected by the change of the calibration values.

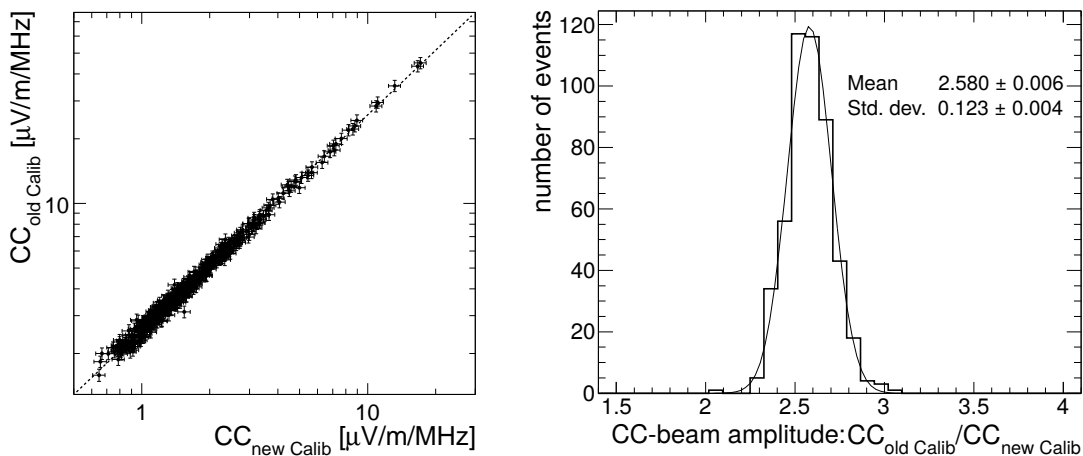


Figure 5.12: Left: Per-event comparison of the CC-beam amplitudes derived with the old and the new calibration values. The dotted line indicates a linear correlation with a slope of 2.58. Right: Ratio of the old and new CC-beam amplitudes.

Lateral distribution

As for the CC-beam the main difference for the lateral distribution is expected in the overall amplitude with only slight changes in the slope. Figure 5.13 and figure 5.14 confirm these expectations. Also the quantitative expectations are confirmed: The amplitude drops by a factor of 2.58 and the slope has an absolute difference of  $0.05 \text{ km}^{-1}$  with a standard deviation of  $0.2 \text{ km}^{-1}$ . The deviation of the slope therefore is much lower than its statistical uncertainty of about  $1.6 \text{ km}^{-1}$ , see figure 4.14 in section 4.2.

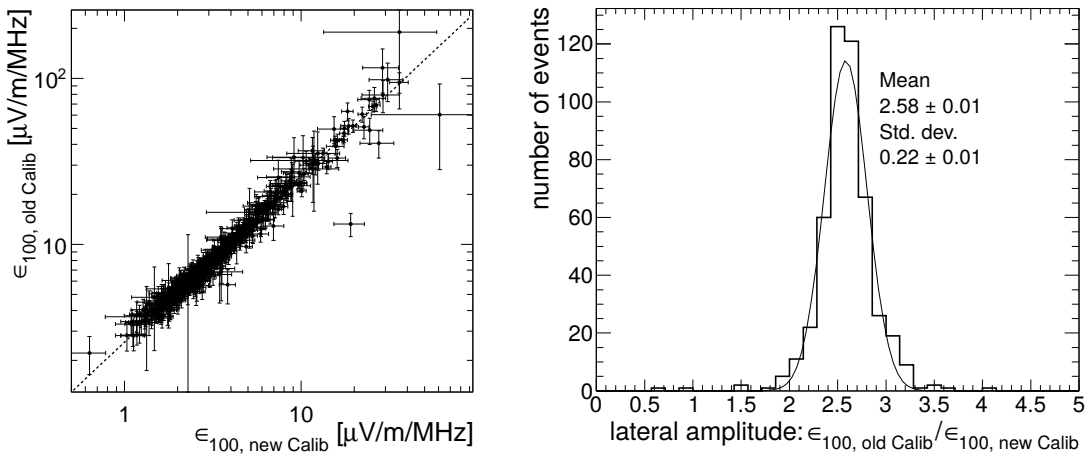


Figure 5.13: Influence of the revised amplitude calibration on the fitted amplitude  $\epsilon_{100}$  at 100 m of the lateral distribution. In the left plot a per-event comparison and in the right plot the ratio of the old and new amplitudes is shown. The dotted line indicates a linear correlation with a slope of 2.58.

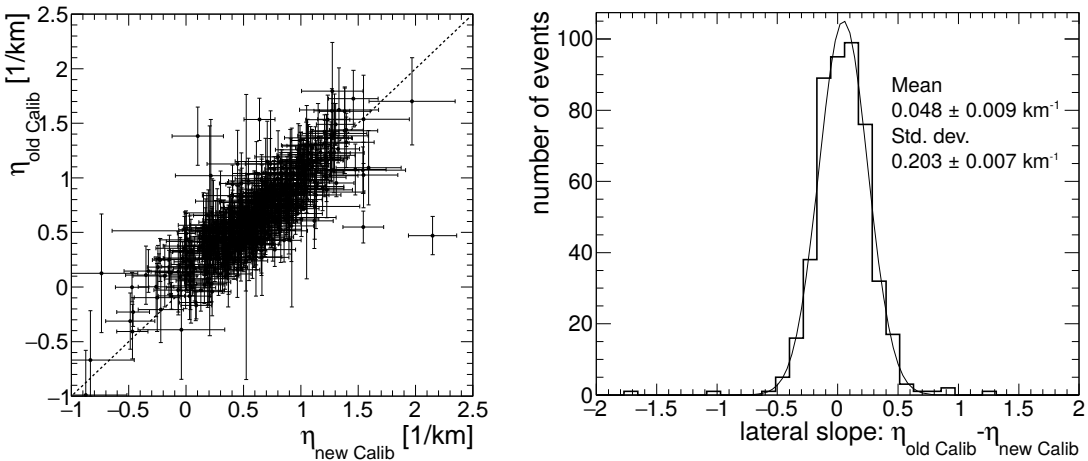


Figure 5.14: Influence of the revised amplitude calibration on the fitted slope  $\eta$  of the lateral distribution. In the left plot a per-event comparison of the old and new slope parameters and in the right plot the absolute difference between them is shown. Here the dotted line indicates identity.

### Radio wavefront

As described in section 3.2 the radio wavefront can be calculated in two ways in the LOPES analysis pipeline. The wavefront is reconstructed during the interferometric analysis and furthermore a fit on the lateral time distribution is performed. The latter suffers highly of the uncertainties of the LOPES experiment and is not used for the reconstruction of shower parameters from data and therefore it is not considered here. Former studies showed that a hyperbolic wavefront is a suitable approximation for the radio wavefront. In principle it depends on two parameters, the opening angle  $\rho$  of the asymptotic cone and an offset parameter  $b$ . As published in Apel et al. (2014b), good results are obtained for a fixed offset parameter  $b=-3$  ns. Figure 5.15 shows the opening angle  $\rho$  obtained by the maximization of the CC-beam assuming a hyperbolic wavefront with the fixed offset parameter. The uncertainties were obtained by the study of the noise influence presented in section 4.2. As the cone angle is independent of the height of the amplitude it only shows slight changes due to the different frequency dependence.

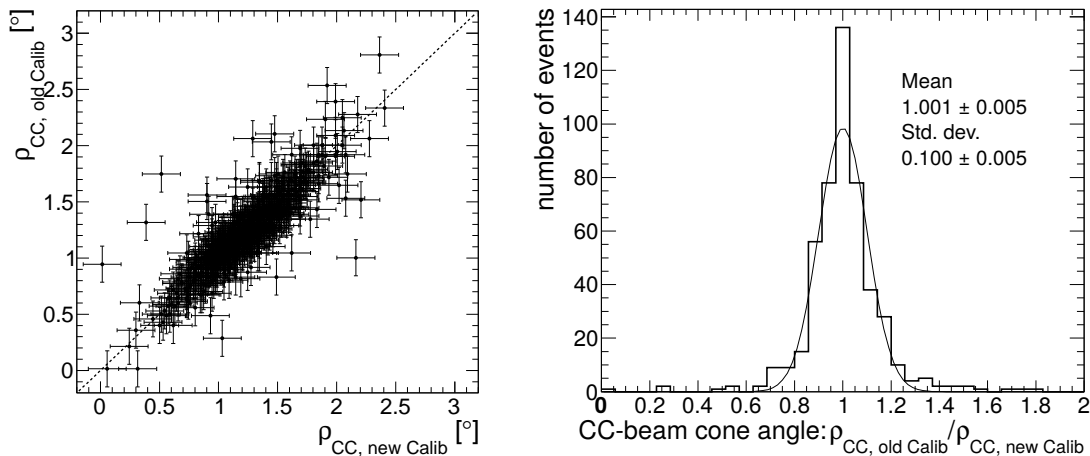


Figure 5.15: Cone angle obtained by hyperbolic beamforming for the old and new amplitude calibration values. In the left plot the per-event comparison and in the right plot the ratio of the two values is shown. The dotted line indicates identity.

## 5.7 Conclusion

To exclude any inconsistencies of the amplitude calibration of the LOPES experiment all included parts were reviewed here.

A closer look at the simulated antenna gain, also with the help of the detector simulation, showed that the effect of the metal pedestal below the LOPES antennas is overestimated in the simulations. This led to double pulses applying the detector simulation on CoREAS simulated events, mainly caused by the high gradient in the phase. Therefore the simulations not considering the metal pedestal are now used, which describe the data more realistically.

In the next step the original calculation of the absolute amplification factor was revised

and a discrepancy between reconstructed spectra and the spectrum of the calibration source was found. Using a different independently developed analysis software solved this discrepancy and slightly different calibration values were obtained.

Both aspects had only minor effects on the reconstructed amplitude and could not explain the observed discrepancy between LOPES measurements and CoREAS simulations.

Finally it turned out that the calibration values, provided by the manufacturer, for the reference source were obtained for free-field conditions. But for the application as a reference source for air shower radio experiments a calibration under free-space conditions is needed. A recalibration of the reference source was obtained from the manufacturer and the new reference values differ by a factor of around 2.6 and could resolve the discrepancy.

The change of the amplitude due to the revised calibration requires a revision of all former results. Especially those based on amplitude parameters like the CC-beam and  $\epsilon_{100}$ , while the results based on the slope and on the cone angle are almost unaffected by the change of the calibration values. Since the amplitude changed by a factor of 2.6 it is expected that also the correlation of the amplitude with the energy changes by a similar factor.

Results for the reconstruction of the shower maximum should remain the same since they are based on the slope and cone angle which are hardly affected. Also the reconstruction of the arrival direction, which is based on the interferometric reconstruction should be independent of the updated calibration.

The comparison of LOPES data with simulations is of course strongly affected by the revised calibration. Detailed comparisons of data and simulations are presented in chapter 6.

The complete absolute amplitude calibration is now based on a reliable analysis and the revision could finally solve the open question of the difference between measured and simulated amplitudes for LOPES and CoREAS.

## 5.8 Cross-Calibration with LOFAR and Tunka-Rex

With the updated amplitude calibration a cross-calibration with LOFAR and Tunka-Rex was performed. This was mainly done by the LOFAR collaboration with the support of LOPES and Tunka-Rex. The results are published in Nelles et al. (2015b). All three experiments now use the same reference antenna for the calibration and can therefore be compared independent of the systematic uncertainty introduced by the reference source. Figure 5.16 shows a calibrated pulse of the reference source measured by the three different radio experiments. These pulses were obtained using the different independent standard pipelines of the three experiments. To allow a comparison the amplitudes are scaled to a source at ten metres distance and are filtered to the LOPES bandwidth of 43-74 MHz. The upsampled traces after application of a Hilbert envelope are shown. For LOPES the calibration is performed several times under different environmental conditions. The averaged calibration value is applied on a typical event and therefore it does not necessarily reproduce the exact amplitude of the reference source. For LOFAR and Tunka-Rex only one calibration campaign is performed and therefore not averaged over several calibration values. The calibrated pulses should

therefore reproduce the exact amplitude of the reference source. The amplitude of the pulse measured by LOPES is slightly smaller than for the other experiments but within the uncertainties arising from the different environmental conditions of  $\sim 20\%$  all three are comparable.

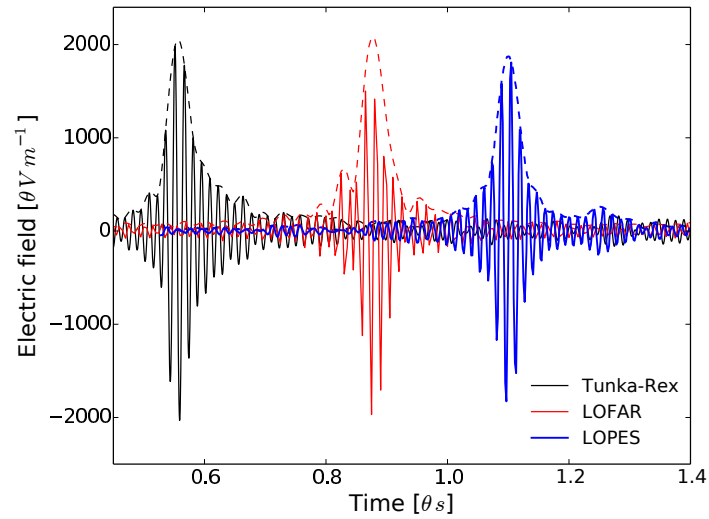


**Figure 5.16:** Calibrated upsampled pulses obtained during amplitude calibration from the source for the three experiments Tunka-Rex, LOFAR and LOPES.



# 6

## Revision of former results using the improved analysis

*In the scope of this work, parts of the analysis presented in this chapter have already been published as a contribution to the following papers:*

- Hiller, R. (Tunka-Rex- and LOPES-Collaboration), *A comparison of the cosmic-ray energy scales of Tunka-133 and KASCADE-Grande via their radio extensions Tunka-Rex and LOPES*, submitted to Physics Letters B, 2016 (Hiller et al., 2016)
- Apel, W. D. et al. (LOPES-Collaboration), *Improved absolute calibration of LOPES measurements and its impact on the comparison with REAS 3.11 and CoREAS simulations*, Astroparticle Physics, 2016 (Apel et al., 2016)
- Link, K. et al. (LOPES-Collaboration), *Revised absolute amplitude calibration of the LOPES experiment*, Proceedings of Science, ICRC 2015 (Link et al., 2016)
- Schröder, F. G., Link, K. et al. (LOPES-Collaboration), *New results of the digital radio interferometer LOPES*, Proceedings, ICRC 2015 (Schröder et al., 2016)

---

This chapter provides an updated analysis of the LOPES data including all improvements made in the last years, not only in the scope of this work. Within the standard pipeline this includes the hyperbolic beamforming (Apel et al., 2014b) also using an enhanced grid for the beamforming (Lapp, 2013), an improved fit procedure for the lateral distribution and the presented exchange of the gain pattern (section 5.1). The simulations are now analysed using the full detector simulation with and without added noise (section 4.2) and by applying the standard pipeline, including the beamforming. With the actual knowledge, the complete data set, up-to-date software and state-of-the-art simulations former important results concerning air shower parameters and comparisons of data and simulations are reviewed. These are all based on some fundamental

properties of the radio emission namely the lateral distribution function, the cross-correlation beam and the shape of the radio wavefront. In the appendix A, histograms of these properties are presented. In the following section their uncertainties are discussed.

With the improved analysis, the preselected events were analysed again and the same quality cuts were applied, as described in section 3.5. The cut based on the CC-beam quantities results in consistently higher numbers of events which are presented in table 6.1.

Although more events survive the quality cuts for the improved analysis, the old selections are not fully included in the new one. A common data set exists of 487 events. These common events are used in the following analysis since only for these events also corresponding CoREAS simulations are available. For investigations solely based on measurements that are analysed with the improved pipeline all 578 events are used.

**Table 6.1:** Number of events after applying the quality cuts for the different LOPES setups and divided into KASCADE (K) and KASCADE-Grande (G) selections.

setup	LOPES 30 K	LOPES 30 G	LOPES Dual K	LOPES Dual G	sum
old analysis	91	40	244	186	527
improved analysis	103	50	263	201	578
				common	487

## 6.1 Discussion of uncertainties

### Lateral distribution

The amplitude  $\epsilon_{100}$  and the slope  $\eta$  are both obtained by an exponential fit to the lateral distribution, which depends on two quantities, the distance to the shower axis and the amplitude of the individual antennas.

The uncertainty of the distance to the shower axis is mainly determined by the uncertainty of the shower core. This uncertainty is provided by KASCADE-Grande with 4 m for KASCADE and 7 m for KASCADE-Grande events.

The amplitude uncertainty for individual antennas is the quadratic sum of the uncertainty from noise and the uncertainty from the calibration. The calibration uncertainty affecting individual signals is determined to be 5% (Schröder, 2011). The uncertainty from noise is determined within the noise correction analysis and does depend on the signal-to-noise ratio, see Schröder et al. (2012). It amounts to up to 80% for low signal-to-noise ratios and drops below the calibration uncertainty for signal-to-noise ratios above 13.

The uncertainties for the individual amplitudes and for the shower core are considered within the fit procedure of the lateral distribution which means the statistical uncertainties for  $\epsilon_{100}$  and  $\eta$  from the fit directly contain the above-described uncertainties. For the uncertainty of  $\epsilon_{100}$  an additional event-to-event uncertainty from the amplitude calibration caused by differing environmental effects of 5% is quadratically added

to the statistical uncertainty provided by the fitting routine. The derived uncertainties for  $\epsilon_{100}$  and  $\eta$  are shown in figure 6.1. For the slope parameter  $\eta$  the absolute values are shown since the relative uncertainties can become quite large for events with an essentially flat lateral distribution where  $\eta$  is almost zero. Relating the mean absolute uncertainty of  $\eta$  to the mean value of  $\eta$ , which is around  $5.3 \text{ km}^2$  as shown in the appendix A, leads to a relative uncertainty of around 27 % for  $\eta$ .

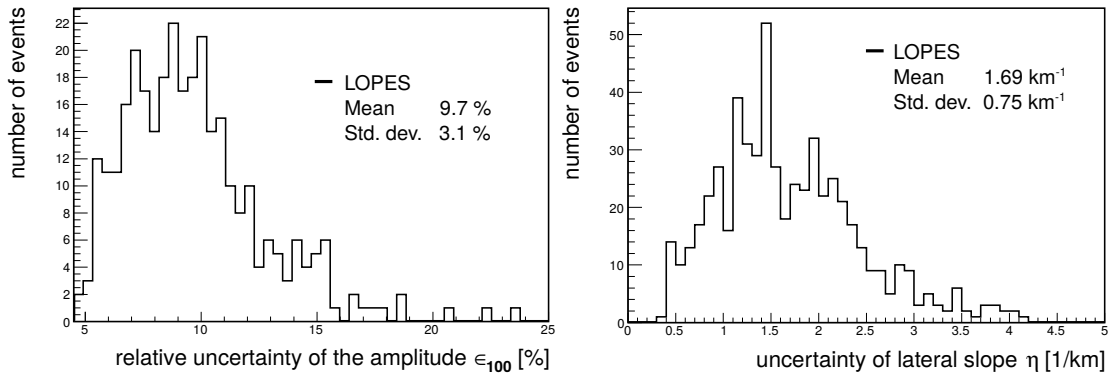


Figure 6.1: Distribution of the relative uncertainty for the lateral amplitude parameter  $\epsilon_{100}$  (left) and the absolute uncertainty for the lateral slope parameter  $\eta$  (right) derived from the fit of the lateral distribution.

In section 4.2 the noise correction applied in the standard reconstruction pipeline was tested using the detector simulation. For the amplitude the noise correction works fine and no additional uncertainty needs to be considered. Also the influence of the simplified reconstruction on  $\epsilon_{100}$  by 2 % is negligible compared to the statistical uncertainty of 10 %. For the slope parameter the noise correction seems to be insufficient since still a systematic decrease by  $1 \text{ km}^{-1}$  of the slope is observed when including noise. By chance this decrease cancels out with the increase caused by the simplified reconstruction applied in the standard LOPES pipeline. Therefore, at least for a statistical analysis, this systematic uncertainties need not be considered, see also section 4.6. For single events one or the other effect might dominate, depending on the signal to noise ratio and on the geometry. Analyses based on the slope of single-events need to consider both effects as additional uncertainties.

When comparing different events or even different experiments or simulations, further uncertainties need to be considered. These arise mainly from the amplitude calibration. Environmental effects which are in the order of 4.5 % have to be considered when comparing different LOPES events with each other. The main uncertainty for comparisons with other experiments or simulations is the scale uncertainty of the reference source which is 16 %. All these numbers are derived for electric field amplitudes and need to be doubled when considering power quantities.

Only the uncertainties for the individual antennas need to be considered for the slope since all the other sources of uncertainty affect all antennas in the same way and the slope should remain the same.

Regarding simulations the uncertainties mainly depend on the treatment of the simulations and whether measured noise is added or not. The amplitude at the single antennas and the shower core are known exactly for the pure simulations and the statistical uncertainties for  $\epsilon_{100}$  and  $\eta$  only arise from the fit procedure. When using the end-to-end

simulations the determination of the uncertainties for single antennas is adopted from data. The uncertainties are calculated from the mean noise for all end-to-end simulations but the noise correction is only applied to simulations including measured noise. Event-to-event uncertainties caused by the calibration are not considered for the simulations.

For comparison between data and simulations an additional scale uncertainty arising from the energy reconstruction by KASCADE-Grande of 20 % becomes important. The energy is used as input for the CoREAS simulations and thus gives rise to an additional uncertainty on the overall scale of the simulated events.

### CC-beam

Using the detector description for a comparison of the reconstructed CC-beam amplitude and the cone angle  $\rho_{CC}$  for simulations with and without noise gives the opportunity to determine an uncertainty induced by noise on these quantities. This was done in section 4.2. For the cone angle  $\rho_{CC}$ , no systematic shift is observed and also for the amplitude the effect is small with 2 %. The statistical uncertainty from noise is less than 6 % for the amplitude and around 12 % for the cone angle. For the amplitude an additional uncertainty, derived from the Gaussian fit applied within the standard analysis to the CC-beam (see section 3.2), is added quadratically to the 6 % but this fit uncertainty is only around 1 %.

Furthermore, as for the amplitude parameter  $\epsilon_{100}$ , the scale uncertainties from the reference source of the absolute amplitude calibration of 16 % and the scale uncertainty of the KASCADE-Grande energy of 20 % needs to be considered for the CC-beam amplitude, comparing data and simulations.

### Lateral time distribution

The cone angle can in principle also be reconstructed by a fit to the lateral time distribution, but for measurements the uncertainties are too high to get reliable results. A detailed discussion of these uncertainties is provided in Apel et al. (2014b). There, three main sources of uncertainties are revealed: The uncertainty of the arrival times, the uncertainty for the zero-time  $t_0$  and the uncertainty on the distance to the shower axis.

The distance-uncertainty is mainly arising from the uncertainty on the core position reconstructed by KASCADE-Grande. Transferred to a timing uncertainty this amounts to approximately 7 ns for the average zenith angle of 30°.

The uncertainty of the arrival time is determined by the calibration uncertainty of 2 ns and by the uncertainty from noise. Depending on the signal-to-noise ratio in the individual antennas this uncertainty can reach up to 17 ns. The uncertainty for the arrival time and for the distance are taken into account for the fit of the lateral distribution.

The uncertainty on the zero-time is more complicated. Theoretically the zero-time is defined as the time when the radio front hits the ground at the core. This can only be measured directly by extremely dense arrays. For LOPES the zero-time is determined by the time of the CC-beam maximum. A quantification of the uncertainty introduced by this is not easy and needs further investigations.

As for the other properties also for the fit of the lateral time distribution the influence

introduced by the detector and the standard reconstruction was studied. A significant difference was found between pure simulations and end-to-end simulations, see section 4.5. This suggests that the reconstruction of the zero-time used so far within the standard analysis pipeline does not work properly. As already stated before, this needs further investigations and therefore the cone angle from the lateral time distribution derived for data and end-to-end simulations is not used for further analysis.

For pure simulations the arrival times, the zero-time and the distance to the shower axis are known exactly. Therefore a reconstruction of the cone angle via the lateral distribution function gives reliable results for simulations.

## 6.2 Comparison of data and simulations

One important goal of this thesis was to understand previously found discrepancies between LOPES data and CoREAS simulations, see section 3.4. Now it is not only clear where the discrepancy came from but it could even be resolved. The free-field calibration values for the reference source used for the amplitude calibration were replaced by those for free-space, which better fit the need of air shower measurements. The newly derived calibration values for the absolute amplitude calibration were determined and are used for an updated comparison.

Before the development of CoREAS the REAS3.11 simulation code was the state-of-the-art. The main difference between the two codes is that REAS3.11 is based on histograms of the particle distribution derived by air shower simulations of CORSIKA while CoREAS is directly implemented in CORSIKA and therefore uses the true particle distribution. This more advanced approach led to a drop in the amplitude of a factor around two. Just by chance the LOPES amplitude using free-field calibration fit to the REAS3.11 expectations. This was the reason why for a long time there was no hint on any discrepancies of LOPES data and simulations. Only with the progress of simulating radio emission from air showers this mistake was revealed.

With the new amplitude calibration and the full detector simulation, both developed in the scope of this work, a sophisticated comparison of data and CoREAS simulations is now possible. This allows a final quantitative comparison of measurements and CoREAS simulations. The compared radio emission quantities are now derived in the same way for data and simulations and also measured noise is considered for simulations. In addition to the reconstructed lateral distributions also the CC-beam amplitude and the cone angle derived from the interferometric analysis are now available for simulations and used for the comparison. A direct comparison of LOPES data with CoREAS simulations including detector effects and noise is performed. The obtained results are presented in this chapter.

As basic event selection the common set of events with available simulations is used. Furthermore additional cuts for individual needs are necessary, e.g. for a successful fit of the lateral distribution.

## 6.2.1 Lateral distribution

A comparison of the lateral distributions from LOPES data using the old calibration values with REAS3.11 and CoREAS was published in Apel et al. (2013a). An update of this, based on the new amplitude calibration but still using pure CoREAS simulations is published in the short article Apel et al. (2016). A comparison based on end-to-end simulations and using the improved analysis, including the updated calibration values, is discussed in this chapter.

An example lateral distribution derived for LOPES data, pure simulation (only band-pass filter) and end-to-end simulation (including detector simulation, simplified reconstruction and noise) is shown in figure 6.2. All following comparisons are based on such lateral distributions for data and end-to-end simulations.

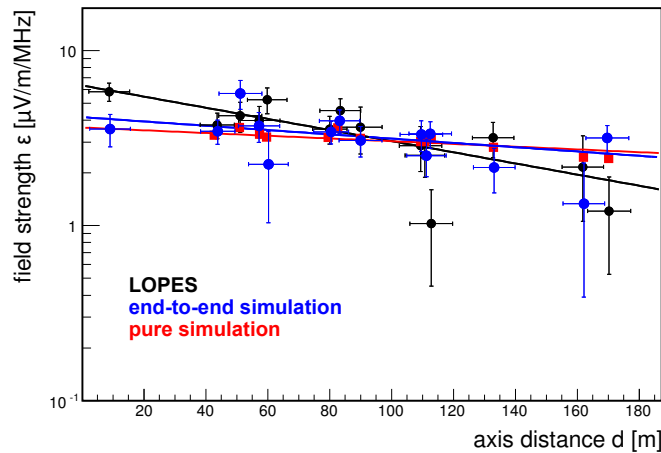


Figure 6.2: Lateral distribution for an example event fitted by an exponential function. In black the LOPES data, in red pure simulations and in blue end-to-end simulations including noise for an iron primary particle are shown.

As additional quality cuts the same signal-to-noise ratio threshold as applied on data is also applied on simulations and only if both, the simulated and measured events, pass the cuts they are used in the analysis. For former comparisons of data and simulations no additional cut on the signal-to-noise ratio for the simulated events was necessary since they were based on pure simulations which did not include noise. This additional cut reduces the number of events noticeable since many are close to the threshold and small differences in the signal-to-noise ratio of the CC-beam lead to a rejection of these events. Furthermore, a successful lateral fit is required which leads to 380 of the original 487 common events used in the following analysis. The distribution of the amplitude parameter  $\epsilon_{100}$  and the relative deviation is shown in figure 6.3 while a per-event comparison is presented in figure 6.4.

On average the amplitude is properly described by CoREAS simulation since the mean value of LOPES with  $4.4 \mu\text{V}/\text{m}/\text{MHz}$  is compatible with the mean values derived for proton and iron with  $4.3 \mu\text{V}/\text{m}/\text{MHz}$  and  $3.8 \mu\text{V}/\text{m}/\text{MHz}$ , respectively. The outliers, already seen in former comparisons (Apel et al., 2013a), are still visible and are therefore not introduced by the simplified reconstruction. The overall good agreement is also confirmed by a direct comparison of the deviation for single events: Iron-initiated

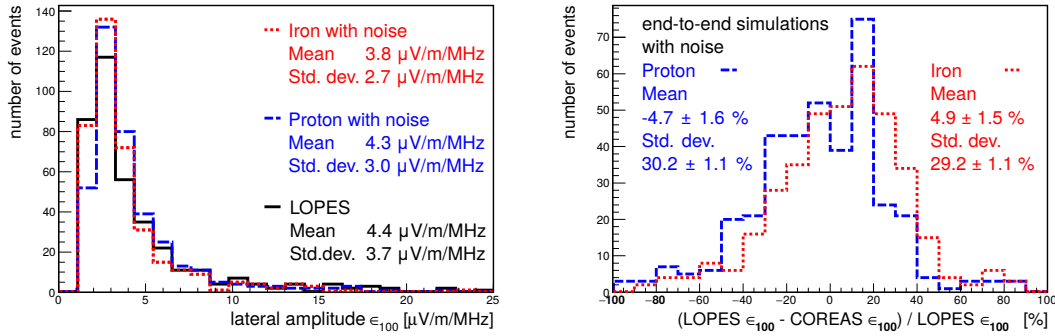


Figure 6.3: Left: Distribution of the amplitude parameter  $\epsilon_{100}$  for LOPES data as well as for proton and iron CoREAS simulations. Right: Relative deviation between data and simulations for  $\epsilon_{100}$ .

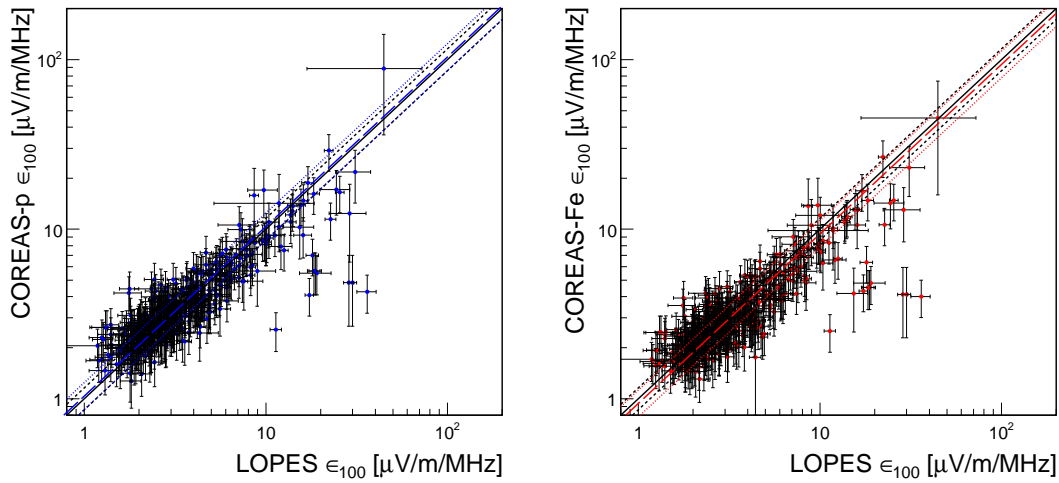


Figure 6.4: Per-event comparison of the amplitude for LOPES data and CoREAS-simulated events for proton (left) and iron (right) primaries. The black solid line indicates identity while the black dashed lines indicate the one sigma calibration uncertainty from the reference source. The coloured solid lines are shifted by the scale factor, see figure 6.5, and the dashed coloured lines indicate the 20% energy uncertainty of KASCADE-Grande.

events have slightly lower amplitudes while proton-initiated events have slightly higher amplitudes.

This difference in the amplitude is caused by the different fraction of primary energy in the electromagnetic component for the different primary particles. As input for the simulations the total energy provided by KASCADE-Grande is used and this leads to different electromagnetic energies depending on the primary particle mass for the same input energy.

For a statistical study whether the spread visible in the per-event comparison is as expected by the uncertainties, the relative deviation of the scaled  $\epsilon_{100}$  is calculated using the following formula:

$$\Delta\epsilon_{rel} = \frac{\epsilon_{100,LOPES} - f_{scale}\epsilon_{100,CoREAS}}{\sqrt{\sigma_{LOPES}^2 + f_{scale}^2\sigma_{CoREAS}^2}}, \quad (6.1)$$

with the fitted amplitude  $\epsilon_{100}$  and the statistical uncertainty from the fit  $\sigma$  for LOPES data and CoREAS simulations, respectively.

The scaling factor  $f$  is derived to gain a centred Gaussian fit to the distribution, as shown in figure 6.5. This procedure was first applied in Apel et al. (2013a) and is adopted here. The derived scaling factors are 0.97 for proton and 1.07 for iron. This differs significantly from the values published before the revised amplitude calibration where a scaling factor of 2.46 was derived for proton and 2.70 for iron, see figure 6.6 on the left and table 6.2. The new results show a very good agreement of LOPES and CoREAS concerning the amplitude. Less than 7 % deviation is clearly below the scale uncertainty from the calibration source of 16 % and from the scale uncertainty of the energy reconstruction by KASCADE-Grande which is 20 %.

A standard deviation of the fitted Gaussian of one implies a perfect estimation of the individual uncertainty and no correlation between them. The observed deviation is slightly below one which might be due to a small overestimation of the statistical uncertainties or due to a correlation of the uncertainties. The latter could be due to geometrical asymmetries of the lateral distribution which are correctly reproduced by simulations and thus lead to correlated uncertainties using a one-dimensional LDF.

In the update paper Apel et al. (2016) the scaling factors slightly differ, see figure 6.6 right and table 6.2, which is due to the fact that there pure simulations and not end-to-end simulations are used. But independent of whether pure or end-to-end simulations are used, in any case, LOPES data and CoREAS simulations are now in agreement for the amplitude parameter  $\epsilon_{100}$ .

Also the slope parameter  $\eta$  is still in good agreement as shown in figure 6.7. As expected the average slope of data is between the average values for proton and iron. Also the distribution of the uncertainty is reproduced by the simulations including noise. As explained in section 3.5.1 a per-event comparison for the slope is not suitable due to shower-to-shower fluctuations.

**Table 6.2:** Scaling factors and deviation between LOPES data and CoREAS simulations for different treatment of simulations - pure and end-to-end simulations - and for the old and new calibration values.

simulations	noise	calibration values	$f_{scale}(\text{Fe})$	Std. dev. iron [%]	$f_{scale}(\text{p})$	Std. dev. proton [%]
end-to-end	yes	new	1.07	$0.93 \pm 0.04$	0.97	$0.95 \pm 0.04$
pure	no	new	1.09	$0.98 \pm 0.04$	0.98	$0.95 \pm 0.04$
pure	no	old	2.70	$0.96 \pm 0.03$	2.46	$0.90 \pm 0.03$

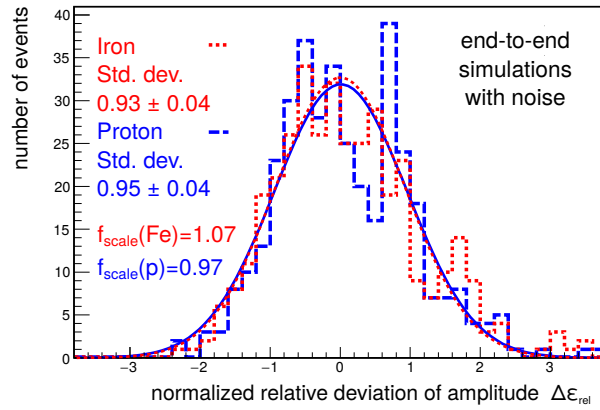


Figure 6.5: Normalized relative deviation between LOPES data and end-to-end simulations including noise of scaled  $\epsilon_{100}$  fitted with a Gaussian function.

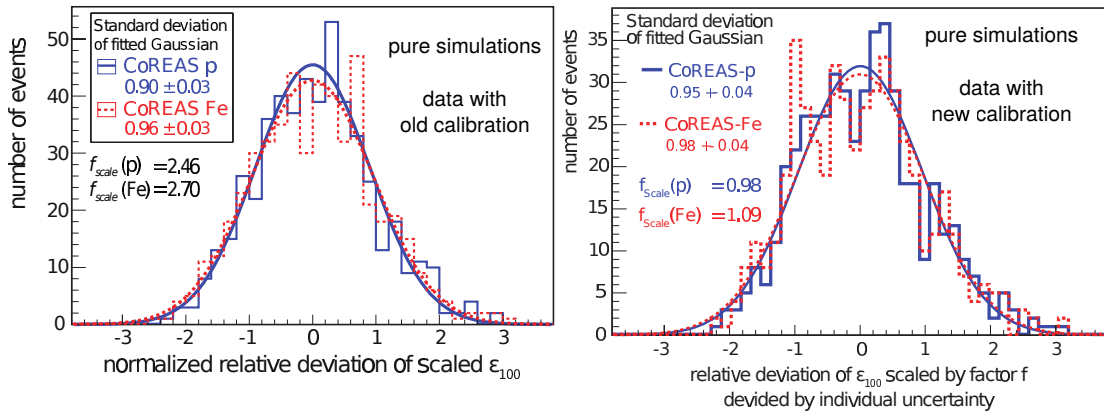


Figure 6.6: Former results as published in (Apel et al., 2013a) (left) and (Apel et al., 2016) (right). Normalized relative deviation of scaled  $\epsilon_{100}$  fitted with a Gaussian function. On the left for pure simulations and LOPES data derived with the former amplitude calibration and on the right for pure simulations and LOPES data derived with the updated amplitude calibration.

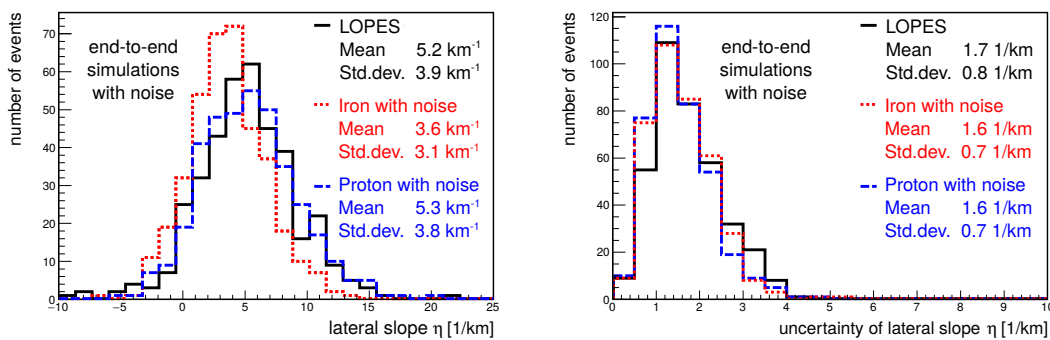


Figure 6.7: Distribution of the slope parameter  $\eta$  (left) and its derived uncertainty (right) for LOPES data and CoREAS end-to-end simulations including noise for both proton and iron initiated showers.

### Dependence on zenith angle

Former studies showed a dependence of the amplitude ratio of data and simulations on the zenith angle (Apel et al., 2014a). In figure 6.8 this dependence is still visible, for both KASCADE and KASCADE-Grande events. This means that one formerly possible reason, namely the influence from the simplified reconstruction, is now ruled out.

Another possible reason would be a zenith dependence in the reconstructed KASCADE(-Grande) energy which is used as input for the CoREAS simulations. This assumption is strengthened by the slightly different behaviour for KASCADE and KASCADE-Grande events and is therefore investigated in more detail. For KASCADE events the main impact is visible in the zenith range from  $40^\circ$  to  $45^\circ$  ( $\cos(\theta) < 0.75$ ). Zenith angles above  $40^\circ$  are not included in the standard analysis of KASCADE(-Grande) and therefore it is unknown whether the energy reconstruction is still valid there or might degrade. Furthermore, the reconstruction is not optimized for the energy range used for LOPES but for lower energies.

For the KASCADE-Grande events a striking peak at around  $25^\circ$  is visible, which is caused by some outliers in this angular bin. The reason for these outliers needs to be further investigated. In the other angular bins the same trend as for KASCADE is observed but even more distinct. A simple way of testing a zenith dependence in the KASCADE-Grande data is to calculate the trigger rate depending on the zenith angle. For the preselected LOPES events no significant dependence was observed, neither for KASCADE nor for KASCADE-Grande. This rules out that the observed zenith dependence is caused by the energy reconstruction.

An incorrect simulation of the antenna gain is still one possible explanation as well as an incorrect description of the zenith dependence in the CoREAS simulation code. This can be studied with other experiments using different antenna types. In the scope of a joint paper from LOPES and Tunka-Rex the zenith dependence was studied in more detail, see also section 6.4.3 and Hiller et al. (2016). The amplitude per energy was studied as a function of the zenith angle for data and simulations. While for LOPES a difference between measurements and simulations was observed this was not seen for Tunka-Rex. Since Tunka-Rex uses a different type of antenna the observed behaviour leads to the conclusion that the simulated zenith dependence of the gain pattern for

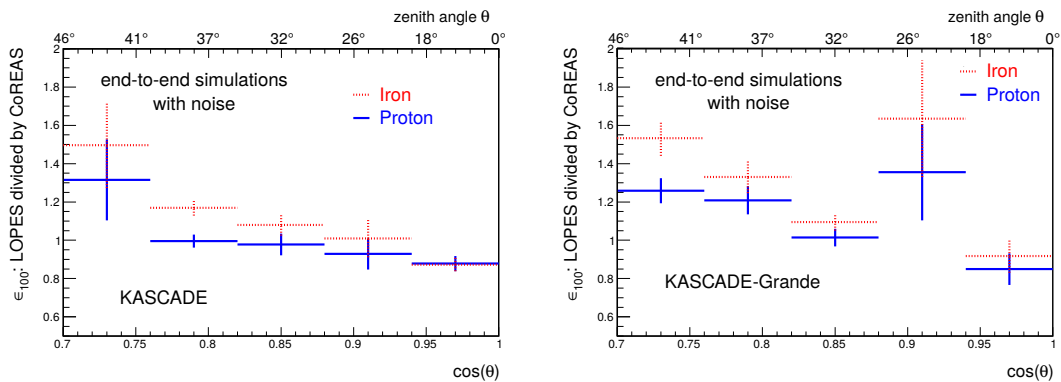


Figure 6.8: Ratio of the measured and simulated amplitude parameter  $\epsilon_{100}$  as a function of the zenith angle for KASCADE events (left) and KASCADE-Grande events (right).

the LOPES antennas is the most probable reason for the zenith dependence of the ratio between measured and simulated amplitudes.

### 6.2.2 CC-beam amplitude and cone angle $\rho_{CC}$

With the newly developed detector simulation it is possible to perform the same interferometric analysis on simulated events as previously only done on measurements. This enables, for the first time, a comparison of the amplitude of the CC-beam between data and simulations. Likewise, the cone angle  $\rho_{CC}$  of the wavefront, determined via the CC-beam can now be compared between LOPES data and CoREAS end-to-end simulations including noise.

#### CC-beam amplitude

For the amplitude of the CC-beam a per-event comparison is shown in figure 6.9. A linear function with the slope  $k$  is fitted, which shows on average a good agreement of data and simulations. For simulations using proton as primary particle the proportionality constant is slightly above one while for iron it is slightly below one. But the deviation from one is small compared to scale uncertainties from the energy reconstruction of KASCADE-Grande (20 %) and from the calibration source (16 %), see section 6.1.

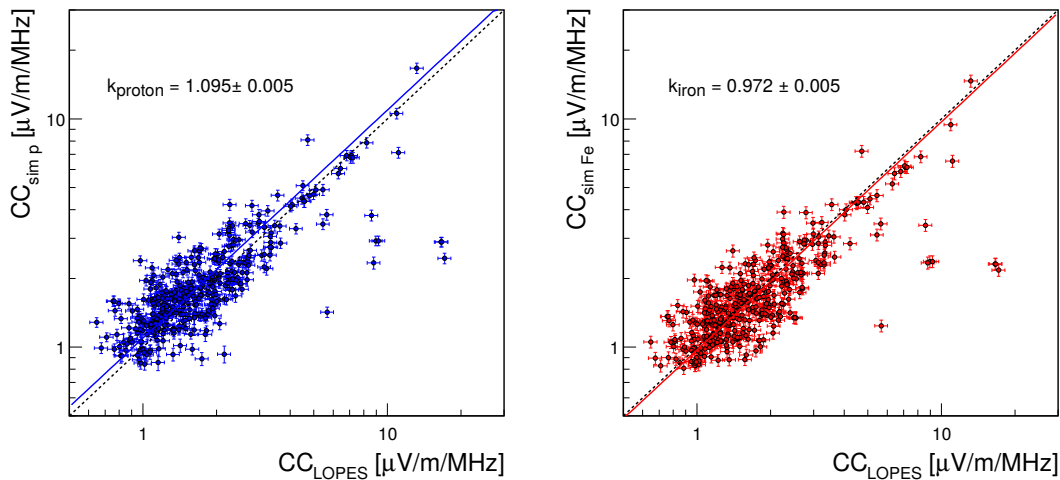


**Figure 6.9:** Per-event comparison of the measured and simulated amplitude of the CC-beam. Left for proton and right for iron primary particles. The dashed line indicates unity while the solid line is a linear fit to the data points with the fitted slope  $k$ .

But as already visible by eye and confirmed by a reduced  $\chi^2$  of almost 10 the statistical uncertainty of 6 %, obtained from the influence of noise (section 4.2), seems to be significantly underestimated. Assuming that the simulations predict a correct CC-beam amplitude, a statistical uncertainty in the order of 20 % for both, data and simulations, is required to explain the observed scatter. As discussed in section 6.1, formerly the only available uncertainty on the CC-beam amplitude was derived from the Gaussian fit. With the detector simulation it was possible to determine an additional statistical uncertainty from the influence of noise. It seems that the true statistical uncertainty

for both, data and simulations is higher and in the same order as for the amplitude parameter  $\epsilon_{100}$ . For future analysis a statistical uncertainty of the CC-beam of 20 % is assumed for data and for simulations including noise.

From figure 6.10 an overestimation of the amplitude for proton simulations of 10 % and a slight underestimation for iron simulations of 0.2 % is determined. Such a systematic shift is clearly covered by the systematic uncertainty of the calibration source (16 % on data) and of the energy reconstruction by KASCADE-Grande (20 % on simulations). As expected, the width of the distribution is comparable to the one obtained for  $\epsilon_{100}$  as both are a measure for the amplitude. The total difference between proton and iron is around 10 % for both, the CC-beam amplitude and the lateral amplitude whereas the observed absolute shifts differ: For  $\epsilon_{100}$  an overestimation for proton and an underestimation for iron of 5 % was observed. This difference is still below the statistical uncertainties of 20 % for the CC-beam amplitude and 10 % for the lateral amplitude  $\epsilon_{100}$ .

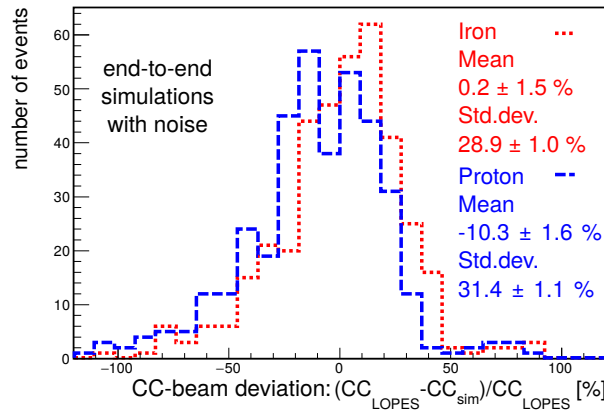
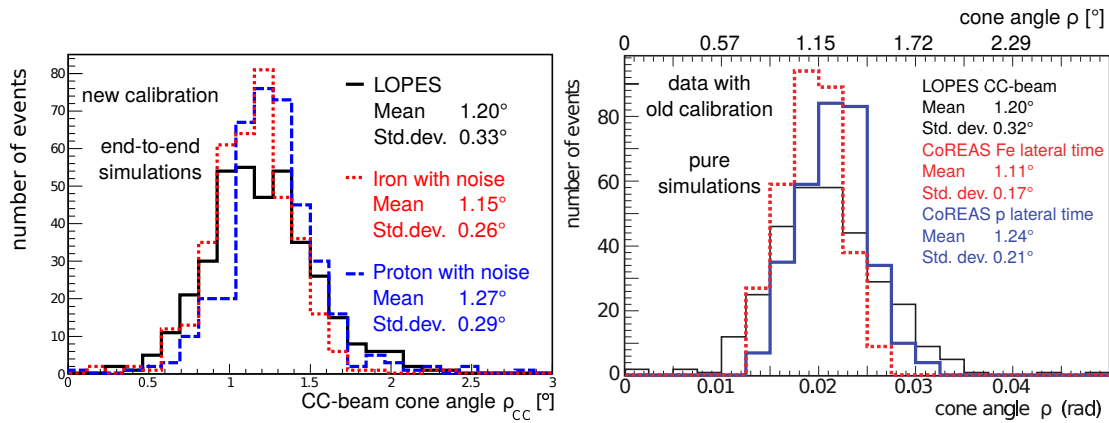


Figure 6.10: Relative deviation of the measured and simulated amplitude of the CC-beam.

### Cone angle

Beside the amplitude also the wavefront is reconstructed during the interferometric analysis and the cone angle is calculated. Since the cone angle is sensitive to the shower maximum only a statistical comparison is performed and no per-event comparison. A per-event comparison suffers on the high shower to shower fluctuations. This means that the simulation of a particular event does not necessarily have the same shower maximum as the measured event.

The average cone angle  $\rho_{CC}$  of LOPES data is  $1.20^\circ \pm 0.02^\circ$  which is in between the values obtained for proton with  $1.27^\circ \pm 0.01^\circ$  and iron with  $1.15^\circ \pm 0.01^\circ$ , see figure 6.11 (left). For the first time the cone angle of data and simulations obtained with the same method are compared and a very good agreement is found. It is notable that these values are also in good agreement with former published results using pure simulations which are  $1.24^\circ$  for proton and  $1.11^\circ$  for iron while for the measurement the values are identical, see figure 6.11 (right) (Apel et al., 2014b). In this earlier publication the values for the simulations did not include noise and were derived using a fit to the lateral



**Figure 6.11:** Left: Distribution of the cone angle  $\rho_{CC}$  reconstructed by hyperbolic beamforming for measured and simulated events. Right: Former results as published in Apel et al. (2014b). Distribution of the cone angle  $\rho_{CC}$  reconstructed by hyperbolic beamforming for measured events and the cone angle  $\rho$  derived by a fit to the lateral time distribution for simulated events.

time distribution. For the published results the cone angle for measurements was derived using the beamforming method and the old calibration values. The width of the distribution for the simulations is difficult to compare. The different reconstruction methods have different uncertainties and the inclusion of noise leads to additional statistical uncertainties for the cone angle which mainly explains the larger width of  $0.26^\circ$  and  $0.29^\circ$  for iron- and proton-induced end-to-end simulations, respectively.

### 6.2.3 Conclusion

With the revised amplitude calibration, the LOPES measurements show good agreement with state-of-the-art CoREAS simulations. Regarding the high measurement uncertainties of the pioneering LOPES experiment, the achieved agreement of data and CoREAS simulations is remarkable.

Using the lateral distribution, a per-event comparison is done for the amplitude while for the mass sensitive parameters only a statistical comparison is performed. Within uncertainties the simulated and measured lateral distributions are compatible. A per-event comparison of data and simulations for the slope and cone angle could be performed by radio experiments connected with detectors that provide a good measurement of the shower maximum, like Tunka-Rex with the Cherenkov detectors or AERA with the fluorescence telescopes (Bezyazeev et al., 2016; Kostunin et al., 2016; Gaté et al., 2016).

For the first time also a comparison based on interferometric analysis of simulations was possible and for both the amplitude and the reconstructed cone angle a good agreement was found.

### 6.3 Reconstruction of arrival direction

After establishing a good agreement of data and simulations in the previous section, in this and the following sections the reconstruction of the air shower parameters arrival direction, energy and shower maximum are investigated using the improved analysis. All these investigations are done for both LOPES data and CoREAS end-to-end simulations.

The reconstruction of the arrival direction with the LOPES data is performed within the interferometric analysis using a hyperbolic wavefront. The CC-beam is calculated for different arrival directions in the sky and iteratively maximized. As starting point the arrival direction provided by KASCADE-Grande is used. Former investigations showed that this induces no bias on the reconstruction accuracy, see Lapp (2013). In figure 6.12 the deviation between the arrival directions given by KASCADE(-Grande) and reconstructed with LOPES is shown, on the left only for KASCADE-triggered events and on the right for both, KASCADE- and KASCADE-Grande-triggered events. The variable binning is chosen in such a way, that the phase space covered by each bin is constant. A combined LOPES and KASCADE angular resolution of  $0.52 \pm 0.02^\circ$  and a combined LOPES and KASCADE(-Grande) resolution of  $0.53 \pm 0.01^\circ$  is observed. The angular resolution of KASCADE-Grande is not exactly known but should be below  $0.5^\circ$ .

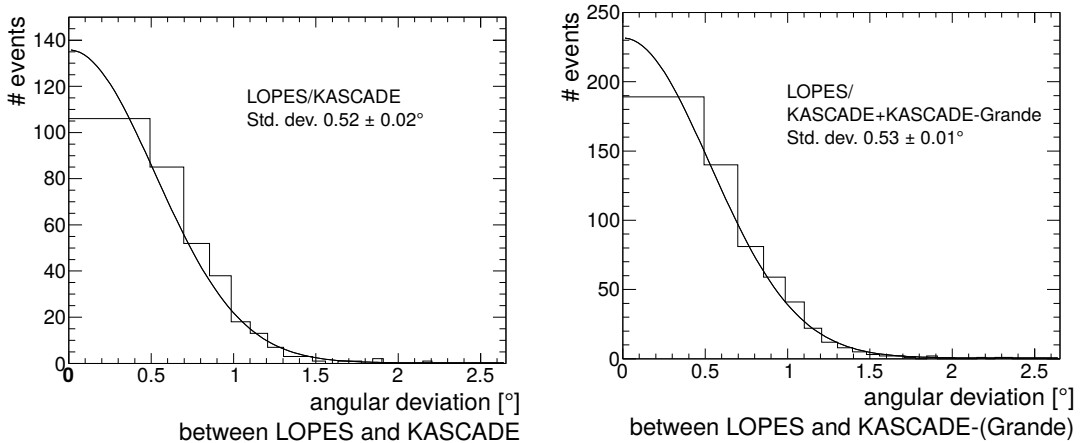


**Figure 6.12:** Angular deviation between the arrival direction given by KASCADE-Grande and the arrival direction reconstructed within the interferometric analysis of LOPES data. On the left only for events inside the KASCADE array and on the right for events inside KASCADE and KASCADE-Grande. The variable binning accounts for a constant phase space in each bin.

In former publications (Apel et al., 2014b, 2016) no variable but a constant binning was chosen which results in an increasing phase space for increasing bins and therefore the stated angular resolution is worse than the actually achieved one. Figure 6.13 shows the former published results on the right and on the left the results obtained with the improved analysis for comparison also using a constant binning. As expected the calculated resolution is worse than the one obtained with the variable binning but the resolution for the improved analysis of  $0.64 \pm 0.02^\circ$  is compatible within uncertainties with the former published resolution of  $0.65 \pm 0.02^\circ$ .

For investigations independent of the KASCADE-Grande angular resolution CoREAS simulations are used. With these also the influence of noise on the angular resolution

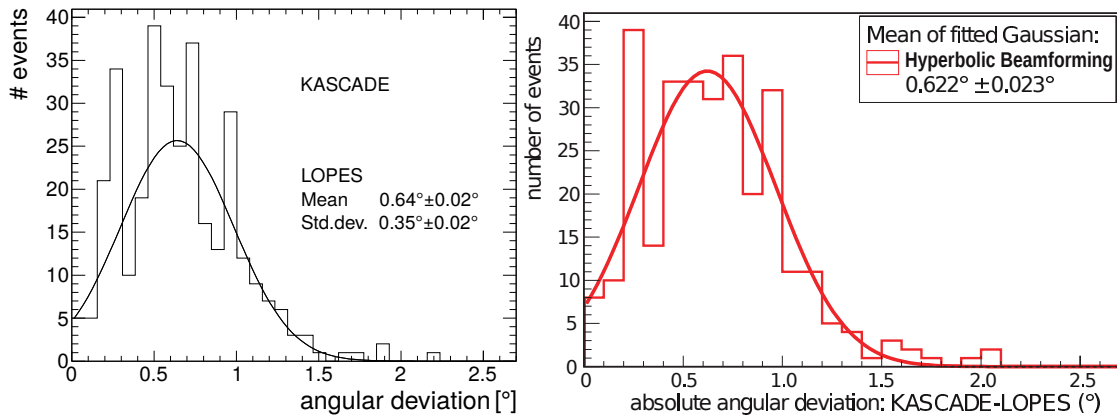


**Figure 6.13:** Angular deviation between the arrival direction given by KASCADE and the arrival direction reconstructed by the interferometric beamforming within the analysis pipeline of LOPES for hyperbolic beamforming. On the left using the improved analysis pipeline and on the right former results as published in Apel et al. (2014b).

can be studied. Figure 6.14 shows the angular difference between the interferometrically reconstructed and the true arrival direction, once for events including noise and once without noise. Here the end-to-end CoREAS simulations are used including all detector effects and the simplified reconstruction. The intrinsic angular resolution is around  $0.05^\circ$  for the simulations without noise. The additional noise increases the angular difference by only  $0.02^\circ$  for proton and  $0.01^\circ$  for iron primaries. The very good angular resolution of only  $0.06 - 0.07^\circ$  for the method itself including noise implies that the combined resolution achieved with the LOPES measurements of  $\sim 0.5^\circ$  is by far dominated by the angular resolution of KASCADE-Grande.

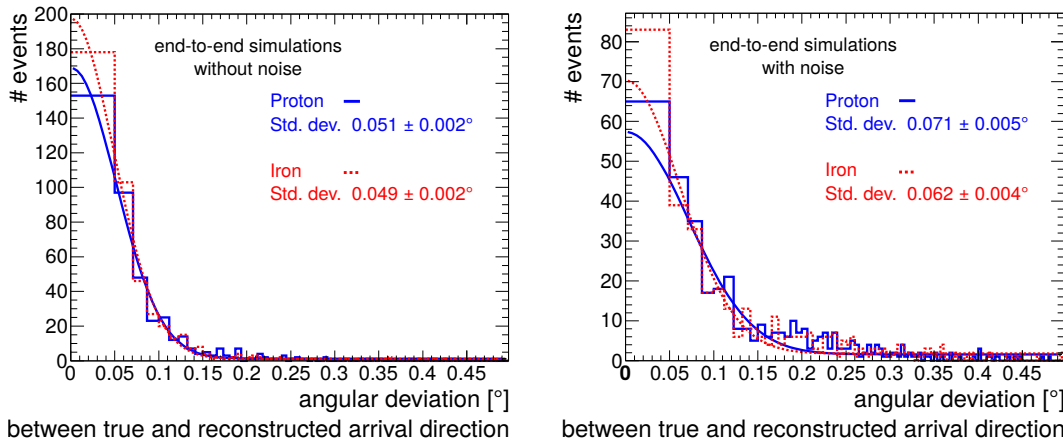


**Figure 6.14:** Angular deviation between the true arrival direction and the arrival direction reconstructed by the interferometric beamforming within the analysis pipeline of LOPES applied to simulations.

## 6.4 Reconstruction of the cosmic-ray energy

Beside the arrival direction also the energy of the primary particle can be reconstructed using LOPES measurements. In this work two approaches are discussed, one uses the amplitude of the CC-beam and one is based on the amplitude at a characteristic axis distance determined from the lateral distribution.

### 6.4.1 Based on CC-beam

An energy reconstruction based on the CC-beam amplitude was at first presented in Horneffer et al. (2007) with a small data set and with the full data set in Schröder et al. (2013) where a combined energy resolution better than 20 % for KASCADE and LOPES and 26 % for KASCADE-Grande and LOPES was reported. The same analysis is repeated here using the improved analysis for data and for the first time also using end-to-end simulations.

In principle a reconstruction of the energy should be based on the complete electric field vector, but only the east-west component is available in LOPES data. The main contribution of the radio signal is determined by the Lorentz force of the Earth's magnetic field. The east-west component is therefore normalized to the fraction of amplitude expected for the individual shower direction in the east-west component  $P_{EW} = |\vec{v} \times \vec{B}|_{EW}$  by the geomagnetic Lorentz force. Furthermore the signal is normalized to the mean distance of all antennas  $d_{mean}$  using an exponential function, and only the LOPES bandwidth is considered. Formula 6.2 shows the exact calculation, adopted from Schröder et al. (2013). As normalization distance the average mean distance of KASCADE-Grande events, which is 180 m, was chosen.

$$CC_{norm} = \frac{CC}{P_{EW} \cdot \exp(-d_{mean}/180 \text{ m})} \quad (6.2)$$

$$E_{LOPES} = c \cdot CC_{norm} \quad (6.3)$$

A cross-calibration of the energy  $E_{LOPES}$  reconstructed via the normalized CC-beam amplitude  $CC_{norm}$  and the energy given by KASCADE and KASCADE-Grande, respectively, is performed. A linear correlation between the energy and the amplitude is assumed because of the coherence of the radio signal.

The proportionality factor  $c$  in formula 6.3 is determined in such a way that the mean relative deviation between the reconstructed energy  $E_{LOPES}$  and the one from KASCADE(-Grande) is zero. Therefore the calibration values are increased step-by-step and for each, the relative difference between LOPES and KASCADE(-Grande) reconstructed energies is determined. Then the range of calibration values where the relative difference is, within uncertainties, equal to zero is identified. From this range of calibration values the mean value is chosen as proportionality factor which results in  $c_K = 45.5 \pm 0.8 \text{ PeV}/(\mu\text{V}/\text{m}/\text{MHz})$  for KASCADE and  $c_{KG} = 32.7 \pm 0.9 \text{ PeV}/(\mu\text{V}/\text{m}/\text{MHz})$  for KASCADE-Grande, see also table 6.3. The range of the calibration values, for which the relative energy difference is zero, is used as uncertainty of the correlation factors.

A per-event comparison of the energy reconstructed by LOPES and the energy given by KASCADE(-Grande) is shown in the upper row of figure 6.15. The error bars are the statistical errors of 20 % as determined in section 6.2.2. For the KASCADE events

a deviation from the linear correlation for high energies is visible. This was already observed earlier (Schröder et al., 2013) and is probably due to the fact that the energy reconstruction used for KASCADE events is not optimized for this energy range. The distribution of the relative deviation is shown in figure 6.15, lower row. Since the mean deviation of this distribution is zero by construction, the energy resolution is determined by the standard deviation. The combined KASCADE-(Grande) and LOPES energy resolution is  $21.5 \pm 1.3\%$  for KASCADE and  $24.3 \pm 1.7\%$  for KASCADE-Grande. Within the uncertainty these resolutions are compatible with the previously reported ones, see figure 6.16 and table 6.3. The proportionality factor of course is different. For KASCADE events it is 2.68 times higher and for KASCADE-Grande 2.52 times higher than before the improved analysis which matches the expectations from the updated amplitude calibration.

In the publication Schröder et al. (2013) two possible reasons for the different proportionality factors for KASCADE and KASCADE-Grande are given: First the energy reconstruction for KASCADE is not designed for the energy range measured by

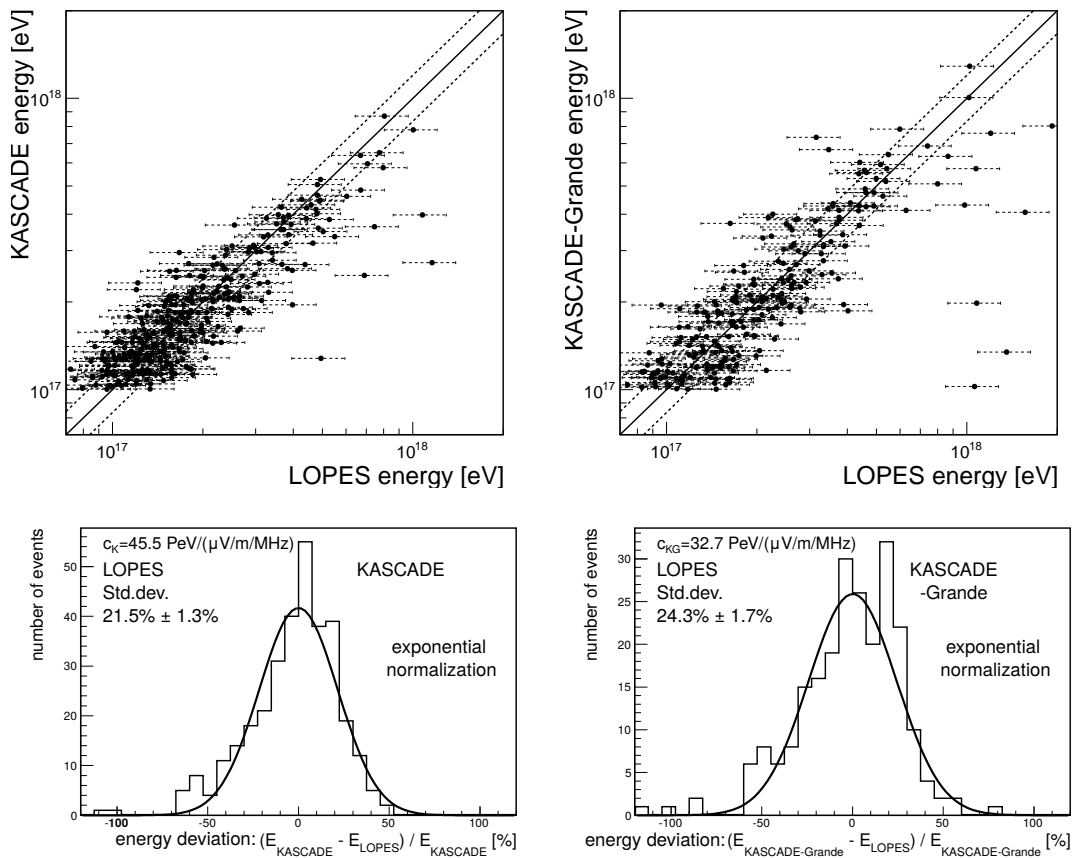


**Figure 6.15:** Upper row: Per-event comparison of the KASCADE(-Grande) energy and the energy reconstructed with LOPES. The solid line indicates identity and the dashed lines indicate the 20 % scale uncertainty. Lower row: Distribution of the relative deviation between KASCADE(-Grande) and LOPES energies. On the left for events inside the KASCADE array and on the right for those inside the KASCADE-Grande array.

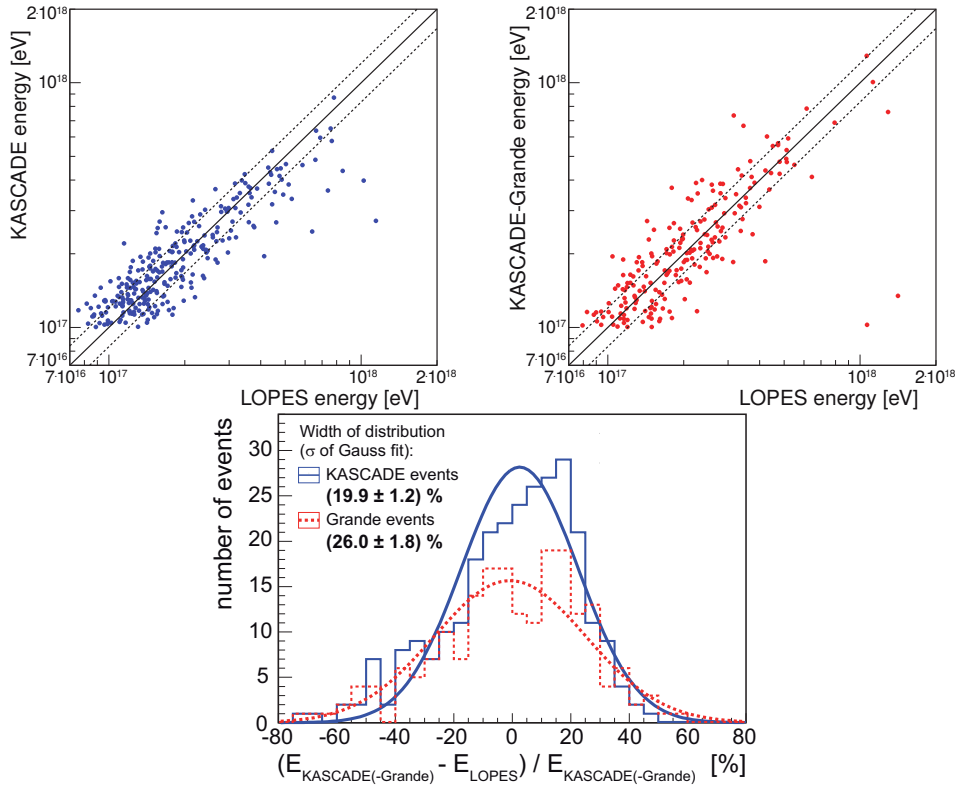


**Figure 6.16:** Former results as published in Schröder et al. (2013). Upper row: Per-event comparison of the KASCADE(-Grande) energy and the energy reconstructed with LOPES. For KASCADE events the LOPES energy is reconstructed using  $c_K = 17 \text{ PeV}/(\mu\text{V}/\text{m}/\text{MHz})$  while for KASCADE-Grande  $c_{KG} = 13 \text{ PeV}/(\mu\text{V}/\text{m}/\text{MHz})$  is used. Lower row: Distribution of the relative deviation between KASCADE(-Grande) and LOPES energies.

LOPES and second the mean distance of the shower core to the antennas is higher for KASCADE-Grande. In principle a normalization for the distance is done but the used exponential dependence might be insufficient, in particular since it is known that the true lateral distribution is better described by a Gaussian function.

For simulations the true input energy is known and therefore a dependence on the energy reconstruction accuracy of KASCADE(-Grande) vanishes. Using the simulations allows to further investigate the reasons for the difference between KASCADE and KASCADE-Grande. Furthermore, with the end-to-end simulations including measured noise the LOPES-only energy resolution can be determined and the method-only resolution is calculated with the end-to-end simulations without noise.

The same procedure as applied to data is therefore also performed for end-to-end simulations with and without noise. The resulting plots are shown in figure 6.17 for simulations with noise and in figure 6.18 for simulations without noise. The derived proportionality factors and resolutions are listed in table 6.3.

The correlation factors of the measurements are slightly different than those from the simulations. Compared to the mean values of proton and iron for simulations including noise the correlation factor of the measurements are  $\sim 9\%$  higher for KASCADE events and  $\sim 11\%$  lower for KASCADE-Grande events. This implies that the energy reconstructed by KASCADE underestimates the true energy while the energy reconstructed

**Table 6.3:** Correlation factor  $c$  between KASCADE(-Grande) energy and reconstructed LOPES energy using the exponential-normalized CC-beam and the resulting resolutions. For the end-to-end simulations the KASCADE(-Grande) energy is the true energy.

		KASCADE		KASCADE-Grande	
		correlation $c$ [PeV/( $\mu$ V/m/MHz)]	resolution [%]	correlation $c$ [PeV/( $\mu$ V/m/MHz)]	resolution [%]
LOPES, new calibration		$45.5 \pm 0.8$	$21.5 \pm 1.3$	$32.7 \pm 0.9$	$24.3 \pm 1.7$
LOPES, old calibration		17	20	13	26
end-to-end simulations with noise	p	$39.4 \pm 0.3$	$12.5 \pm 0.6$	$35.1 \pm 0.4$	$14.9 \pm 1.4$
	Fe	$44.3 \pm 0.4$	$12.2 \pm 0.6$	$38.2 \pm 0.6$	$13.8 \pm 1.2$
end-to-end simulations without noise	p	$40.4 \pm 0.2$	$11.6 \pm 0.5$	$36.2 \pm 0.6$	$13.1 \pm 0.9$
	Fe	$45.3 \pm 0.3$	$11.0 \pm 0.6$	$39.2 \pm 0.3$	$11.7 \pm 0.9$

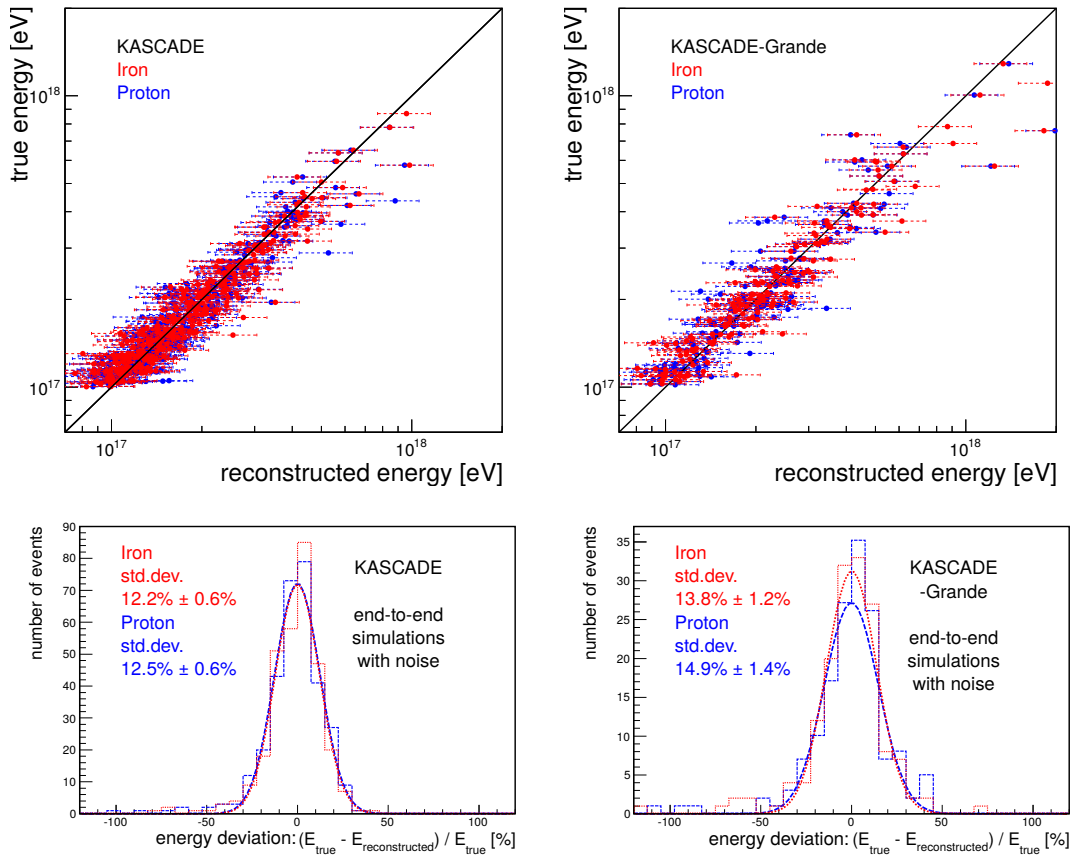


**Figure 6.17:** Upper row: Per-event comparison of the true and reconstructed energy for events simulated with CoREAS for both, iron and proton initiated shower including noise. On the left for events inside the KASCADE array and on the right for those inside the KASCADE-Grande array. The line indicates identity. Lower row: Distribution of the relative deviation between true and reconstructed energies.

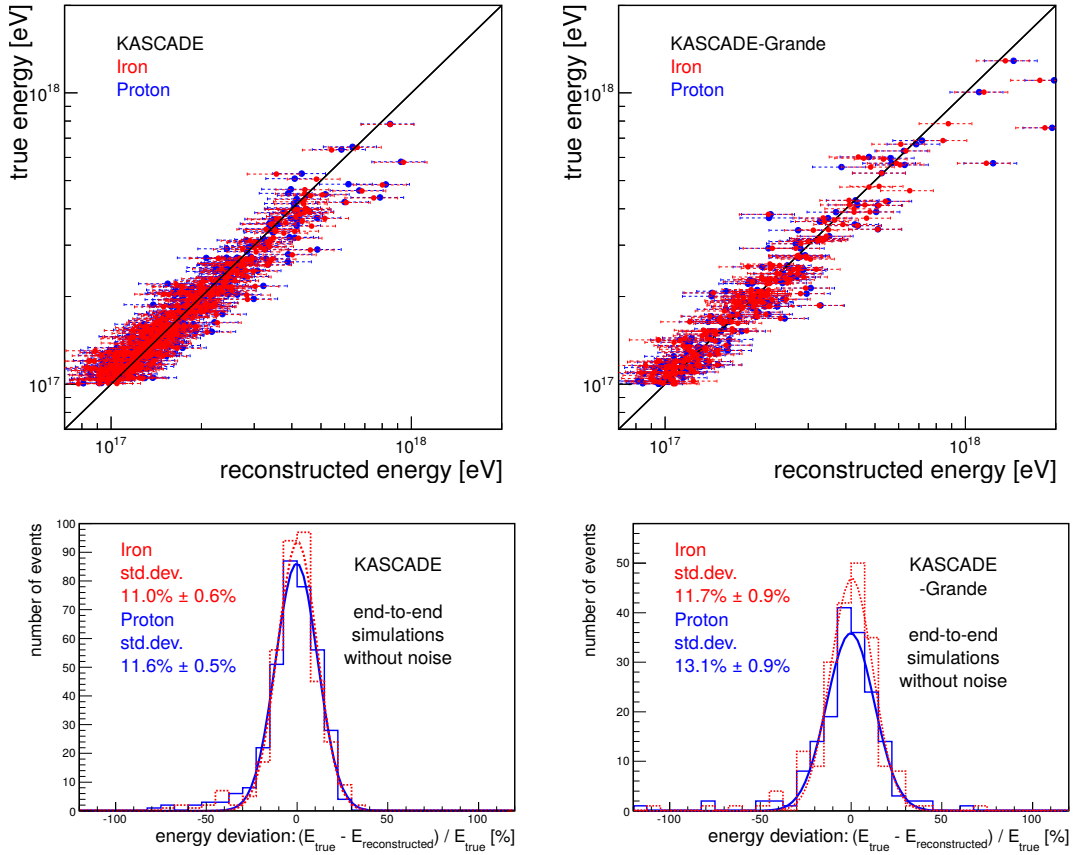


**Figure 6.18:** Upper row: Per-event comparison of the true and reconstructed energy for events simulated with CoREAS for both, iron and proton initiated shower without noise. On the left for events inside the KASCADE array and on the right for those inside the KASCADE-Grande array. The line indicates identity. Lower row: Distribution of the relative deviation between true and reconstructed energies.

by KASCADE-Grande overestimates it. Which is probably due to the fact that the applied energy formula as used for LOPES is not designed for the measured energies. But still the difference is below the energy uncertainty provided by KASCADE(-Grande) of 20%.

For the simulated events still a difference in the proportionality factor between KASCADE and KASCADE-Grande occurs but less distinct. This implies that the difference between KASCADE and KASCADE-Grande is caused by both effects, the energy reconstruction method which is not optimized for the used energy range and the higher mean distances of KASCADE-Grande events which is discussed later.

The difference in the proportionality factors for proton and iron primaries hint to a dependence of the CC-beam amplitude on the mass of the primary particle. In principle the CC-beam amplitude combined with a measurement of the number of muons in the air shower should provide information on the primary mass: Radio measurements are only sensitive to the electromagnetic component and its corresponding electromagnetic energy. Depending on the type of the primary particle the ratio of the electromagnetic and muonic component changes and this ratio yields information on the primary mass.

To minimize the influence of the primary particle for the energy reconstruction a different method based on a different parameter, e.g. the amplitude of the lateral distribution at a certain distance, is possible, see section 6.4.2.

The energy resolution derived for the simulations range from 12 % to 15 % for events including noise and from 11 % to 13 % for events without noise. A LOPES-only energy resolution of less than 15 % can therefore be achieved with the presented procedure with an intrinsic resolution for the method itself of  $\sim 12\%$ .

The achieved resolution is almost independent of the simulated primary particle and is compatible within uncertainties for the iron and proton simulation sets. But, as for the proportionality factors, also in the achieved resolution a difference between KASCADE and KASCADE-Grande is visible. An insufficient normalization of the lateral dependence (see formula 6.2) can explain the higher scatter for the events measured with KASCADE-Grande. Figure 6.19, on the left, shows the ratio of the true and reconstructed energy for the KASCADE-Grande iron simulations as a function of the mean lateral distance using an exponential distance normalization like in formula 6.2. For events with a mean lateral distance around 180 m, which is the reference value for which the correction is applied, the ratio is close to one while for closer and further distances the reconstructed energy gets too high.

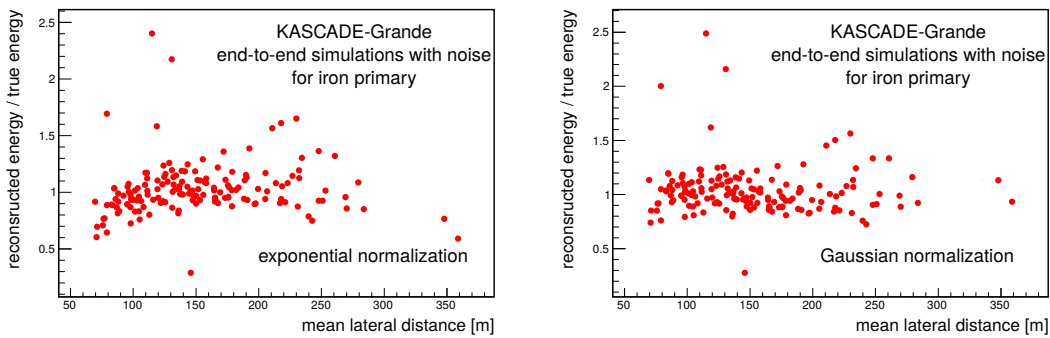


**Figure 6.19:** Ratio of the true and reconstructed energy as a function of the mean lateral distance of the shower to the antennas for CoREAS simulated KASCADE-Grande events. On the left for an exponential normalization and on the right for a Gaussian normalization.

### Gaussian distance normalization

To improve the energy reconstruction, a different distance normalization based on a Gaussian function was tested. The normalized CC-beam amplitude was calculated like:

$$CC_{norm} = \frac{CC}{P_{EW} \cdot \exp((d_{mean} - a)^2 / 2 \cdot b^2)}, \quad (6.4)$$

with  $a=50$  m and  $b=160$  m.

The parameter  $a$  is chosen in such a way that for KASCADE events, which mostly have a mean axis distance of 50 m, no correction is applied. For  $b$  a scan of different values was performed, and for  $b=160$  m the smallest dependence on the deviation between reconstructed and true energy was found, see figure 6.19 on the right.

Using formula 6.4 the same procedure as before was applied to LOPES data. The resulting correlation values are  $71.5 \pm 1.9 \text{ PeV}/(\mu\text{V}/\text{m}/\text{MHz})$  for KASCADE and  $59.5 \pm 2.1 \text{ PeV}/(\mu\text{V}/\text{m}/\text{MHz})$  for KASCADE-Grande while the achieved resolutions are  $23.1 \pm 1.3$  for KASCADE and  $23.0 \pm 1.4$  for KASCADE-Grande, see figure 6.20. The difference in the correlation factors for KASCADE and KASCADE-Grande are due to the slightly different energy reconstruction. Within uncertainties the resolutions are still compatible with those achieved for the exponential distance normalization, but now, with the Gaussian distance normalization, no difference in the resolution of KASCADE and KASCADE-Grande is observed. Anyhow the achieved resolution for the energy reconstruction does not significantly improve. This result also supports that it is valid to use an exponential function to describe the lateral distribution, at least for the LOPES experiment.

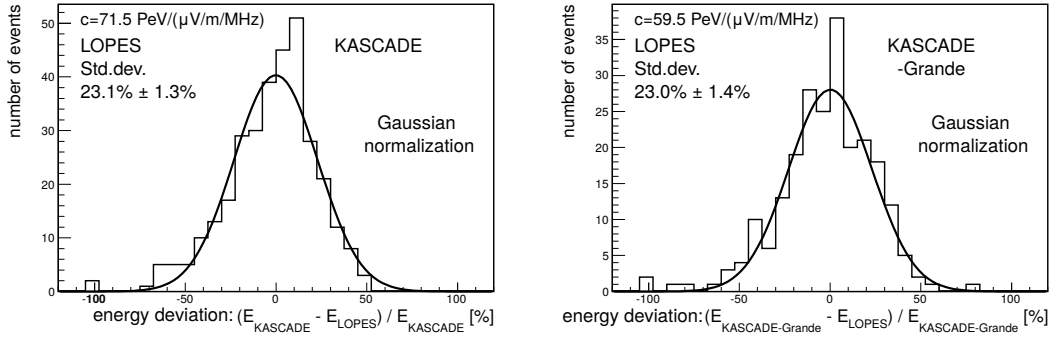


Figure 6.20: Distribution of the relative deviation between the reconstructed energy of KASCADE(-Grande) and LOPES for a Gaussian distance normalization.

#### 6.4.2 Based on the amplitude at a certain lateral distance

The same approach for the reconstruction of the energy as applied to the CC-beam amplitude is also applied to the amplitude of the lateral distribution. The fitted amplitude at 100 m distance,  $\epsilon_{100}$ , is normalized to the amplitude fraction  $P_{EW}$  from the Lorentz force, like also done in Schröder et al. (2013b), and then the LOPES energy is calculated like:

$$E_{\text{LOPES}} = k \cdot \frac{\epsilon_{100}}{P_{EW}} \quad (6.5)$$

The correlation factor  $k$  is determined as for the CC-beam reconstruction, which means, that the relative difference between LOPES and KASCADE(-Grande) reconstructed energy is zero. The combined energy resolution is given by the standard deviation of the relative difference between LOPES and KASCADE(-Grande), and the LOPES- and method-only resolution can be determined using the end-to-end simulations. The resulting correlation plots and the energy deviations are shown in figures 6.21 – 6.23 and the determined correlation factors and the resolutions are given in table 6.4. The principle results are comparable with those obtained from the energy reconstruction based on the CC-beam.

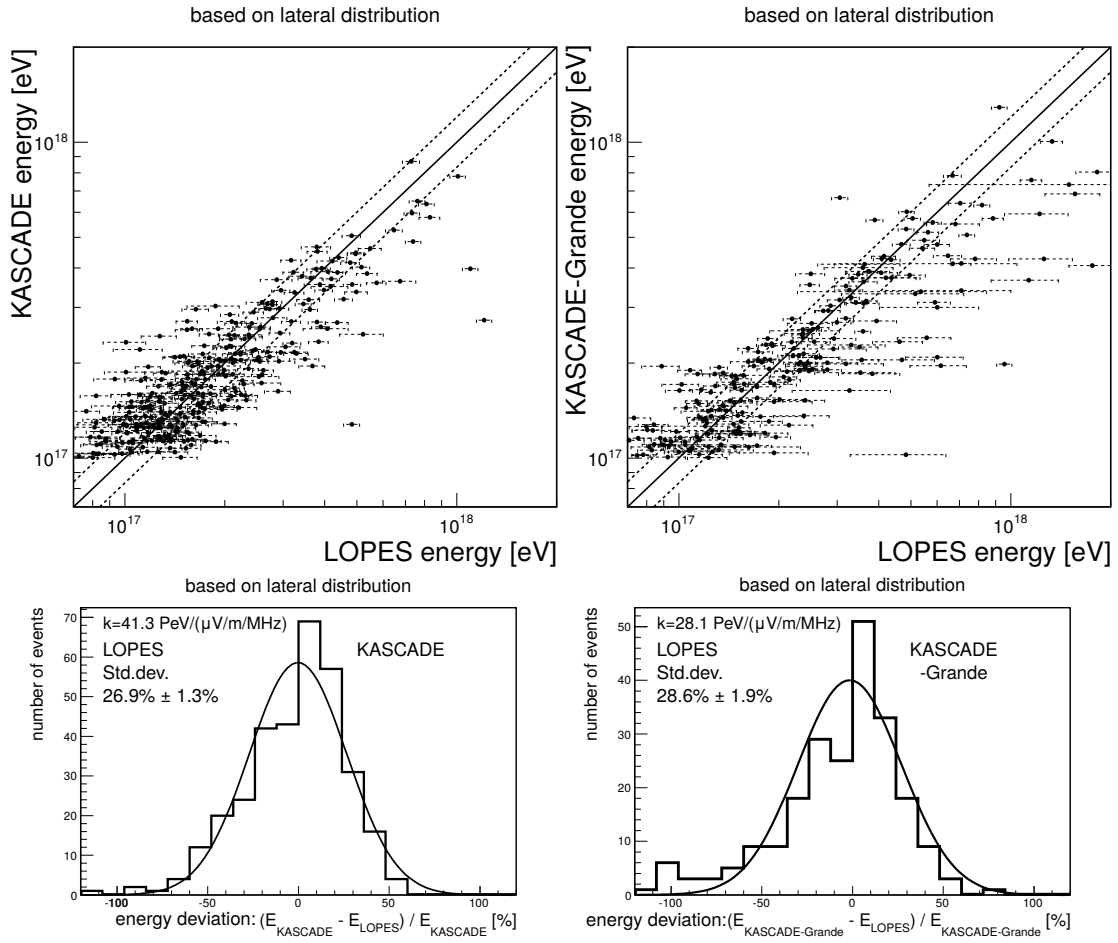


Figure 6.21: Upper row: Per-event comparison of the KASCADE(-Grande) and LOPES energy reconstructed from the lateral amplitude  $\epsilon_{100}$ . On the left for events inside the KASCADE array and on the right for those inside the KASCADE-Grande array. The solid line indicates identity while the dashed lines represent the 20% energy uncertainty from KASCADE(-Grande). Lower row: Distribution of the relative deviation between KASCADE(-Grande) and LOPES energies.

Table 6.4: Correlation factor  $k$  between KASCADE(-Grande) energy and reconstructed LOPES energy using the lateral amplitude  $\epsilon_{100}$  and the resulting resolutions. For the end-to-end simulations the KASCADE(-Grande) energy is the true energy.

	KASCADE		KASCADE-Grande	
	correlation $k$ [PeV/( $\mu$ V/m/MHz)]	resolution [%]	correlation $k$ [PeV/( $\mu$ V/m/MHz)]	resolution [%]
LOPES, new calibration	$41.3 \pm 0.5$	$26.9 \pm 1.3$	$28.1 \pm 0.8$	$28.6 \pm 1.9$
end-to-end simulations with noise	p $37.2 \pm 0.2$	$14.1 \pm 0.7$	$32.5 \pm 0.6$	$12.0 \pm 0.7$
	Fe $40.9 \pm 0.3$	$13.0 \pm 0.7$	$36.5 \pm 0.5$	$14.5 \pm 0.9$
end-to-end simulations without noise	p $37.8 \pm 0.2$	$12.0 \pm 0.6$	$30.5 \pm 1.0$	$14.3 \pm 1.7$
	Fe $41.9 \pm 0.3$	$10.4 \pm 0.4$	$33.7 \pm 0.6$	$17.5 \pm 1.2$

It is noticeable that for most cases the resolutions achieved from the lateral reconstruction are worse than those using the CC-beam. The main difference is observed for the KASCADE-Grande events simulated without noise which somehow break ranks. From the reconstruction based on the CC-beam the correlation factors were expected to get higher while the resolution should get better compared to the simulations without noise. The reason for this different behaviour is not understood.

The overall worse resolution is caused by the simple reconstruction approach. For a more precise reconstruction not  $\epsilon_{100}$  should be considered but the amplitude  $\epsilon_{d_0}$  at a distance  $d_0$  with the minimal dependence on the primary particle. This distance can also change for different zenith angles of the incoming shower as observed in Apel et al. (2014a). There the energy reconstruction is based on the amplitude at  $d_0$  derived from a Gaussian fit of the lateral distribution.

Such a Gaussian fit was not done in the scope of this work and also not such a sophisticated energy reconstruction. But in the next paragraph the expected influence of the improved analysis for the results presented in Apel et al. (2014a) is discussed.

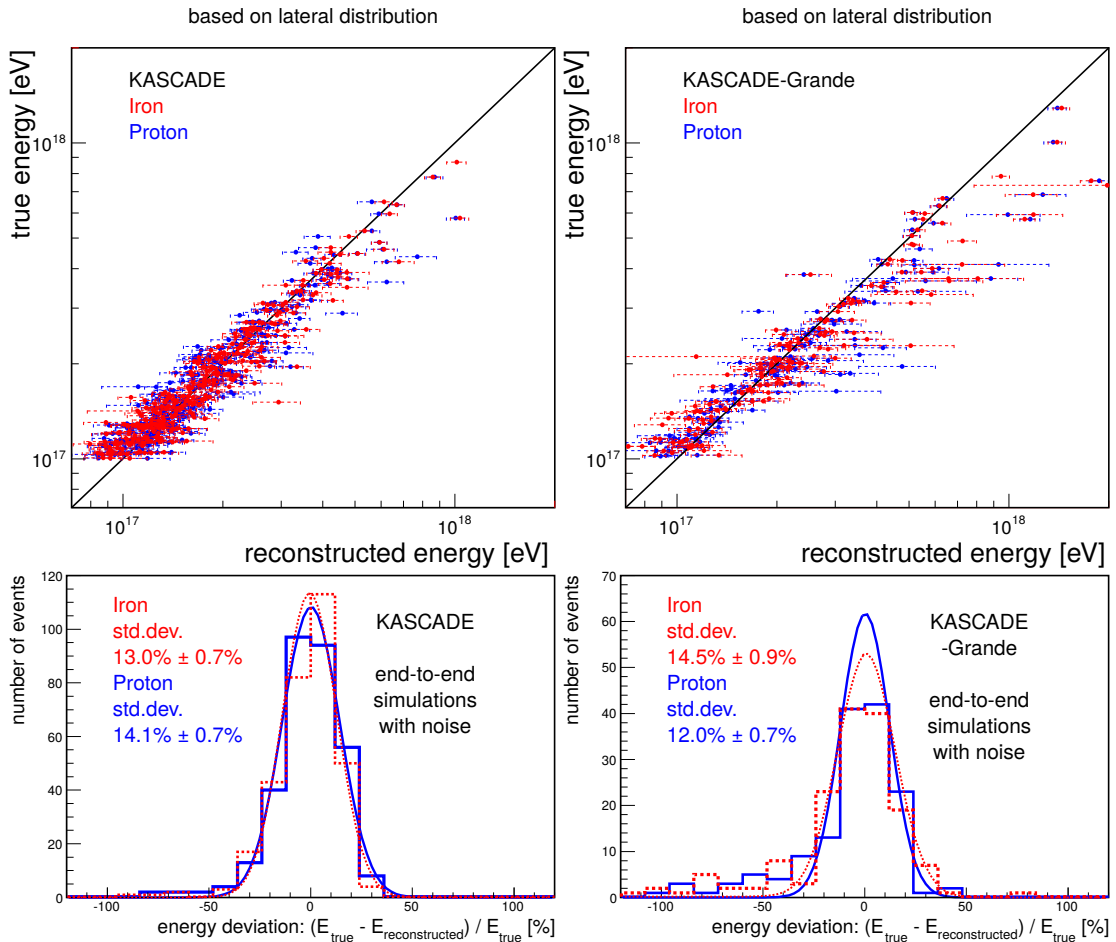


Figure 6.22: Upper row: Per-event comparison of the true energy and the energy reconstructed from the lateral amplitude  $\epsilon_{100}$  for events simulated with CoREAS for both, iron and proton initiated shower, including noise. On the left for events inside the KASCADE array and on the right for those inside the KASCADE-Grande array. The line indicates identity. Lower row: Distribution of the relative deviation between true and reconstructed energies.

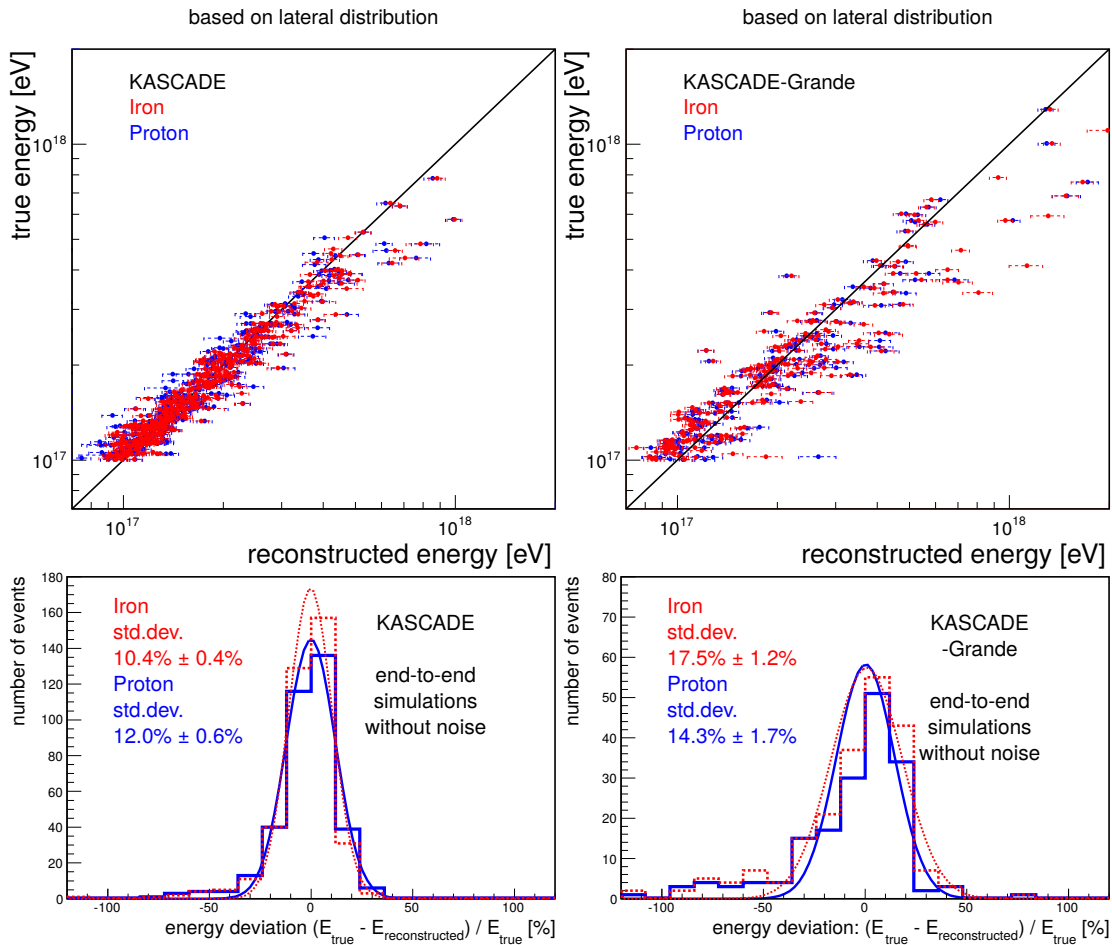


Figure 6.23: Upper row: Per-event comparison of the true energy and the energy reconstructed from the lateral amplitude  $\epsilon_{100}$  for events simulated with CoREAS for both, iron and proton initiated shower, without noise. On the left for events inside the KASCADE array and on the right for those inside the KASCADE-Grande array. The line indicates identity. Lower row: Distribution of the relative deviation between true and reconstructed energies.

### Energy reconstruction based on a Gaussian lateral distribution

In Apel et al. (2014a), for the energy reconstruction the amplitude of the Gaussian fit at a particular distance  $d_0$ , which depends minimally on the primary mass, is determined. This amplitude is correlated with the primary energy once for data and once for CoREAS simulations. The distance  $d_0$  is evaluated separately for different zenith angles and varied from 70 m to 100 m. The influence of the improved analysis on the amplitude at  $d_0$  is expected to be comparable with the influence on the amplitude parameter  $\epsilon_{100}$ . In section 4.4 it was shown that the amplitude  $\epsilon_{100}$  derived for pure simulations is the same as the one derived for the end-to-end simulations including the detector simulation and noise. This implies that also the correlation factor between the amplitude and the energy derived for simulations should not change. Due to the updated amplitude calibration a change of the measured amplitude by a factor of 2.6 is expected as shown in section 5.6. Therefore the correlation factor (i.e. the slope) for

data should increase by a factor of 2.6.

The published correlation factors for simulations increase from  $29,9 \text{ PeV}/(\mu\text{V}/\text{m}/\text{MHz})$  to  $39.8 \text{ PeV}/(\mu\text{V}/\text{m}/\text{MHz})$  with increasing zenith angle. For data no clear zenith dependence was observed with correlation factors varying between  $13.4 \text{ PeV}/(\mu\text{V}/\text{m}/\text{MHz})$  and  $15.1 \text{ PeV}/(\mu\text{V}/\text{m}/\text{MHz})$ . Multiplying the published correlation factors for data by 2.6 results on average in comparable slopes for data and simulations. For individual zenith angles there is a difference related to the zenith dependence observed in the ratio of measured and simulated amplitudes which is still apparent for the improved analysis, see figure 6.8.

The achieved energy resolution is expected to be still valid. A combined LOPES and KASCADE energy resolution of 20-25 % and an intrinsic energy resolution of less than 10 % for the presented method was reported in Apel et al. (2014a), depending on the zenith angle. An energy reconstruction for KASCADE-Grande was not performed. Hence, these resolutions are better than those achieved for the simple reconstruction approach based on the lateral amplitude at 100 m  $\epsilon_{100}$ .

### 6.4.3 Comparing energy scales of KASCADE-Grande and Tunka-133

In Hiller et al. (2016) a comparison of the energy scales of the particle detector KASCADE-Grande and the Cherenkov detector Tunka-133 via their radio extensions LOPES and Tunka-Rex is presented. Based on the improved analysis, as developed in this work, the LOPES measurements were reconstructed and, beside rescaled simulations, provided for this joint analysis. A short description of the applied comparison methods and their results are shown in this section.

The energy spectra for cosmic rays derived by KASCADE-Grande and Tunka-Rex as presented in Apel et al. (2012b) and Prosin et al. (2014) are based on two totally different measurement techniques. But both experiments are a host for a radio extension. Since radio measurements provide a high sensitivity on energy a comparison of the two different energy scales is possible. The comparison is based on events measured by the radio extensions Tunka-Rex and LOPES. The main advantage of using these experiments is the common amplitude calibration using the same external calibration source. This reduces the scale uncertainty to only 7 %. To account for the zenith dependence of the LOPES amplitude, which is probably caused by an insufficient simulation of the antenna gain pattern, an additional uncertainty of 10 % is assumed. This value is determined from the mean deviation between LOPES data and simulations, see figure 6.8 and section 6.2.1.

Two different approaches are presented, one is based on a radio energy estimator, which is the amplitude and one is based on CoREAS simulations.

For the first approach, the normalized amplitude at 100 m distance is calculated using an exponential fit of the lateral distribution. In contrast to the normalization used in section 6.4.2 here a normalization on the sine of the geomagnetic angle is used. The normalized amplitude is proportional to the energy reconstructed by the respective host experiment. The median signal amplitudes per energy  $\kappa$  of both experiments are compared taking into account the different geomagnetic fields and observation levels. Therefore the slope derived from figure 6.24 (left) is divided by the corresponding geomagnetic field strength. The derived values are:

$$\kappa_{LOPES} = 15.40 \pm 0.26 \frac{\mu\text{V/m}}{\mu\text{T EeV}}$$

$$\kappa_{Tunka-Rex} = 14.65 \pm 0.18 \frac{\mu\text{V/m}}{\mu\text{T EeV}}$$

The ratio of  $\kappa_{Tunka-Rex}$  and  $\kappa_{LOPES}$  is proportional to the reconstructed energies of Tunka-133 and KASCADE-Grande. The resulting ratio is

$$f_{amp} = \frac{\kappa_{Tunka-Rex}}{\kappa_{LOPES}} = 0.95 \pm 0.09,$$

which means that the energy scale of KASCADE-Grande is  $5\% \pm 9\%$  lower than the energy scale of Tunka-133.

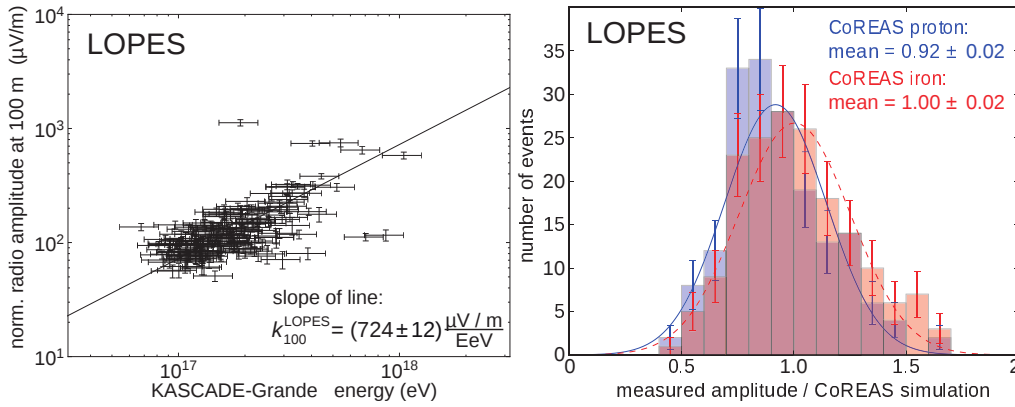


Figure 6.24: Left: Correlation of  $\epsilon_{100}$  measured by LOPES and the energy reconstructed by KASCADE-Grande. Right: Ratio of the measured and simulated amplitude  $\epsilon_{100}$  for LOPES data and CoREAS end-to-end simulations including noise (Hiller et al., 2016).

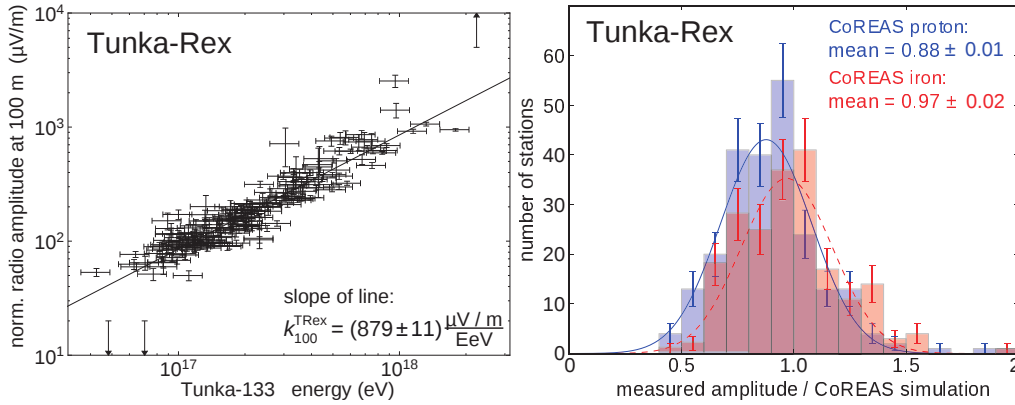


Figure 6.25: Left: Correlation of the amplitude at 100 m distance measured by Tunka-Rex and the energy reconstructed by Tunka-133. Right: Ratio of the measured and simulated amplitudes for Tunka-Rex data and CoREAS end-to-end simulations including noise reconstructed with the Tunka-Rex software (Hiller et al., 2016).

The second approach is based on CoREAS simulations as a common benchmark. The measured amplitudes are compared to the amplitudes derived with the end-to-end simulations including all characteristics of the respective experiments including antennas, noise and geographical effects. Each experiment determines the ratio of the measured

and simulated amplitudes using their standard analysis. The energy spectrum presented in Apel et al. (2012b) is based on an improved energy reconstruction compared to the one used as input for the CoREAS simulations of the LOPES events. Therefore the amplitudes of the simulations were rescaled linearly by the shift of the reconstructed energy. Since the mass distribution of the primary particles is unknown, simulations for both proton and iron primaries are used. The ratio of the measured and simulated amplitude for LOPES is shown in figure 6.24 on the right. For Tunka-Rex the corresponding plots are shown in figure 6.25.

The ratio of the simulated and measured amplitudes are again proportional to the ratio of the reconstructed energies of Tunka-133 and KASCADE-Grande. Two different ratios are derived for the two primary particle types: For proton primaries  $f_{sim}^p = 0.96 \pm 0.05$  and for iron primaries  $f_{sim}^{Fe} = 0.97 \pm 0.06$ . This is in the same order as the ratio obtained by the first approach.

Figure 6.26 summarizes the achieved results. In Hiller et al. (2016) it is concluded that for the observed energy range of  $10^{17}$ – $10^{18}$  eV the spectra of Tunka-133 and KASCADE-Grande can be brought to agreement by a systematic shift of 4%.

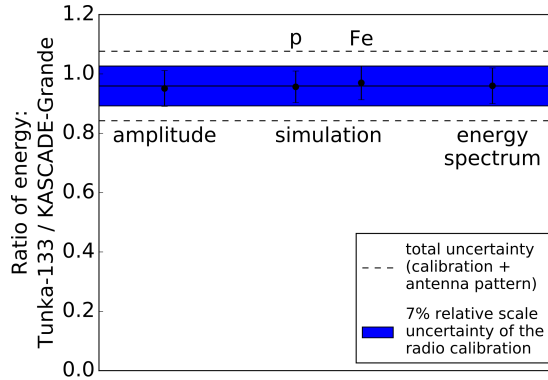


Figure 6.26: Summary of the different comparisons of the energy scales of Tunka-133 and KASCADE-Grande as presented in Hiller et al. (2016).

## 6.5 Reconstruction of the shower maximum

Radio measurements are sensitive to the depth of the shower maximum  $X_{max}$  via the opening angle of the radio front and the slope of the lateral distribution. LOPES presented a reconstruction method for each of these quantities.

The slope method, based on the lateral distribution was published in Apel et al. (2014a). There, a correlation formula was developed based on CoREAS simulations to calculate the shower maximum from the slope derived by a Gaussian fit. This formula was then applied on measured data to reconstruct the shower maximum. As shown in section 4.4 and section 5.6 no change of the reconstructed slope is expected neither due to the usage of the end-to-end simulations nor due to the updated calibration values. The results shown in Apel et al. (2014a) related to the shower maximum should therefore not change significantly using the improved analysis and are still valid.

A reconstruction of the shower maximum via the cone angle  $\rho$  of the radio front was presented in Apel et al. (2014b). Here, a function correlating the cone angle and the shower maximum was also developed based on CoREAS simulations and applied to data. For the simulations the cone angle was derived by a fit of the lateral time distribution while for measurements the cone angle derived from the beamforming was used. With the now developed detector simulation it is possible to also use the beamforming method for the simulations. The principle approach is the same as presented in the previous publication but now the beamforming method is used for both, data and simulations. The formula applied to data is developed based on end-to-end simulations including noise which best represent the true measurements.

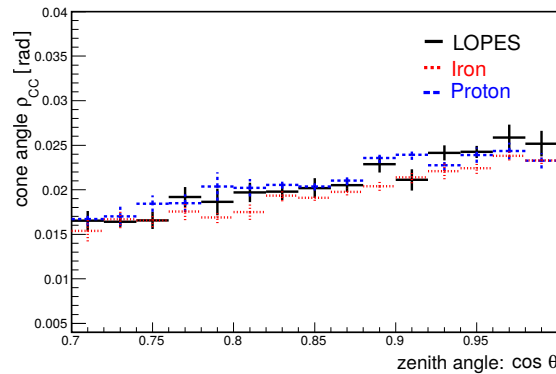


Figure 6.27: Profile of the cone angle  $\rho_{CC}$  as a function of  $\cos(\theta)$  and a power law fit for data and CoREAS simulations.

First the correlation between the cone angle and the depth of shower maximum is calculated for the end-to-end simulations including noise, and then the obtained formula is applied to data. A direct correlation of measured data with the shower maximum is not possible since a measure for the depth of shower maximum is not provided by KASCADE-Grande.

In first order the cone angle  $\rho_{CC}$  depends on the zenith angle of the incoming shower which has to be corrected for. Therefore a profile of  $\rho_{CC}$  is plotted as a function of  $\cos(\theta)$ , see figure 6.27, and fitted by a power law with the index  $\gamma$  (not shown in the plot). For proton simulations the fit results in  $\gamma_p = 1.15 \pm 0.1$  while for iron simulations

$\gamma_{Fe} = 1.33 \pm 0.09$ . For the correction the mean value of both, which is  $\gamma = 1.24$ , is used. This is slightly below the published value of  $\gamma = 1.485$ , which was determined using pure simulations without detector simulation and without noise. With the corrected cone angles their correlation factor  $k$  with the shower maximum is determined by dividing the average true  $X_{max}$  by the average  $\rho_{CC,corr}$ . Here no discrimination of iron and proton is done since the aim is to get a formula independent of the primary particle. The resulting correlation factor is  $k = 26143 \text{ g/cm}^2$  while the formerly published one was  $k = 25200 \text{ g/cm}^2$ . With the following formula the reconstructed shower maximum is then calculated for both, data and simulations.

$$X_{max} = k \cdot \rho_{CC,corr} = 26143 \text{ g/cm}^2 \cdot \rho_{CC} \cdot \cos^{-1.24}(\theta) \quad (6.6)$$

In figure 6.28 left, the reconstructed shower maxima are shown for the measurements and the iron and proton CoREAS simulations while on the right the true  $X_{max}$  distributions are shown.

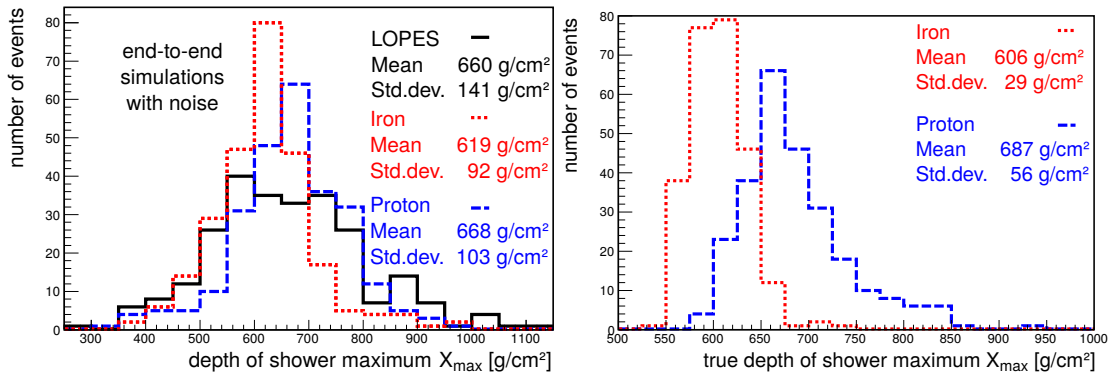


Figure 6.28: Left: Distribution of the reconstructed shower maxima derived for LOPES and end-to-end CoREAS simulations including the detector simulation and noise. Right: Distribution of the true shower maxima for the CoREAS simulations.

The mean value of the measurements is between those of the extreme cases of pure iron and pure proton simulations. Within uncertainties the reconstructed mean values for the simulations are compatible with the true mean values.

From the width of the reconstructed simulations the uncertainty arising from the method itself including noise can be determined. To do so, the true width of the distribution, known from the true  $X_{max}$  values, is quadratically subtracted. For proton simulations the resulting uncertainty is  $\sigma_{p,method} = 86 \text{ g/cm}^2$  and for iron it is  $\sigma_{Fe,method} = 87 \text{ g/cm}^2$ .

Another way of calculating the uncertainty for the method including noise is from the deviation of the true and reconstructed shower maximum as shown in figure 6.29. There the width of the distributions are around  $82 \text{ g/cm}^2$ . Furthermore a bias depending on the primary particle is observed. In total the mean value of the proton-induced showers is shifted by about  $23 \text{ g/cm}^2$  compared to the mean value of the iron-induced showers. The bias is still small compared to the width of the distributions and, combining both, a total uncertainty of  $86 \text{ g/cm}^2$  is derived which is the same as using the other method.

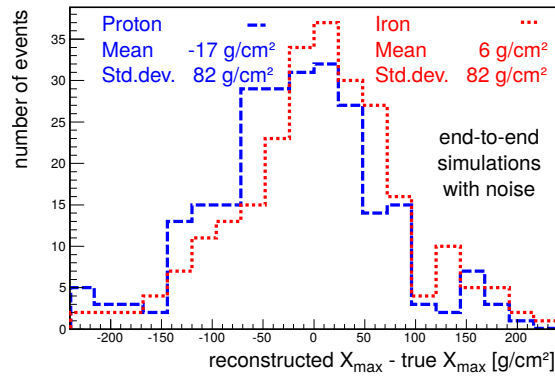


Figure 6.29: Deviation of the true and reconstructed shower maxima for proton and iron induced air shower simulations. The reconstructed values are derived for end-to-end CoREAS simulations including noise and the full detector simulation.

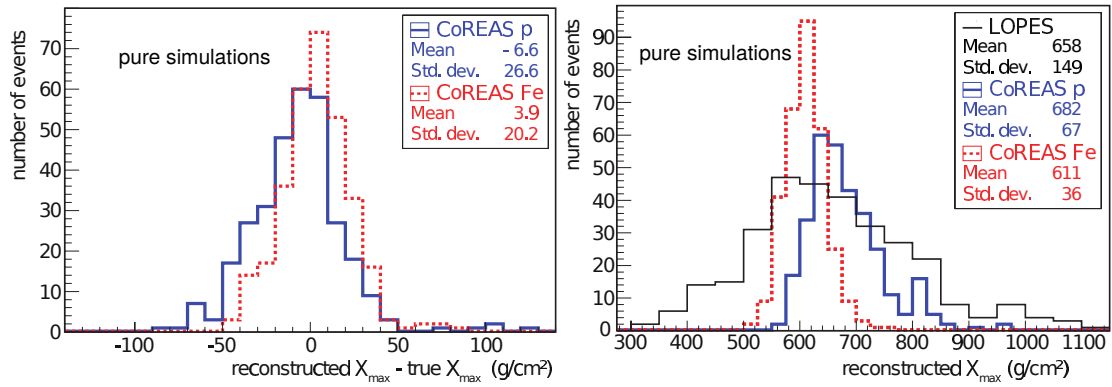


Figure 6.30: Former results as published in Apel et al. (2014b). Left: Deviation of the true and reconstructed shower maximum for pure CoREAS simulations. Right: Distribution of the reconstructed shower maxima for LOPES derived using the beamforming method and for pure CoREAS simulations derived from the lateral time fit.

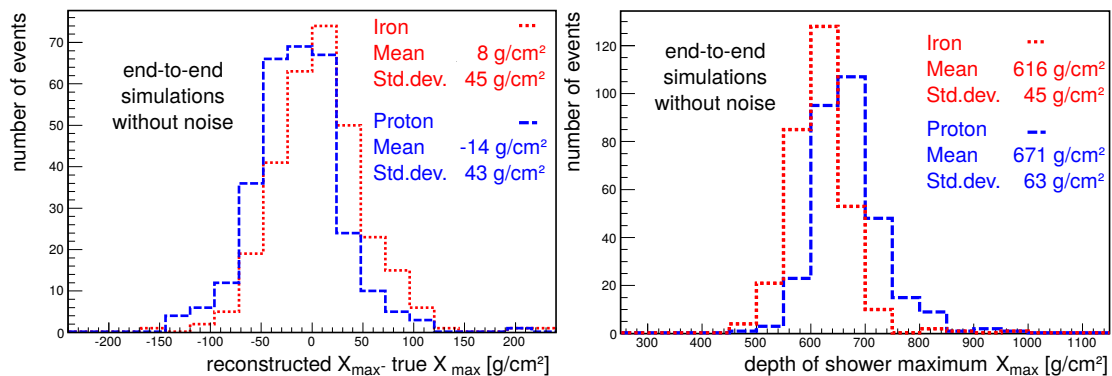


Figure 6.31: Left: Deviation of the true and reconstructed shower maxima for proton and iron induced air shower simulations. Right: Distribution of the reconstructed shower maxima derived for end-to-end CoREAS simulations including only the detector simulation.

In Apel et al. (2014b) the uncertainty for the method is stated to be less than  $30 \text{ g/cm}^2$  which does not include noise and is based on the lateral time distribution, using the exact  $t_0$  as input, instead of the beamforming, see figure 6.30 on the left. To determine the uncertainty also for the beamforming method itself the analysis is done for end-to-end simulations without additional noise. The resulting distributions are shown in figure 6.31.

Quadratically subtracting the true width from the reconstructed width an uncertainty of the method is determined, yielding to  $\sigma_{p,method,w/o\ noise} = 32 \text{ g/cm}^2$  for proton and  $\sigma_{Fe,method,w/o\ noise} = 45 \text{ g/cm}^2$  for iron. From the distribution of the absolute difference between true and reconstructed depth of shower maximum, see figure 6.31 on the left, an uncertainty of  $45 \text{ g/cm}^2$  for proton and  $46 \text{ g/cm}^2$  for iron are derived. These values are higher than the formerly stated uncertainty of  $30 \text{ g/cm}^2$  for the same method based on the lateral time distribution. This shows that in principle a reconstruction of the cone angle based on the lateral time distribution gives better results compared to the beamforming method. But for experiments like LOPES a fit to the lateral time distribution suffers from high uncertainties. These are not only uncertainties coming from noise but also from the unclear determination of the zero-time  $t_0$ . Using the beamforming method to reconstruct the cone angle still a resolution of the shower maximum of less than  $50 \text{ g/cm}^2$  can be reached. The same resolution was achieved with the slope method presented in Apel et al. (2014a)

The width of the reconstructed shower maximum distribution for LOPES measurements is  $\sigma_{LOPES} = 141 \text{ g/cm}^2$ , see figure 6.28, which is comparable with the one from Apel et al. (2014b) of  $149 \text{ g/cm}^2$ , see figure 6.30 on the right. As done in Apel et al. (2014b) the resolution for LOPES is determined from this width of the distribution using the true expected width of the depth of shower maximum. Tunka indicates a width of the shower maximum distribution of  $55 \text{ g/cm}^2$  at  $10^{17} \text{ eV}$  (Epimakhov et al., 2013) which is quadratically subtracted from the width measured with LOPES. This results in a resolution of  $130 \text{ g/cm}^2$  while in the former publication the resolution was  $140 \text{ g/cm}^2$ . A reconstruction based on the same quantities for data and simulations, namely the cone angle derived by beamforming, confirms former results and only gives a slightly better resolution. For the reconstruction of the shower maximum using the lateral slope a resolution of  $95 \text{ g/cm}^2$  was achieved for LOPES data (Apel et al., 2014a). An analysis combining both methods is promising and might result in a better resolution.

## 6.6 Conclusion

Using the improved analysis, a good agreement of LOPES measurements and CoREAS-simulated events was shown. The state-of-the-art simulation code CoREAS is able to predict the expected radio amplitude at ground. Using a full detector simulation and the LOPES standard analysis pipeline the measured amplitudes are reproduced. The comparison is not only based on the lateral distribution but also on the beamforming analysis, which is applied for the first time on simulated events. A good agreement is shown for all observed properties and the simulated and measured values are compatible within uncertainties.

With the LOPES experiment it was possible to show that the three main air shower properties, namely arrival direction, energy and mass of the primary particle, can be related to and reconstructed from radio emission quantities. While the resolution of LOPES is mainly limited by noise the presented methods can be adopted by other experiments with higher precision. Furthermore, the resolution obtained for combined LOPES-KASCADE(-Grande) measurements can only be as good as those from KASCADE-Grande. Using CoREAS simulations including noise it became possible to determine resolutions independent of the reconstruction accuracy of KASCADE-Grande. This was done for all three air shower parameters and table 6.5 summarises the results.

These results show that the radio technique indeed is very promising and already with a small radio experiment, originally just built as a prototype station, resolutions compatible with other detection techniques are achieved.

**Table 6.5:** Resolution of the reconstructed air shower parameters. The resolution of LOPES always depends on the resolution of the used reference values. The method including noise corresponds to a LOPES only resolution.

	LOPES	KASCADE-Grande	method including noise	method itself
arrival direction	$\sim 0.5^\circ$ *	$< 0.5^\circ$	$\sim 0.065^\circ$	$\sim 0.05^\circ$
energy by CC-beam	$< 25\%$ *	$\sim 20\%$	$< 15\%$	$< 13\%$
shower maximum by $\rho_{CC}$	$\sim 130 \text{ g/cm}^2$ **		$\sim 86 \text{ g/cm}^2$	$< 50 \text{ g/cm}^2$

\* combined resolution of LOPES and KASCADE(-Grande)

\*\* resolution of LOPES assuming a true width of  $55 \text{ g/cm}^2$



# 7

## Conclusion

The LOPES experiment played a pioneering role in the development of the radio measurement technique to become competitive with already established techniques. On the technical part as well as on the analysis of the data, LOPES very successfully developed new methods that were often used by follow-up experiments.

One of the first results of LOPES was to confirm the dependence of the radio signal on the geomagnetic angle and a linear correlation of the amplitude with the air shower energy. This was expected from the understanding of the radio emission processes at that time. Furthermore LOPES showed that it is possible to reconstruct the arrival direction of the air shower using an interferometric beamforming. It was also shown that the slope of the lateral distribution and the cone angle of the radio wavefront are both sensitive on the depth of the shower maximum.

With the methods developed for LOPES it was therefore demonstrated that the radio technique is sensitive to the important air shower parameters which are the arrival direction, the energy and the mass of the primary particle. The accuracy achieved by LOPES is mainly limited by the high radio background at the detector site.

Despite these great results some open questions remained which were addressed in the scope of this work. This mainly concerns the question how precise the electric field can be reconstructed with the LOPES analysis pipeline. Furthermore there was a discrepancy between the amplitude measured by LOPES and the one predicted by CoREAS which was not understood. To be able to answer these and related questions a full detector simulation was developed and a thorough review of the amplitude calibration was done.

Applying the developed detector simulation on a set of CoREAS simulations allowed a study on the influence of the standard LOPES pipeline on the reconstructed parameters and how noise influences the measurements. It was shown that the electric field component determined with the simplified reconstruction employed in LOPES using the amplitude in a single antenna, reproduces the true amplitude within 10 %

accuracy for typical LOPES event selections.

This leads to only minor changes of the amplitude parameter  $\epsilon_{100}$  derived from the lateral distribution. A negligible shift was observed for the east-west signal and the observed scatter is explained by statistical uncertainties from the fit. This also shows that the applied noise correction works properly for the reconstructed amplitude.

The influence on the slope parameter  $\eta$  is more prominent but by chance this effect cancels out with the influence of noise. While the simplified reconstruction leads to a steeper slope the measured noise leads to a flatter slope.

Overall the slope and the amplitude reconstructed from the lateral distribution of simulations including the simplified reconstruction and noise are compatible with those obtained from pure simulations. This implies that former published results based on the pure simulations are still valid.

The application of the standard reconstruction pipeline to simulations made, for the first time, an interferometric analysis of simulations possible and the same reconstruction methods could be applied on simulated events as were used for measured data.

After developing the detector simulation a closer look at the antenna calibration was taken. Beside the review of the the antenna gain pattern and the amplitude calibration software also a cross-calibration with LOFAR and Tunka-Rex was performed. In this context it turned out that the calibration values of the reference source were valid for free-field conditions while for air shower measurement purposes free-space conditions are needed. Such free-space calibration values were obtained from the manufacturer of the reference source and the calculation of the amplification factor was repeated using the new values and independently implemented analysis software.

With the new amplitude calibration and the detector simulation a detailed comparison of CoREAS simulations and LOPES measurements for different quantities was possible. Before this work, only the lateral distribution functions were used for the comparison. The usage of the developed detector simulation made a comparison also on the CC-beam quantities possible. Due to the updated amplitude calibration using free-space calibration data the reconstructed amplitudes of the measurements dropped significantly. CoREAS end-to-end simulations and LOPES measurements now show a very good agreement in all observed quantities which are the CC-beam amplitude, the lateral amplitude at 100 m  $\epsilon_{100}$ , the lateral slope parameter  $\eta$  and the cone angle determined by the beamforming method  $\rho_{CC}$ . It can conclusively be stated that the CoREAS simulations properly describe the measured LOPES data within uncertainties. This means that our current understanding of radio emission physics is correct and radio measurements can be used as an independent energy estimator for air shower detections.

Once more LOPES confirms its pioneering role in the radio detection technique since so far no other experiment could provide such a detailed comparison of data and simulations not only based on the lateral distribution but also on interferometrically obtained quantities.

The reconstruction methods for the arrival direction, the air shower energy and the depth of the shower maximum were applied to data and also to end-to-end

simulations. The application to data confirms former results obtained by LOPES, taking into account the new amplitude calibration. While for the measurements only a combined reconstruction accuracy for LOPES and KASCADE-Grande can be determined, the end-to-end simulations newly allow to calculate the expected LOPES-only accuracy and the intrinsic accuracy of the reconstruction methods. For the direction reconstruction already a small radio experiment like LOPES can achieve a resolution of less than  $0.07^\circ$ . Also an energy reconstruction with a resolution of less than 15 % and a resolution of the depth of the shower maximum of less than  $90 \text{ g/cm}^2$  was derived, even including the influence of noise. At least the achieved accuracy of the energy reconstruction and of the arrival direction is competitive with other detection techniques.

With this work it was possible to finally state that our current understanding of radio emission physics represented in the CoREAS simulations properly describes the LOPES measurements and that the simplified reconstruction as used in the standard LOPES pipeline is valid. This implies that former published LOPES results are valid, taking into account a drop of the measured amplitude. Furthermore it was shown that the radio detection technique is competitive with other established techniques at least for radio quiet areas. Especially in combination with other detection techniques, radio measurements are a promising method to help address the remaining questions of cosmic ray physics.



# A

## Histograms of the radio emission properties

Histograms of the radio emission properties for LOPES data and corresponding CoREAS simulations. For the simulations the energy and arrival direction provided by KASCADE-Grande of selected LOPES events are used as input. Since the primary particle type of the measured events is not known each event is simulated for the two extreme cases of iron and proton primary. There are three different ways of further processing the simulations. The so called pure simulations or true simulations are just filtered by a rectangular filter to 43-74 MHz, the frequency band of LOPES. If the simulated events undergo the full detector simulation and the LOPES standard analysis pipeline they are called end-to-end simulations or simplified simulations. If no noise is added to the simulations the noise correction implemented in the reconstruction pipeline is switched off. Otherwise, for simulated events including measured noise the reconstruction pipeline is exactly the same as for data. So in total the three simulation set 'pure simulations', 'end-to-end simulations w/o noise' and 'end-to-end simulations with noise' are available each for both primary particle types.

In the following figures the histograms of the typical reconstructed parameters which are used for further investigations are shown. Since no beamforming is done for the pure simulations the CC-beam amplitude and cone angle for those cannot be calculated.

### A.1 Properties from lateral distribution

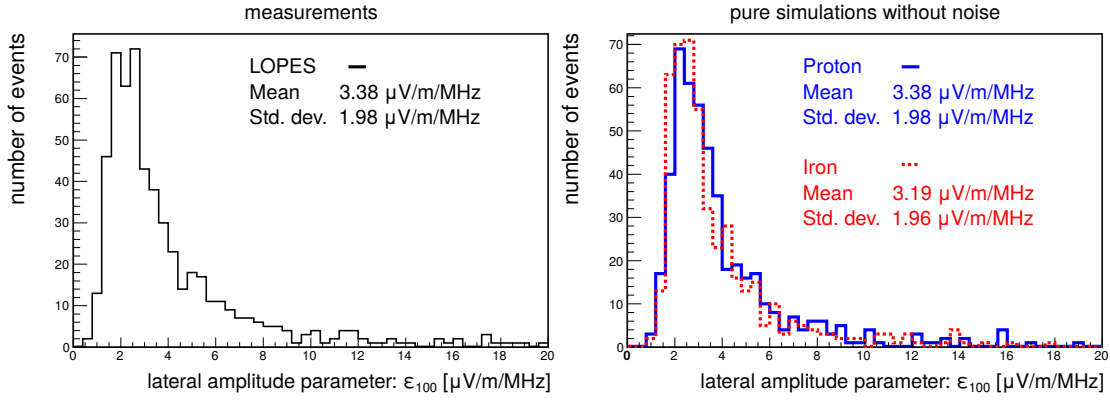


Figure A.1: Lateral amplitude parameter fitted at 100 m axis distance  $\epsilon_{100}$  for LOPES data (left) and pure CoREAS simulations (right).

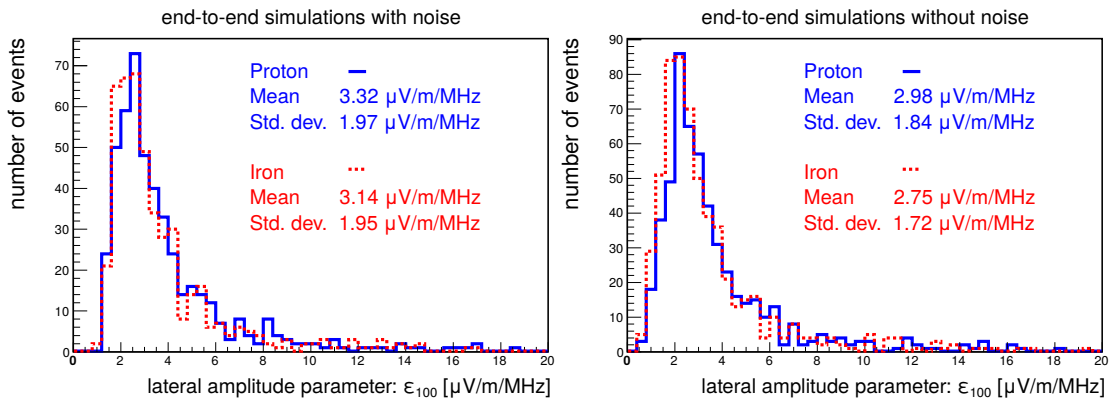


Figure A.2: Lateral amplitude parameter fitted at 100 m axis distance  $\epsilon_{100}$  for end-to-end CoREAS simulations with noise (left) and without noise (right).

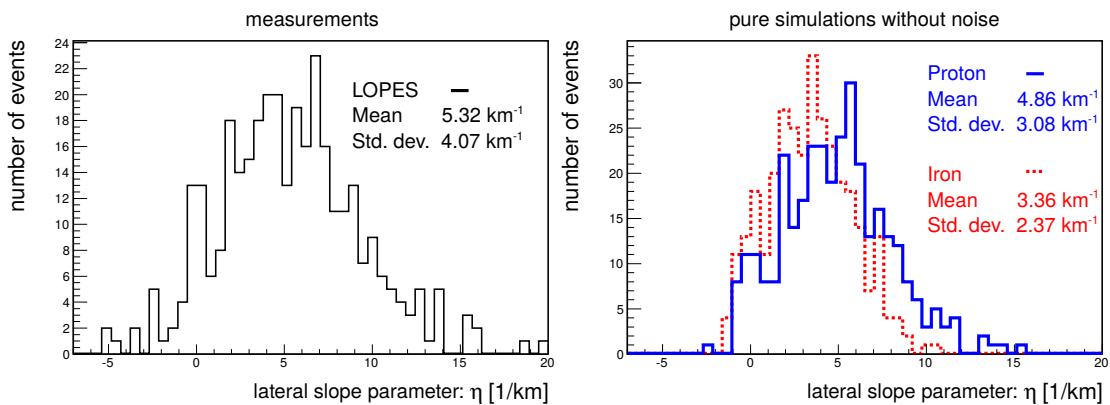


Figure A.3: Lateral slope parameter  $\eta$  for LOPES data (left) and pure CoREAS simulations (right).

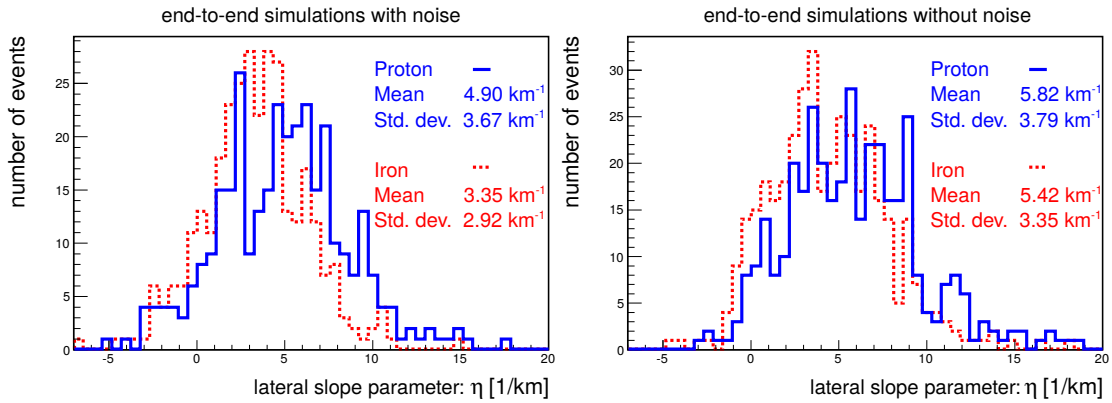


Figure A.4: Lateral slope parameter  $\eta$  for end-to-end CoREAS simulations with noise (left) and without noise (right).

## A.2 Properties from beamforming

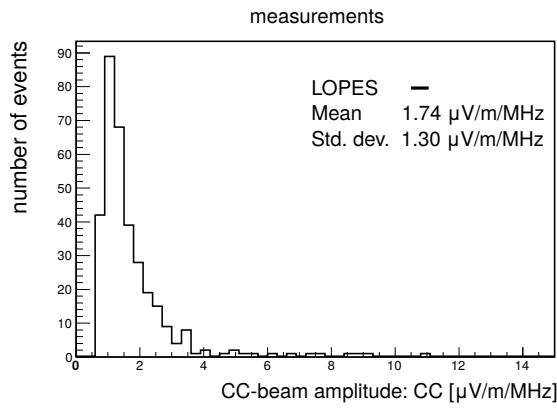


Figure A.5: CC-beam amplitude for LOPES data.

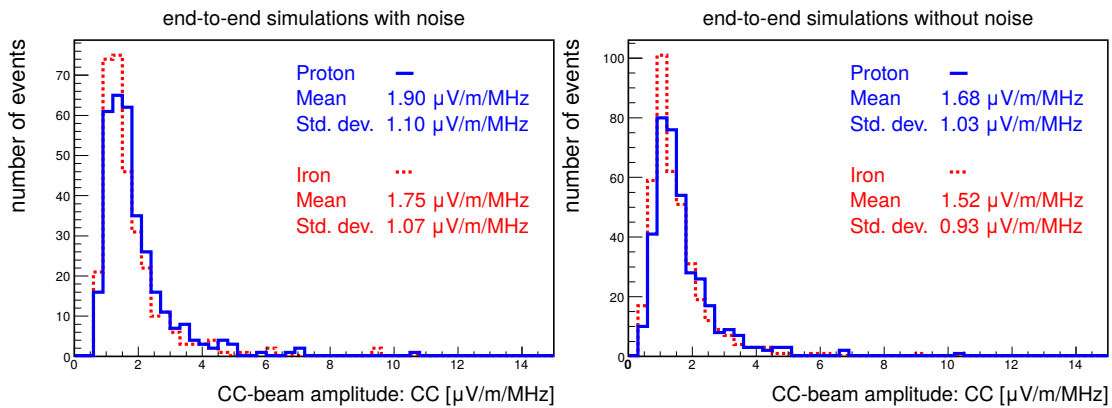


Figure A.6: CC-beam amplitude for end-to-end CoREAS simulations with noise (left) and without noise (right).

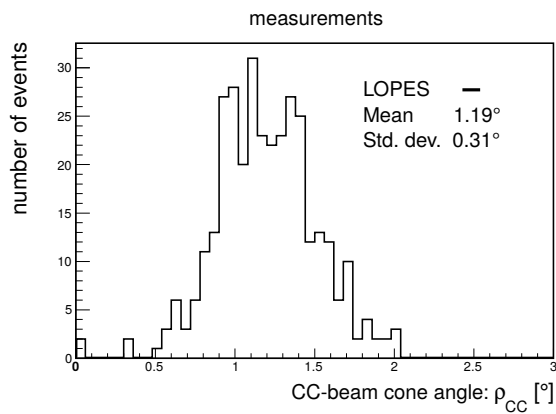


Figure A.7: CC-beam cone angle  $\rho_{CC}$  for LOPES data.

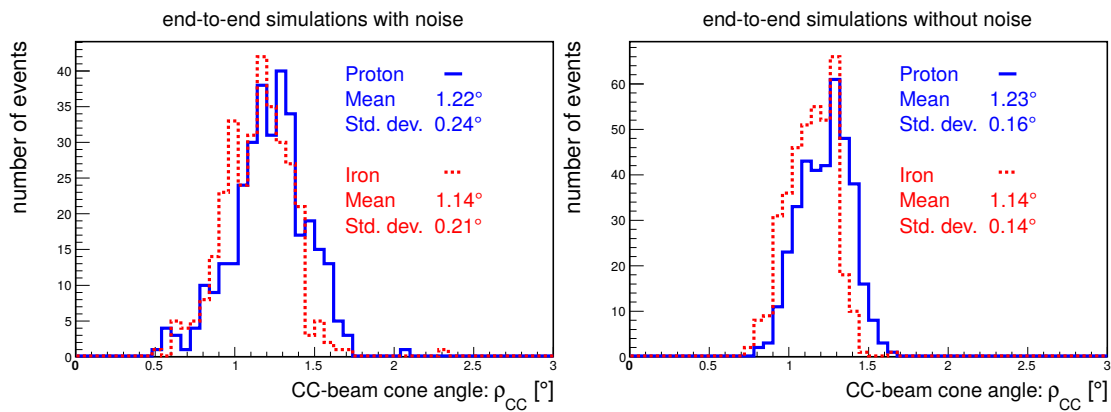


Figure A.8: CC-beam cone angle  $\rho_{CC}$  for end-to-end CoREAS simulations with noise (left) and without noise (right).

### A.3 Cone angle from lateral time fit

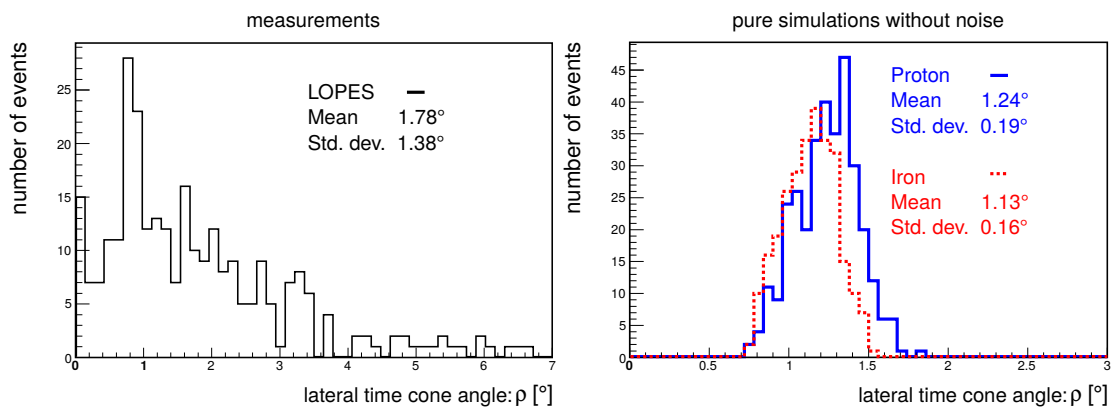


Figure A.9: Cone angle  $\rho$  derived from a fit to the lateral time distribution for LOPES data (left) and pure CoREAS simulations (right).

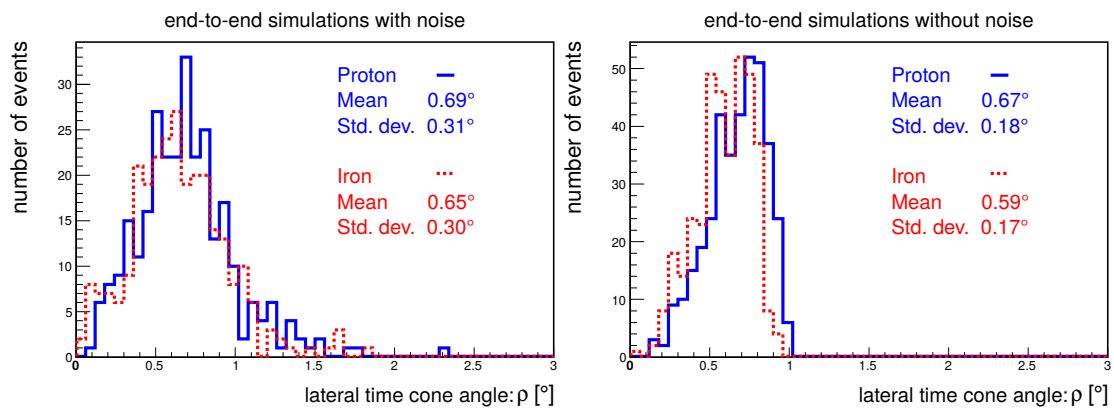


Figure A.10: Cone angle  $\rho$  derived from a fit to the lateral time distribution for end-to-end CoREAS simulations with noise (left) and without noise (right).



# B

## Calibration certificate of reference source

Updated calibration certificate for the reference source used for the absolute amplitude calibration. While the measurement itself is done in free field conditions including reflections from ground the reported calibration values are now calculated for the free space conditions.



Advanced Test Solutions for EMC

**Teseq GmbH** Landsberger Straße 255 12623 Berlin Germany  
 T + 49 30 56 59 88 0 F + 49 30 56 59 88 34 www.teseq.com

Certificate N° **A021060/057** Page **1** of **5** pages  
 Zertifikat Nr. **A021060/057** Seite **1** von **5** Seiten

Customer **KIT** Order N°, date **254/20588347/**  
 Kunde **Karlsruher Institut für Technologie** Auftrags-Nr., Datum **IKP/GFB**  
**76344 Eggenstein-Leopoldshafen** **29.01.2015**

**Certificate of Calibration - Kalibrierzertifikat**

Object **Reference Radiation Source**  
 Gegenstand  
 Manufacturer **SCHAFFNER**  
 Hersteller  
 Model **VSQ 1000 consisting of RSG 1000 ; DPA 4000**  
 Typ  
 Serial N° **20563; 18138**  
 Serien-Nr.  
 Remarks **special Frequency range 30-100 MHz; 1 MHz Step; Free Space**  
 Bemerkungen  
 Date of calibration **03 February 2015**  
 Datum der Kalibrierung

This calibration certificate documents the traceability to national standards, which realize the physical units of measurements (SI).  
 Dieses Kalibrierzertifikat dokumentiert die Rückführbarkeit auf nationale Normale zur Darstellung der physikalischen Einheiten (SI).

The measurements, the uncertainties with confidence probability and calibration methods are given on the following pages and are part of the certificate.  
 Messresultate, Messunsicherheiten mit Vertrauensbereich und Messverfahren sind auf den folgenden Seiten aufgeführt und sind Teil des Zertifikates.

Place and date Ort und Datum	The Calibration Laboratory Die Kalibrierstelle	Person in charge Bearbeiter
Berlin, 23 February 2015	 U. Karsten	 T. Gör

This certificate shall not be published or reproduced other than in full.  
 Der Inhalt dieses Zertifikates darf nur in vollständiger Form veröffentlicht oder weitergegeben werden.  
 Calibration in line with EN ISO/IEC 17025 specifications

Certificate N° **A021060/057**Page **2** of **5** pages

Calibration method: The calibration method is defined in the VSQ 1000 calibration instruction. (see 1.1.)

Calibration equipment: The entire equipment is connected to the respective primary laboratory and therefore directly traceable to national and international standards.

Uncertainty of measurements: The reported expanded uncertainty of measurement is stated as the standard uncertainty of measurement multiplied by the coverage factor  $k = 2$ , which for a normal distribution corresponds to a coverage probability of approximately 95 %.

Validity : This certificate is valid only if the VSQ 1000 is in use according to the standard.

### Uncertainty of measurements

Electrical Field Strength	30 MHz ... 100 MHz	2.5dB
---------------------------	--------------------	-------

### Calibration equipment

Device	Type	Serial number	Next calibration / Traceability / Certificate N° / Date
EMI Measuring Receiver	SMR 4518	016	02.2017 / D-K-15033-01-00 / 4231 / 02.2015
SAC	SAC3+	10107	05.2016 / UKAS 0392 / CS0434 / 05.2013
Antenna	VBA6106A	29750	12.2016 / UKAS 0392 / CA8003 / 12.2014

Calibration environment:	Room temperature	<b>22</b> °C	± 1 °C
	Relative humidity	<b>45</b> %	± 5 %

Certificate N° **A021060/057**

Page **3** of **5** pages

**1. Description of the calibration method**

**1.1. Emission measurement of the VSQ in the SAC3+**

The emission measurement will be done in a standard 3m SAC (with reflective ground).  
The results will be recalculated to a 10m free field.

**Note!**

The reference point for the measurement is the middle point of the dipole antenna.

**VSQ settings:**

Frequency range : 1 MHz

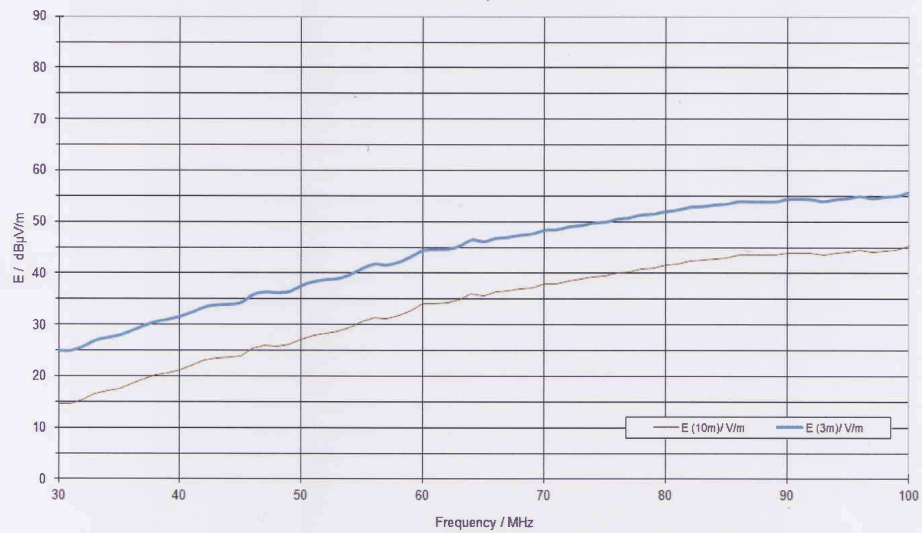
**Receiver settings:**

Frequency range : 30 MHz to 100 MHz  
Step size : 1 MHz  
Bandwidth : 9 kHz  
Detector : AV 20 ms

**Details about the object under calibration**

**2. Calibration results**

Reference Radiation Source VSQ 1000 SN: 20563  
Field Strength @ 3m and 10m Distance  
Free Space





Advanced Test Solutions for EMC

Certificate N° **A021060/057**

Page **5** of **5** pages

Frequency / MHz	E (3m) / $\mu\text{V/m}$	E (10m) / $\mu\text{V/m}$
30	25.0	14.6
31	25.0	14.6
32	25.8	15.4
33	27.0	16.6
34	27.6	17.1
35	28.0	17.6
36	28.9	18.4
37	29.9	19.4
38	30.7	20.2
39	31.1	20.6
40	31.7	21.2
41	32.5	22.1
42	33.5	23.0
43	33.9	23.5
44	34.0	23.6
45	34.4	23.9
46	35.9	25.5
47	36.4	26.0
48	36.3	25.8
49	36.5	26.1
50	37.7	27.2
51	38.4	28.0
52	38.8	28.4
53	39.0	28.6
54	39.8	29.4
55	41.0	30.6
56	41.9	31.4
57	41.7	31.2
58	42.2	31.8
59	43.3	32.8
60	44.5	34.0
61	44.6	34.2
62	44.7	34.2
63	45.3	34.9
64	46.5	36.0
65	46.2	35.7

Frequency / MHz	E (3m) / $\mu\text{V/m}$	E (10m) / $\mu\text{V/m}$
66	46.8	36.4
67	47.0	36.6
68	47.4	37.0
69	47.7	37.2
70	48.4	37.9
71	48.5	38.0
72	49.0	38.6
73	49.3	38.8
74	49.8	39.3
75	50.0	39.5
76	50.5	40.1
77	50.8	40.4
78	51.4	40.9
79	51.5	41.1
80	52.0	41.6
81	52.3	41.9
82	52.9	42.4
83	53.0	42.5
84	53.3	42.9
85	53.5	43.0
86	54.0	43.5
87	53.9	43.5
88	54.0	43.5
89	53.9	43.5
90	54.4	44.0
91	54.5	44.0
92	54.4	43.9
93	54.0	43.6
94	54.4	43.9
95	54.6	44.1
96	55.0	44.5
97	54.6	44.2
98	54.9	44.4
99	55.0	44.6
100	55.7	45.2
101	55.7	45.2

## Bibliography

- Aab, A. et al. (2015). *The Pierre Auger Cosmic Ray Observatory*. Nucl. Instrum. Meth. A, A798: 172–213. doi:10.1016/j.nima.2015.06.058. (Cited on page 6)
- Aab, A. et al. (2016a). *Energy Estimation of Cosmic Rays with the Engineering Radio Array of the Pierre Auger Observatory*. Phys. Rev., D93 (12): 122005. doi:10.1103/PhysRevD.93.122005. (Cited on page 31)
- Aab, A. et al. (2016b). *The Pierre Auger Observatory Upgrade - Preliminary Design Report*. arXiv:1604.03637. (Cited on page 7)
- Abbasi, R. et al. (2016). *Report of the Working Group on the Composition of Ultra High Energy Cosmic Rays*. JPS Conf. Proc., 9: 010016. doi:10.7566/JPSCP.9.010016. (Cited on page 7)
- Abraham J. et al. (2004). *Properties and performance of the prototype instrument for the Pierre Auger Observatory*. Nucl. Instrum. Meth. A, 523 (1-2): 50 – 95. doi:10.1016/j.nima.2003.12.012. (Cited on page 6)
- Abraham J. et al. (2010). *The fluorescence detector of the Pierre Auger Observatory*. Nucl. Instrum. Meth. A, 620 (2-3): 227 – 251. doi:10.1016/j.nima.2010.04.023. (Cited on page 10)
- Aglietta, M. et al. (2004). *The cosmic ray primary composition between  $10^{15}$  and  $10^{16}$  eV from Extensive Air Showers electromagnetic and TeV muon data*. Astropart. Phys., 20 (6): 641 – 652. doi:10.1016/j.astropartphys.2003.10.004. (Cited on page 6)
- Aleksic, J. et al. (2012). *Performance of the MAGIC stereo system obtained with Crab Nebula data*. Astropart. Phys., 35: 435–448. doi:10.1016/j.astropartphys.2011.11.007. (Cited on page 10)
- Allan, H. R. (1971). *Radio Emission From Extensive Air Showers*. Prog. in Element. part. and Cos. Ray Phys., Vol. 10: 171–302. (Cited on page 14)
- Alvarez-Muñiz, J., Jr., W. R. C. and Zas, E. (2012). *Monte Carlo simulations of radio pulses in atmospheric showers using ZHAireS*. Astropart. Phys., 35 (6): 325 – 341. doi:10.1016/j.astropartphys.2011.10.005. (Cited on page 12)
- Alvarez-Muñiz, J. et al. (2013). *The MIDAS telescope for microwave detection of ultra-high energy cosmic rays*. Nucl. Instrum. Meth. A, 719 (0): 70 – 80. doi:10.1016/j.nima.2013.03.030. (Cited on page 16)

- Antoni, T. et al. (2003). *The Cosmic-Ray Experiment KASCADE*. Nucl. Instrum. Meth. A, 513 (3): 490–510. doi:10.1016/S0168-9002(03)02076-X. (Cited on pages 6, 9 and 17)
- Apel, W. et al. (2010). *Lateral distribution of the radio signal in extensive air showers measured with LOPES*. Astropart. Phys., 32 (6): 294 – 303. doi:10.1016/j.astropartphys.2009.09.007. (Cited on page 19)
- Apel, W. et al. (2011a). *Thunderstorm observations by air-shower radio antenna arrays*. Adv. Space Res., 48 (7): 1295 – 1303. doi:10.1016/j.asr.2011.06.003. (Cited on page 11)
- Apel, W. et al. (2012a). *LOPES-3D: An antenna array for full signal detection of air-shower radio emission*. Nucl. Instrum. Meth. A, 696 (0): 100 – 109. doi:10.1016/j.nima.2012.08.082. (Cited on pages 10, 14 and 20)
- Apel, W. et al. (2012b). *The spectrum of high-energy cosmic rays measured with KASCADE-Grande*. Astropart. Phys., 36 (1): 183 – 194. doi:10.1016/j.astropartphys.2012.05.023. (Cited on pages 104 and 106)
- Apel, W. et al. (2013a). *Comparing LOPES measurements of air-shower radio emission with REAS 3.11 and CoREAS simulations*. Astropart. Phys., 50–52 (0): 76 – 91. doi:10.1016/j.astropartphys.2013.09.003. (Cited on pages 26, 31, 32, 84, 86 and 87)
- Apel, W. et al. (2016). *Improved absolute calibration of LOPES measurements and its impact on the comparison with REAS 3.11 and CoREAS simulations*. Astropart. Phys., 75: 72 – 74. doi:10.1016/j.astropartphys.2015.09.002. (Cited on pages 37, 63, 71, 79, 84, 86, 87 and 92)
- Apel, W. D. et al. (2010). *The KASCADE-Grande experiment*. Nucl. Instrum. Meth. A, 620: 202–216. doi:10.1016/j.nima.2010.03.147. (Cited on pages 9 and 17)
- Apel, W. D. et al. (2011b). *Kneelike Structure in the Spectrum of the Heavy Component of Cosmic Rays Observed with KASCADE-Grande*. Phys. Rev. Lett., 107: 171104. doi:10.1103/PhysRevLett.107.171104. (Cited on page 6)
- Apel, W. D. et al. (2012c). *Experimental evidence for the sensitivity of the air-shower radio signal to the longitudinal shower development*. Phys. Rev. D, 85: 071101. doi:10.1103/PhysRevD.85.071101. (Cited on page 27)
- Apel, W. D. et al. (2013b). *Ankle-like feature in the energy spectrum of light elements of cosmic rays observed with KASCADE-Grande*. Phys. Rev. D, 87: 081101. doi:10.1103/PhysRevD.87.081101. (Cited on page 6)
- Apel, W. D. et al. (2014a). *Reconstruction of the energy and depth of maximum of cosmic-ray air showers from LOPES radio measurements*. Phys. Rev. D, 90: 062001. doi:10.1103/PhysRevD.90.062001. (Cited on pages 11, 20, 27, 88, 102, 103, 104, 107 and 110)
- Apel, W. D. et al. (2014b). *The wavefront of the radio signal emitted by cosmic ray air showers*. J. Cosmol. Astropart. P., 09: 025. doi:10.1088/1475-7516/2014/09/025. (Cited on pages 11, 20, 24, 27, 47, 49, 75, 79, 82, 90, 91, 92, 93, 107, 109 and 110)
- Arts, M. J. (2002). *EM simulations of a LOFAR LBH antenna*. personal communication. (Cited on pages 41 and 63)

- Askaryan, G. A. (1962). *Excess negative charge of an electron-photon shower and its coherent radio emission*. Sov. Phys. JETP, 14: 441. (Cited on pages 11 and 13)
- Auger, P. et al. (1939). *Extensive Cosmic-Ray Showers*. Rev. Mod. Phys., 11 (3-4): 288–291. doi:10.1103/RevModPhys.11.288. (Cited on page 7)
- Battistoni, G. et al. (2016). *The FLUKA Code: An Accurate Simulation Tool for Particle Therapy*. Front. Oncol., 6: 116. doi:10.3389/fonc.2016.00116. (Cited on page 34)
- Bezyazeev, P. et al. (2015). *Measurement of cosmic-ray air showers with the Tunka Radio Extension (Tunka-Rex)*. Nulc. Instrum. Meth. A, 802: 89 – 96. doi:10.1016/j.nima.2015.08.061. (Cited on page 15)
- Bezyazeev, P. et al. (2016). *Radio measurements of the energy and the depth of the shower maximum of cosmic-ray air showers by Tunka-Rex*. J. Cosmol. Astropart. P., 2016 (01): 052. doi:10.1088/1475-7516/2016/01/052. (Cited on page 91)
- Blümer, J., Engel, R. and Hörandel, J. R. (2009). *Cosmic rays from the knee to the highest energies*. Prog. Part. Nucl. Phys., 63 (2): 293 – 338. doi:10.1016/j.pnpnp.2009.05.002. (Cited on page 9)
- Bracewell, R. N. (1986). *The Fourier Transform and Its Applications (Second Edition, Revised)*. McGraw-Hill Book Company. ISBN 0070070156. (Cited on page 24)
- Buitink, S. et al. (2005). *Electric field influence on the radio emission of air showers*. Proceedings of the 29th ICRC 2005, 6: 333. URL <http://www.icrr.u-tokyo.ac.jp/can/icrc2005/>. (Cited on page 20)
- Buitink, S. et al. (2007a). *Amplified radio emission from cosmic ray air showers in thunderstorms*. Astron. Astrophys., 467: 385–394. doi:10.1051/0004-6361:20066006. (Cited on page 14)
- Buitink, S. et al. (2007b). *Shower evolution and radio emission of air showers in thunderstorm electric fields*. Proceedings of the 30th ICRC 2007, 4: 161–164. URL <http://www.icrc2007.unam.mx/proceedings/index>. (Cited on page 20)
- Cossavella, F. (2009). *Measurements of high energy cosmic rays above 10 PeV with KASCADE-Grande*. Ph.D. thesis, Universität Karlsruhe (TH). URL <https://publikationen.bibliothek.kit.edu/200077343>. (Cited on page 33)
- Croes, G. A. (1993). *On AIPS++, A New Astronomical Information Processing System*. 52: 156. URL <http://adsabs.harvard.edu/abs/1993ASPC...52..156C>. (Cited on page 68)
- Ender, M. et al. (2009). *Radio Emission of Extensive Air Showers during Thunderstorms*. Proceedings of the 31st ICRC 2009, 0405. URL <http://icrc2009.uni.lodz.pl/proc/pdf/icrc0405.pdf>. (Cited on page 14)
- Epimakhov, S. et al. (2013). *Elemental Composition of Cosmic Rays above the Knee from  $X_{max}$  measurements of the Tunka Array*. Proceedings of the 33rd ICRC 2013, 0326. URL [www.cbpf.br/~icrc2013/papers/icrc2013-0326.pdf](http://www.cbpf.br/~icrc2013/papers/icrc2013-0326.pdf). (Cited on page 110)

- Falcke, H. et al. (2005). *Detection and imaging of atmospheric radio flashes from cosmic ray air showers*. *Nature*, 435 (7040): 313–316. doi:10.1038/nature03614. (Cited on pages 11, 17, 18 and 20)
- Fick, D. and Hoffmann, D. (2014). *Werner Kollhörster (1887–1945): The German pioneer of cosmic ray physics*. *Astropart. Phys.*, 53 (0): 50 – 54. doi:10.1016/j.astropartphys.2013.09.007. (Cited on page 5)
- Friis, H. T. (1946). *A Note on a Simple Transmission Formula*. *Proceedings of the IRE*, 34 (5): 254–256. doi:10.1109/JRPROC.1946.234568. (Cited on page 67)
- Gaior, R. et al. (2013). *Detection of cosmic rays using microwave radiation at the Pierre Auger Observatory*. *Proceedings of 33rd ICRC 2013*. URL [www.cbpf.br/~icrc2013/papers/icrc2013-0883.pdf](http://www.cbpf.br/~icrc2013/papers/icrc2013-0883.pdf). (Cited on page 16)
- Gaté, F. et al. (2016).  *$X_{max}$  reconstruction from amplitude information with AERA*. *Proceedings of the ARENA*. arXiv:1609.06510. (Cited on page 91)
- Gelb, M. (2012). *Simulation of Extensive Air Showers and their Radio Emission in the Presence of Atmospheric Electric Fields*. Bachelor thesis. (Cited on page 14)
- Gorham, P. W. et al. (2008). *Observations of microwave continuum emission from air shower plasmas*. *Phys. Rev. D*, 78: 032007. doi:10.1103/PhysRevD.78.032007. (Cited on page 16)
- Greisen, K. (1966). *End to the cosmic-ray spectrum?* *Phys. Rev. Lett.*, 16: 748–750. doi:10.1103/PhysRevLett.16.748. (Cited on page 6)
- Haungs, A., Rebel, H. and Roth, M. (2003). *Energy spectrum and mass composition of high-energy cosmic rays*. *Rep. Prog. Phys.*, 66 (7): 1145. URL <http://stacks.iop.org/0034-4885/66/i=7/a=202>. (Cited on pages 8 and 9)
- Haungs, A. et al. (2015). *KCDC — The KASCADE Cosmic-ray Data Centre*. *Proceedings of 24th ECRS 2014, JPCS*, 632 (1): 012011. doi:10.1088/1742-6596/632/1/012011. (Cited on page 22)
- Heck, D. et al. (1998). *CORSIKA: A Monte Carlo Code to Simulate Extensive Air Showers*. FZKA Report 6019, Forschungszentrum Karlsruhe. URL <https://publikationen.bibliothek.kit.edu/270043064>. (Cited on pages 8, 31 and 34)
- Heitler, W. (1954). *The Quantum Theory of Radiation*. Oxford University Press, 3rd edition. (Cited on page 8)
- Hess, V. F. (1912). *Über Beobachtungen der durchdringenden Strahlung bei sieben Freiballonfahrten*. *Phys. Z.*, 13: 1084. URL <https://www.mpi-hd.mpg.de/hfm/HESS/public/HessArticle.pdf>. (Cited on page 5)
- Hiller, R. (2016). *Radio measurements for determining the energy scale of cosmic rays*. Ph.D. thesis, Karlsruhe Institute of Technology. URL <https://publikationen.bibliothek.kit.edu/1000053456>. (Cited on page 70)

- Hiller, R. et al. (2016). *A comparison of the cosmic-ray energy scales of Tunka-133 and KASCADE-Grande via their radio extensions Tunka-Rex and LOPES*. Phys. Lett. B, 763: 179 – 185. doi:10.1016/j.physletb.2016.10.031. (Cited on pages 79, 88, 104, 105 and 106)
- Hinton, J. A. (2004). *The Status of the H.E.S.S. project*. New Astron. Rev., 48: 331–337. doi:10.1016/j.newar.2003.12.004. (Cited on page 10)
- Hoover, S. et al. (2010). *Observation of Ultrahigh-Energy Cosmic Rays with the ANITA Balloon-Borne Radio Interferometer*. Phys. Rev. Lett., 105: 151101. doi:10.1103/PhysRevLett.105.151101. (Cited on page 16)
- Horneffer, A. (2006). *Measuring Radio Emission from Cosmic Ray Air Showers with a Digital Radio Telescope*. Ph.D. thesis, Rheinische Friedrich-Wilhelms-Universität Bonn, Germany. URL <http://hss.ulb.uni-bonn.de/2006/0781/0781.htm>. (Cited on pages 18 and 46)
- Horneffer, A. et al. (2007). *Primary Particle Energy Calibration of the EAS Radio Pulse Height*. Proceedings of 30th ICRC 2007, 4: 83–86. URL <http://www.icrc2007.unam.mx/proceedings/index>. (Cited on pages 19, 21 and 94)
- Huber, D. (2014). *Analysing the electric field vector of air shower radio emission*. Ph.D. thesis, Karlsruhe Institute of Technology, IEKP. URL <https://publikationen.bibliothek.kit.edu/1000043289>. (Cited on pages 22 and 23)
- Huege, T. (2013). *Theory and simulations of air shower radio emission*. Proceedings of the 5th ARENA 2012, AIP Conf. Proc., 1535: 121. doi:10.1063/1.4807533. (Cited on page 11)
- Huege, T. (2014). *The renaissance of radio detection of cosmic rays*. Proceedings of the 33rd ICRC 2013, Braz. J. Phys., 44: 520–529. doi:10.1007/s13538-014-0226-6. (Cited on page 13)
- Huege, T. (2016). *Radio detection of cosmic ray air showers in the digital era*. Phys. Rep., 620: 1–52. doi:10.1016/j.physrep.2016.02.001. (Cited on page 11)
- Huege, T. and James, C. (2013). *Full Monte Carlo simulations of radio emission from extensive air showers with CoREAS*. Proceedings of the 33rd ICRC 2013, 548. arXiv: 1307.7566. (Cited on page 14)
- Huege, T., Ludwig, M. and James, C. (2013). *Simulating radio emission from air showers with CoREAS*. Proceedings of the 5th ARENA 2012, AIP Conf. Proc., 1535: 128. doi: 10.1063/1.4807534. (Cited on pages 12, 13, 31 and 38)
- Huege, T., Ludwig, M., Scholten, O. and de Vries, K. D. (2012). *The convergence of EAS radio emission models and a detailed comparison of REAS3 and MGMR simulations*. In Proceedings of the 4th ARENA 2010, Nucl. Instr. Meth. A, volume 662, S179–S186. doi:10.1016/j.nima.2010.11.041. (Cited on pages 13 and 14)
- Huege, T., Ulrich, R. and Engel, R. (2007). *REAS2: CORSIKA-based Monte Carlo simulations of geosynchrotron radio emission*. arXiv:0707.3763. (Cited on page 31)

- Huege, T., Ulrich, R. and Engel, R. (2008). *Dependence of geosynchrotron radio emission on the energy and depth of maximum of cosmic ray showers*. *Astropart. Phys.*, 30: 96–104. doi:10.1016/j.astropartphys.2008.07.003. (Cited on page 11)
- Huege, T. et al. (2012). *The LOPES experiment—Recent results, status and perspectives*. Proceedings of the 4th ARENA 2010, *Nucl. Instrum. Meth. A*, 662: S72 – S79. doi: 10.1016/j.nima.2010.11.081. (Cited on page 19)
- Huege, T. and Falcke, H. (2003). *Radio emission from cosmic ray air showers*. *Astron. Astrophys.*, 412 (1): 19–34. doi:10.1051/0004-6361:20031422. (Cited on page 14)
- Hörandel, J. R. (2008). *Cosmic-ray composition and its relation to shock acceleration by supernova remnants*. *Adv. Space Res.*, 41 (3): 442 – 463. doi:10.1016/j.asr.2007.06.008. (Cited on page 7)
- Ivanov, A. A., Knurenko, S. P. and Sleptsov, I. Y. (2009). *Measuring extensive air showers with Cherenkov light detectors of the Yakutsk array: The energy spectrum of cosmic rays*. *New J. Phys.*, 11: 065008. doi:10.1088/1367-2630/11/6/065008. (Cited on page 10)
- Jelley, J. et al. (1965). *Radio Pulses from Extensive Cosmic-Ray Air Showers*. *Nature*, 205: 327–328. doi:10.1038/205327a0. (Cited on page 11)
- Kahn, F. D. and Lerche, I. (1966). *Radiation from cosmic ray air showers*. *Proc. Roy. Soc.*, A-289: 206. (Cited on pages 11 and 13)
- Kawai, H. et al. (2008). *Telescope array experiment*. Proceedings of the 14th ISVHECRI 2006, *Nucl. Phys. Proc. Suppl.*, 175-176: 221–226. doi:10.1016/j.nuclphysbps.2007.11.002. (Cited on page 6)
- Knurenko, S. and Petrov, I. (2015). *Radio signal correlation at 32 MHz with extensive air showers parameters*. Proceedings of the 24th ECRS 2014, *JPCS*, 632 (1): 012100. doi:10.1088/1742-6596/632/1/012100. (Cited on page 15)
- Kostunin, D. et al. (2016). *Reconstruction of air-shower parameters for large-scale radio detectors using the lateral distribution*. *Astropart. Phys.*, 74: 79 – 86. doi:10.1016/j.astropartphys.2015.10.004. (Cited on page 91)
- Lapp, J. (2013). *Bestimmung und Verbesserung der LOPES-Winkelauflösung*. Bachelor thesis, Karlsruher Institut für Technologie. (Cited on pages 79 and 92)
- Lawrence, M. A., Reid, R. J. O. and Watson, A. A. (1991). *The cosmic ray energy spectrum above  $4 \times 10^{17}$  eV as measured by the Haverah Park array*. *J. Phys. G*, 17 (5): 733. URL 10.1088/0954-3899/17/5/019. (Cited on page 9)
- Link, K. et al. (2011). *Improved Radio Data Analysis with LOPES*. Proceedings of the 32nd ICRC 2011, 3: 92. doi:10.7529/ICRC2011/V03/0404. (Cited on page 37)
- Link, K. et al. (2013). *Comparison of LOPES data and CoREAS simulations using a full detector simulation (ICRC2013)*. Proceedings of the 33rd ICRC 2013, id 0844. arXiv: 1308.2523. (Cited on page 37)

- Link, K. et al. (2016). *Revised absolute amplitude calibration of the LOPES experiment*. Proceedings of the 34th ICRC 2015, PoS, 311. arXiv:1508.03471. (Cited on pages 63 and 79)
- Ludwig, M. and Huege, T. (2011). *REAS3: Monte Carlo simulations of radio emission from cosmic ray air showers using an "end-point" formalism*. *Astropart. Phys.*, 34 (6): 438 – 446. doi:10.1016/j.astropartphys.2010.10.012. (Cited on pages 31 and 37)
- Luis, P. Facal San et al. (2013). *Status of the program for microwave detection of cosmic rays at the Pierre Auger observatory*. Proceedings of the UHECR 2012, EPJ Web of Conf., 53: 08009. doi:10.1051/epjconf/20135308009. (Cited on page 16)
- Martineau-Huynh, O. et al. (2012). *First results of the TIANSHAN radio experiment for neutrino detection*. Proceedings of the 4th ARENA 2010, Nucl. Instrum. Meth. A, 662: S29 – S31. doi:10.1016/j.nima.2010.11.143. (Cited on page 16)
- Matthews, J. (2005). *A heitler model of extensive air showers*. *Astropart. Phys.*, 22 (5–6): 387 – 397. doi:10.1016/j.astropartphys.2004.09.003. (Cited on page 8)
- McMullin, J. P. et al. (2007). *CASA Architecture and Applications*. 376: 127. URL <http://adsabs.harvard.edu/abs/2007ASPC..376..127M>. (Cited on page 68)
- Nehls, S. (2008). *Calibrated Measurements of the Radio Emission of Cosmic Ray Air Showers*. FZKA Report 7440, Forschungszentrum Karlsruhe. URL <https://publikationen.bibliothek.kit.edu/200073266>. (Cited on pages 21 and 31)
- Nehls, S. et al. (2008). *Amplitude calibration of a digital radio antenna array for measuring cosmic ray air showers*. *Nucl. Instrum. Meth. A*, 589: 350–361. doi:10.1016/j.nima.2008.02.092. (Cited on pages 43, 64 and 67)
- Nelles, A. et al. (2015a). *A parameterization for the radio emission of air showers as predicted by CoREAS simulations and applied to LOFAR measurements*. *Astropart. Phys.*, 60: 13 – 24. doi:10.1016/j.astropartphys.2014.05.001. (Cited on page 12)
- Nelles, A. et al. (2015b). *Calibrating the absolute amplitude scale for air showers measured at LOFAR*. *JINST*, 10 (11): P11005. doi:10.1088/1748-0221/10/11/P11005. (Cited on pages 63, 71 and 76)
- Nichol, R. et al. (2011). *Radio detection of high-energy particles with the ANITA experiment*. *Nucl. Instrum. Meth. A*, 626–627: S30 – S35. doi:10.1016/j.nima.2010.06.268. (Cited on page 16)
- Nigl, A. et al. (2008a). *Direction identification in radio images of cosmic-ray air showers detected with LOPES and KASCADE*. *Astron. Astrophys.*, 487: 781–788. doi:10.1051/0004-6361:20079218. (Cited on page 19)
- Nigl, A. et al. (2008b). *Frequency spectra of cosmic ray air shower radio emission measured with LOPES*. *Astron. Astrophys.*, 488: 807–817. doi:10.1051/0004-6361:20079219. (Cited on page 19)
- Ostapchenko, S. (2006). *QGSJET-II: Results for extensive air showers*. *Nucl. Phys. Proc. Suppl.*, 151: 147–150. doi:10.1016/j.nuclphysbps.2005.07.027. (Cited on page 34)

- Petrovic, J. et al. (2007). *Radio emission of highly inclined cosmic ray air showers measured with LOPES*. *Astron. Astrophys.*, 462: 389–395. doi:10.1051/0004-6361:20065732. (Cited on page 19)
- Prosin, V. V. et al. (2014). *Tunka-133: Results of 3 year operation*. *Nucl. Instrum. Meth. A*, 756: 94–101. doi:10.1016/j.nima.2013.09.018. (Cited on pages 10 and 104)
- Ravel, O. et al. (2012). *The CODALEMA experiment*. Proceedings of the 4th ARENA 2010, *Nucl. Instrum. Meth. A*, 662: S89 – S94. doi:10.1016/j.nima.2010.12.057. (Cited on page 15)
- Saftoiu, A. et al. (2012). *Investigations of the radio signal of inclined showers with LOPES*. Proceedings of the 4th ARENA 2010, *Nucl. Instrum. Meth. A*, 662: S85 – S88. doi: 10.1016/j.nima.2010.11.141. (Cited on page 64)
- Schiebel, D. R. (1996). *Programming in Glish*. 101: 315. (Cited on page 68)
- Scholten, O., Werner, K. and Rusydi, F. (2008). *A macroscopic description of coherent geomagnetic radiation from cosmic-ray air showers*. *Astropart. Phys.*, 29: 94–103. astro-ph/0709.2872. (Cited on pages 13 and 14)
- Schoorlemmer, H. (2013). *Tuning in on cosmic rays*. Ph.D. thesis, Radboud University Nijmegen. URL [http://www.nikhef.nl/pub/services/biblio/theses\\_pdf/thesis\\_H\\_Schoorlemmer.pdf](http://www.nikhef.nl/pub/services/biblio/theses_pdf/thesis_H_Schoorlemmer.pdf). (Cited on page 12)
- Schröder, F., Link, K. et al. (2016). *New results of the digital radio interferometer LOPES*. Proceedings of the 34th ICRC 2015, PoS, 317. (Cited on pages 37, 63 and 79)
- Schröder, F. G. (2011). *Instruments and Methods for the Radio Detection of High Energy Cosmic Rays*. Ph.D. thesis. URL <https://publikationen.bibliothek.kit.edu/1000022313>. (Cited on pages 47 and 80)
- Schröder, F. G. et al. (2010). *New method for the time calibration of an interferometric radio antenna array*. *Nucl. Instrum. Meth. A*, 615 (3): 277 – 284. doi:10.1016/j.nima.2010.01.072. (Cited on page 24)
- Schröder, F. G. et al. (2012). *On noise treatment in radio measurements of cosmic ray air showers*. Proceedings of the 4th ARENA 2010, *Nucl. Instrum. Meth. A*, 662: S238 – S241. doi:10.1016/j.nima.2010.11.009. (Cited on pages 25, 38, 46 and 80)
- Schröder, F. G. et al. (2013). *Cosmic ray measurements with LOPES: Status and recent results*. Proceedings of the 5th ARENA 2012, AIP Conference Proceedings, 1535 (1): 78–83. doi:10.1063/1.4807525. (Cited on pages 94, 95 and 96)
- Schröder, F. G. et al. (2013a). *Radio detection of air showers with the Auger Engineering Radio Array*. Proceedings of the 33rd ICRC 2013, id 0899. URL <http://www.cbpf.br/~icrc2013/papers/icrc2013-0899.pdf>. (Cited on page 15)
- Schröder, F. G. et al. (2013b). *Radio Measurements of Air Showers with LOPES*. Proceedings of the 23rd ECRS 2012, JPCS, 409 (1): 012075. URL <http://stacks.iop.org/1742-6596/409/i=1/a=012075>. (Cited on page 100)

- Schröder, F. G. et al. (2015). *LOPES — Recent Results and Open Questions on the Radio Detection of Air Showers*. Proceedings of the 24th ECRS 2014, JPCS, 632 (1): 012102. doi:10.1088/1742-6596/632/1/012102. (Cited on page 22)
- Sciutto, S. J. (1999). *AIRES: A system for air shower simulations (Version 2.2.0)*. arXiv:astro-ph/9911331. (Cited on page 8)
- Thoudam, S. et al. (2014). *LORA: A scintillator array for LOFAR to measure extensive air showers*. Nucl. Instrum. Meth. A, 767 (0): 339 – 346. doi:10.1016/j.nima.2014.08.021. (Cited on page 15)
- Unger, M. (2008). *Cosmic Rays above the Knee*. Proceedings of the 21st ECRS 2008. arXiv:0812.2763. (Cited on page 6)
- van Haarlem, M. P. et al. (2013). *LOFAR: The LOw-Frequency ARray*. Astron. Astrophys., 556: A2. doi:10.1051/0004-6361/201220873. (Cited on page 15)
- Verzi, V. (2016). *Cosmic rays: air showers from low to high energies*. Proceedings of 34th ICRC 2015, PoS, 015. URL [http://pos.sissa.it/archive/conferences/236/015/ICRC2015\\_015.pdf](http://pos.sissa.it/archive/conferences/236/015/ICRC2015_015.pdf). (Cited on page 6)
- de Vries, K. D., van den Berg, A. M., Scholten, O. and Werner, K. (2010). *The lateral distribution function of coherent radio emission from extensive air showers: Determining the chemical composition of cosmic rays*. Astropart. Phys., 34 (5): 267 – 273. doi: 10.1016/j.astropartphys.2010.08.003. (Cited on page 12)
- de Vries, K. D., van den Berg, A. M., Scholten, O. and Werner, K. (2011). *Coherent Cherenkov Radiation from Cosmic-Ray-Induced Air Showers*. Phys. Rev. Lett., 107: 061101. doi:10.1103/PhysRevLett.107.061101. (Cited on page 14)
- de Vries, K. D., Scholten, O. and Werner, K. (2012). *Macroscopic Geo-Magnetic Radiation Model: Polarization effects and finite volume calculations*. Proceedings of the 4th ARENA 2010, Nucl. Instrum. Meth. A, 662: S175–S178. doi:10.1016/j.nima.2010.10.127. (Cited on page 12)
- Šmída, R. et al. (2014). *First Experimental Characterization of Microwave Emission from Cosmic Ray Air Showers*. Phys. Rev. Lett., 113 (22): 5. doi:10.1103/PhysRevLett.113.221101. (Cited on page 16)
- Zatsepin, G. and Kuzmin, V. (1966). Zh. Eksp. Teor. Fiz., 4: 114–117. (Cited on page 6)



## Danksagung

Hiermit möchte ich mich bei allen bedanken, die mich in den letzten Jahren unterstützt und zum Gelingen dieser Arbeit beigetragen haben.

Besonders möchte ich mich bei Herrn Prof. Dr. Dr. h.c. Blümer für die Übernahme des Referats und Herrn Prof. Dr. Quast für die Übernahme des Korreferats bedanken.

Außerdem danke ich Herrn Dr. Tim Huege für seine gute Betreuung und dafür, dass er mich während der ganzen Zeit unterstützt hat und mir Mut gemacht hat die Arbeit, trotz der Pausen, zu beenden.

Bedanken möchte ich mich auch bei Herrn Dr. Andreas Haungs der mir nicht nur fachlich weiter geholfen hat sondern auch immer wieder für gute Laune gesorgt hat.

Ganz besonderer Dank geht an meine aktuellen und ehemaligen Kollegen, ohne die die Zeit am Institut nie so schön gewesen wäre. Danke für die Zeit in Büro 135 geht an Anne, Aswathi, Agnieszka, Daniel, Andreas, Michael, Johannes, Colin, Jan und alle anderen. Von meinen ehemaligen Kollegen möchte ich ganz besonders Julia danken, die mich nicht nur während der Arbeit und auf Dienstreisen begleitet hat sondern auch eine gute Freundin geworden ist. Außerdem danke an Olga, Ewa, Marianne, Nunzia, Martin, Felix, Ben, Roman, Donghwa, Sven und Heike, die mir immer wieder geholfen haben und mit denen ich jede Menge Spaß hatte.

Bedanken möchte ich mich auch bei der LOPES und KASCADE-Grande Kollaboration. Insbesondere bei Frank, der mir bei allen Fragen rund um LOPES immer geduldig weiter geholfen hat.

Danke auch an Sabine für ihre Hilfe in allen organisatorischen Dingen.

Ganz herzlich möchte ich mich auch bei meinen Freunden und bei meiner Familie bedanken. Danke an meine Eltern die mich immer auf unterschiedlichste Weise unterstützt haben. Marlene und Josefine möchte ich dafür danken, dass sie mich immer wieder auf wunderbare Weise von der Arbeit abgelenkt haben. Und ein ganz großes Danke geht an Sebastian, ohne dessen Unterstützung und Rückhalt ich diese Arbeit nicht hätte abschließen können.